Simultaneous Far-infrared and X-ray Monitoring of Young Stellar Objects in the Coronet Cluster

author:
Miriam Gómez-Elegido

supervised by:
Associate Professor Jan Forbrich, Principal Supervisor
Professor Philip Lucas, Second Supervisor

Centre for Astrophysics Research
School of Physics, Engineering & Computer Science
University of Hertfordshire

Submitted to the University of Hertfordshire in partial fulfilment of the requirements of the degree of MSc by Research.

September 2021

Abstract

Context: Multi-wavelength time domain analysis of Young Stellar Objects (YSOs) is a relatively new method within star formation research which may lead to better constraints on fundamental star formation processes. Such young objects are known to be strong X-ray emitters whereas in the far-infrared we are mainly probing the protoplanetary disk of these YSOs. Protostars are known to be variable in the X-ray, likely due to magnetic coronal activity. Far-infrared variability is still little understood and has only been detected once, but the possibility of finding variability in both wavelengths will allow us to compare processes that may be happening in the corona (X-ray) and the disk (far-infrared).

Aims: Here we present the first simultaneous XMM-Newton and Herschel short-timescale variability analysis of the YSOs in the Coronet Cluster. Located in the Corona Australis Molecular Cloud complex, this is a young (<2 Myr), nearby (149.4 ± 0.4 pc) star-forming region populated with several Class 0 and I protostars as well as a number of T Tauri stars. We analyze the X-ray and far-infrared variability separately so we can then look for first signs of potential correlated variability in this unique experiment.

Methods: We use archival images taken by the Herschel Space Observatory at 100 μm and 160 μm and the XMM-Newton Space Telescope in March 2012 over five epochs with 1, 2, 4, and 8 days between epochs, allowing us to probe for variability on many intermediate timescales.

Results: In the far-infrared, eleven objects are detected in the 100 μm band and eight in the 160 μm band, and seven of these are detected simultaneously in the X-ray band. All seven protostars display some level of X-ray variability and three exhibit far-infrared variability. The most variable far-infrared source is the T Tauri star S CrA and the most variable X-ray source is the Class 0 protostar IRS 7e, which had a flare in the final epoch of up to 36 times the flux of previous epochs. The Class I protostar IRS 1 seemed to exhibit correlated variability with a far-infrared peak in the first epoch and an X-ray peak in the second epoch.

Conclusions: We find a first case of possibly correlated and time-delayed variability, where the far-infrared peak follows the X-ray peak. This suggests that magnetic coronal activity could indeed be affecting the protoplanetary disk on timescales of days. A future detailed comparison with models will lead to unique empirical constraints, taking into account both this apparently correlated case and the remaining variability.

Contents

List of Figures

List of Tables

Chapter 1

Introduction

1.1 Project overview

In this project we present an analysis of young stellar objects (YSOs) in the Coronet Cluster by comparing simultaneous multi-wavelength observations taken in the far-infrared by the Herschel Space Observatory[1] and in the X-ray by the XMM-Newton Space Telescope[2]. The Coronet Cluster is a nearby (149.4 ± 0.4 pc; Galli et al., 2020), young (< 2 Myr; Sicilia-Aguilar et al., 2011), star-forming region with a large population of well known protostars. These two datasets are quite complementary since both can overcome foreground extinction, YSOs are generally strong X-ray emitters, and in the far-infrared we are mainly probing the protoplanetary disk of these YSOs. Protostars are known to be variable in the X-ray, likely due to magnetic coronal activity. Far-infrared variability of YSOs (in physical terms, likely due to a temperature change in the disk) is still little understood and has only been detected once (Billot et al., 2012), but the possibility of finding variability in both wavelengths will allow us to compare processes that may be happening in the corona (X-ray) and the disk (far-infrared). Multi-wavelength monitoring in the past revealed no obvious correlation between near-infrared and X-ray variability (Forbrich et al., 2007), but our study is the first to compare far-infrared observations with X-ray. Our observations were taken by both cameras on five days with 1, 2, 4, and 8 days between epochs, allowing us to probe for variability on many intermediate timescales. In general, what we are looking for would be an X-ray flare and then a far-infrared response

---

[1]Herschel is an ESA space observatory with science instruments provided by European-led Principal Investigator consortia and with important participation from NASA.

[2]Based on observations obtained with XMM-Newton, an ESA science mission with instruments and contributions directly funded by ESA Member States and NASA.

which could indicate a heating event on the disk.

In Chapter 1 we introduce our motivation and briefly give an overview of young star formation and evolution as well as discuss previous studies of the Coronet Cluster both in far-infrared and X-ray. In Chapter 2, we present the far-infrared photometry of the sources discussed in the introduction. Then we look for variability in the far-infrared as this has only been seen once. If observed, this would have interesting implications as disks have dynamical timescales much larger than those we are probing (discussed in Section 1.2.4) and thus we explore what could cause this short timescale variability. It also allows us to compare with any X-ray variability to find correlations. Next, in Chapter 3, we present the X-ray photometry and then look at the light curves to check for variability. In Chapter 4 we compare the light curves of the far-infrared and X-ray sources. We look for correlated variability. In Section 1.2.2 we discuss X-rays flares and disk heating and possible explanations for them. We then present our discussion in Chapter 5, summarize our conclusions in Chapter 6, and finish up with future work in Chapter 7.

1.2   Protostellar evolution and disk formation

1.2.1   Stages of stellar evolution

Stars form in dusty molecular clouds when dense cores gravitationally collapse. Disks are formed around young stars as a result of angular momentum conservation. These are called protoplanetary disks. Stars then accrete most of their mass from the surrounding disc. Shu et al. (1987) is a good early review of low mass star formation and Swift & Welch (2008) is a newer review and case study.

Low mass ($< 2 \; \mathrm{M_\odot}$) YSOs are classified by measuring the slope of their infrared SED from 2 μm to 10–25μm (Lada, 1987). This tells us if the protostar is emitting more at longer wavelengths (cooler temperature indicates an earlier evolutionary stage) or shorter wavelengths (hotter temperature indicates a later evolutionary stage). Lada (1987) used the infrared spectral index:

$$\alpha = \frac{dlog(\lambda S_\lambda)}{dlog\lambda} \tag{1.1}$$

and defined S_λ as the flux density at wavelength λ. An SED with slope $\alpha < 0.3$ is a Class I protostar, Class II objects have a decreasing infrared SED with slope -1.5 $< \alpha <$ -0.3 and Class III objects have a decreasing infrared SED with slope $\alpha <$ -1.5.

Class 0 objects were added later to represent protostars that are too deeply embedded to detect in the near-infrared. They are defined as sources that have a ratio of submillimeter luminosity to bolometric luminosity greater than 0.5%, where the submillimeter luminosity is calculated for $\lambda \geq 350$ μm (Andre et al., 1993, 2000).

Class 0 objects represent the early stage of stellar evolution where the molecular cloud core has just begun to gravitationally collapse. Their envelopes are more massive than the central object (Andre et al., 1993), where material is rapidly accreting, and a disk is beginning to develop. The envelope masses were calculated by Andre et al. (1993) using dust mass opacity and temperature which they derived from submillimeter observations of Class 0 objects. Due to how embedded they are, they can only be observed by the submillimeter to millimeter emission of their cold envelopes but they have more recently been detected in the X-ray (Grosso et al., 2020), which suggests X-ray ionization could have an influence on protostars in these very early stages (we discuss this further in Section 1.2.2). This phase lasts for 10^4 years (Andre et al., 1993) where the starting point for this age (and all ages given in this section) is when the molecular cloud core begins to collapse.

Class I objects have a rising infrared continuum ($\alpha > 0.3$) and are thought to have an infalling envelope surrounding the protostar. Their luminosity is primarily due to accretion, although their accretion rate is lower than it was in the Class 0 stage. From this stage forward, X-ray emission from protostars is well established (e.g. Getman & Feigelson, 2021; Getman et al., 2008), though extinction can still play a role and sometimes lead to a nondetection. This phase lasts for 10^5 years (Kaas et al., 2004).

As the envelope dissipates, the accretion rate then decreases and the protostar enters the Class II phase. Class II objects are classified by their decreasing infrared SEDs with -1.5 $< \alpha <$ -0.3. These objects are also called "classical T Tauri stars" (CTTS). At this stage, since their outer envelopes are mostly dissipated, they are optically visible, and they are close to their final mass, but disk accretion continues.

When the dust in the disk begins to coalesce into large grains, and the gas dissipates, the star begins its Class III phase. Class III objects have decreasing IR SEDs with $\alpha <$ -1.5 (Andre & Montmerle, 1994) and have little or no detectable infrared excess, and thus have likely dissipated the majority of their disks. These objects are also called "weak-line T Tauri stars" (WTTS) because they have weak Hα emission when compared to CTTS which have strong Hα lines. Hα emission is a good tracer for ionized hydrogen, thus sources that have dissipated most of the gas in their disks will have weaker Hα lines.

1.2.2 Disk ionization and heating

In the early stages of star formation, we know the collapse of protostellar clouds should result in the formation of disks and protostars. This stage is then followed by envelope and disk accretion (Class 0/I and Class II) during which angular momentum is transferred to disk particles (gas and dust) permitting the accretion onto the central protostar and some smaller fraction possibly forming planets. This evolution is thus controlled by the rate of angular momentum transport within the disk. The mechanism for the angular momentum transport is not yet fully clear but the most likely mechanism is magnetic turbulence, or magnetorotational instability (Güdel, 2015).

Protoplanetary disks are immersed in X-ray radiation that originates from the magnetized stellar corona of the central YSO and sometimes from collimated jets, although X-rays do not typically reach the full volume of these disks. According to the standard model (e.g. Fletcher et al., 2011), the primary source of X-ray emission is magnetic field reconnection events in the corona and magnetosphere of the YSO. High up in the corona, this sudden rearrangement of the magnetic field configuration leads to a release of accumulated magnetic energy. These energetic particles flow downwards and upwards and the electrons moving downwards intersect the chromosphere and heat the plasma, and the hot plasma emits X-rays. When these X-rays are emitted by the hot corona they irradiate the protoplanetary disk and begin to ionize it. Although they are not a part of our study so we will not go into detail, we must mention that cosmic rays are another primary mechanism of disk ionization along with X-rays. They ionize the disk together and if a minimum ionization level is reached, the gas in the disk couples with the magnetic fields and is able to maintain the magnetic turbulence needed for effective angular momentum transport (Blaes & Balbus, 1994); this drives accretion.

According to Güdel (2015), in the process of ionizing the gas in the disk, X-rays also heat up the material in the disk. They list the mechanisms of heating, which include chemical reactions, collisional de-excitation, and dissociation after collisional excitation. For this project, further details of these mechanisms are outside the scope as we are just interested in if there is a correlation between the X-ray flare and heating event. Our future work section details some next steps using our results which would then consider the mechanism of heating.

Güdel (2015) calculate that X-rays are important heating agents out to 35-40 AU and disk ionization by stellar X-rays can even be seen out to 190 AU in Monte-Carlo
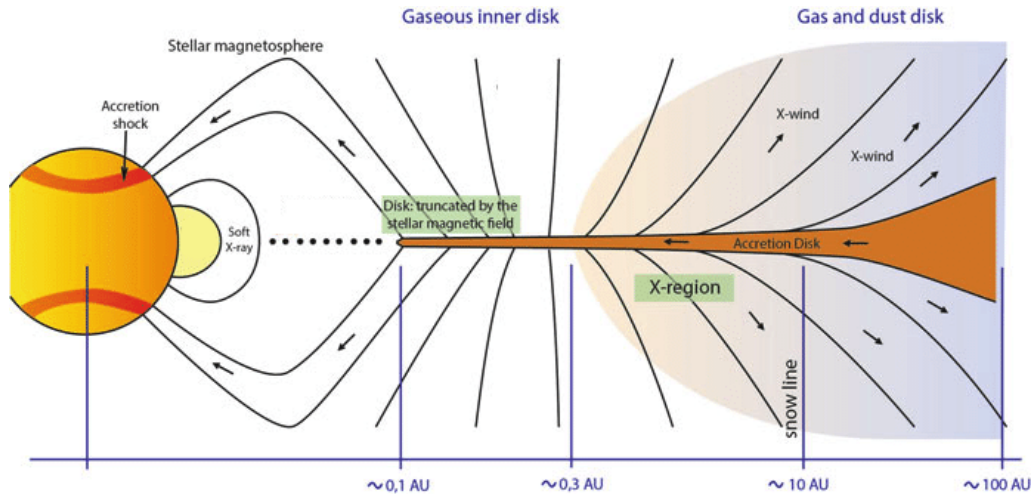
Figure 1.1: Figure adapted from Martínez-Jiménez et al. (2017) of magnetic fields around a protostar and protoplanetary disk (not to scale). We see the arrows where the material accretes from the disk onto the central source. The stellar magnetosphere is where the X-ray reconnection events happen and are then radiated out onto the disk, ionizing it. The snow line is labeled, which is the beginning of the region where the temperature is below the condensation temperature of water. The X-region is where X-winds might propagate outwards, X-winds being high-speed bipolar-collimated jets that are powered by magnetic activities. The snow line and X-region are outside the scope of this project and thus will not be discussed further.

simulations done by Ercolano et al. (2008). This process causes photoevaporation of the gas from the uppermost disk layers. Therefore the lifetime of the disk is certainly affected by, and possibly controlled by, these high energy processes taking place on the central star. And since planets are formed in the disk as well, these processes and their timescales could have implications for planet formation (Güdel, 2015). If we are able to see variable X-ray emission (likely due to high levels of coronal magnetic activity) followed by variable/increased far-infrared flux, this could be a heating response in the disk due to the X-ray emission radiating to the outer disk, being re-processed, thus heating the disk, and being re-emitted in the far-infrared. That could give insight as to whether protostellar magnetic fields are causing enough ionization and heating to affect the outer disk. However, in this work we will not be doing a detailed radiative transfer analysis.

1.2.3 Multi-wavelength analysis of variability

Star formation research is fundamentally a multi-wavelength field. X-rays and far-infrared emission are both particularly good at penetrating thick molecular clouds, allowing us to observe deeply embedded young protostars. And since young stars usually show high levels

of X-ray emission, X-ray studies are good at separating YSOs from other sources in the field of view. Observations primarily probe material with a temperature that peaks at the observing wavelength. The observing wavelengths of our Herschel images are 100μm and 160μm which, using Wein's displacement law to convert peak wavelength to temperature, correspond to $\sim$29K and $\sim$18K respectively. This is the temperature of the material in the outer disk, about 10^2 AU from the central protostar (Lesniak & Desch, 2011). Thus the combination of far-infrared and X-ray observations is perfect for attempting to see a heating response in the outer disk (far-infrared) after an ionization event (X-ray).

Most processes happening on the disk have timescales orders of magnitude longer than the short timescales (see Section 1.2.4) that we are looking at for variability, so we know that if we see variability, it is more likely due to a heating response than processes in the disk itself. However this is still unclear as accretion is a possible explanation since accretion happens in bursts (see Fig 1.12 in Hartmann, 2008) thus the emission that is released when the material hits the surface of the star can be variable, though we would typically expect this to happen on longer timescales than days, which is what we are observing. Accretion is given as a possible reason for far-IR variability by Billot et al., 2012 (which we discuss further in 1.4.2) and Flaherty et al., 2014 (which we discuss in 1.2.3), but the latter only consider it because they did not find a correlation with the X-ray variability. Accretion is also considered unlikely by Flaherty et al., 2011 and Flaherty et al., 2012 (as we discuss in 1.2.4).

If we see X-ray variability at the same time as far-infrared variability, this could be a stellar flare; if there is a correlation with a time delay, which we expect since it takes photons time to reach these outer parts of the disk (this being the light travel time, or $\sim$0.5-3 days to reach the far-IR emitting material at 10^2 AU from the protostar), that could be a heating response in the disk. We expect to see X-ray variability because we know there are many X-ray flares in YSOs, and they have been observed from the Coronet Cluster as discussed in Section 1.4.2.

Simultaneous measurements

Comparing simultaneous observations of infrared and X-ray emission can give us insight into whether X-ray flares can affect the circumstellar disks. As discussed below, previous studies have been done comparing simultaneous X-ray and mid-infrared (emission from the mid-disk or $\sim$1-5 AU from the central object), but none comparing far-infrared. Here

we discuss what the most relevant previous studies have found.

Flaherty et al. (2014) did a recent study looking at simultaneous observations of pre-main-sequence stars in the IC 348 cluster with Chandra (X-ray) and Spitzer (mid-infrared, 3–5 μ m). Their images were taken in 2011 over the course of a month with 2-3 days between epochs. This allowed them to look at week to month long infrared correlations between X-ray flares and mid-infrared responses. They found 39 sources with detections in X-ray and mid-IR, as well as enough infrared excess to indicate the sources have a disk. Of these, 28 stars were variable in both bands. But when they looked for correlations between the X-ray and mid-IR light curves of these variable stars, they found none. Thus Flaherty et al. (2014) ruled out X-ray ionization as the cause of the mid-IR variability and gave the most likely reasons, as discussed by the references they give, to be accretion bursts, variable obscuring of the central star, or changes to the structure of the inner disk (Cody et al., 2014; Stauffer et al., 2014; Wolk et al., 2013).

Another multi-wavelength simultaneous study was done by Flaccomio et al. (2018) comparing Chandra X-ray, CoRoT optical, and Spitzer infrared observations taken simultaneously in 2008 and 2011 of the NGC 2264 star forming region. They detected 78 X-ray flares with an optical or mid-infrared counterpart. They found the optical emission to correlate with the X-ray emission. They also found that mid-infrared flares coming from stars with disks had a much higher amount of mid-infrared emission than those without disks. They discussed that the most likely reason was that the mid-infrared excess was a response on the inner disk to the optical and X-ray flares and that most of the mid-infrared flux is "reprocessed emission" or emission from the optical/X-ray flares that is absorbed by the circumstellar material and then re-emitted in the mid-infrared. The results and conclusions of these studies are very interesting and directly help motivate our study. Flaherty et al. (2014) concluded that in their dataset there was no correlation between mid-IR and X-ray variability, thus they found no evidence that X-ray ionization is a cause of mid-infrared variability. However the Flaccomio et al. (2018) study asserts that it is possible the mid-infrared flares they observed were the result of a heating response in the inner disk due to the heating from the X-ray and optical flares. In our study we are instead comparing the X-ray flares to the far-infrared emission, which, while still tracing the circumstellar disk as does the mid-IR in these previous studies, far-IR flux is primarily emission from farther out in the disk, orbiting at hundreds of AU from the central star (as previously discussed). So since correlations between X-ray and mid-IR flux from the

inner disk have been observed, but not consistently, we are looking to see if we observe a similar correlation between X-ray and far-infrared variability.

1.2.4 Timescales

The timescales of disk formation/dissipation are on the order of Myr and dynamical processes of protoplanetary disks are on the timescales of years. The primary dynamical process is disk rotation, which at the radii we are probing in far-infrared is about 10^3-10^5 years.

Variability of disks on short timescales has been studied and found that accretion is likely not the driving force. Flaherty et al. (2011) found variations of mid-infrared excess on the timescales of weeks when studying the transition disk LRLL 31. They say the variability is likely due to a companion further out than 0.4 AU or the dynamic interface between the disk and the stellar magnetic field, and not accretion. Flaherty et al. (2012) went on to study six more disks with strong mid-infrared variability on timescales of weeks (though not days) and found the most likely cause to be vertical perturbation of the inner disk. They also agree it is unlikely that the variability comes from the accretion or from the stellar flux as variability from the stellar flux is on different timescales. They do also, like the previous study, consider companion stars at certain radii to be another possible explanation.

Konstantin Getman has published many papers on X-ray flares from young stars and their timescales. Getman et al. (2008) examined 216 of the brightest flares from 161 pre-main sequence (PMS) stars observed during the Chandra Orion Ultradeep Project (COUP). They found the timescale for the rise of the flare to range from 1 hour to 1 day (3-100 ks) and the timescale for the flare decay to be a few hours to 1.5 days (10-150 ks). Getman et al. (2021) looked at >1000 X-ray super-flares from PMS stars and found a rise timescale ranging from about 6 minutes to 4 days (0.4-400 ks) with the median being about 1.5 hours ($\sim$5 ks). Decay timescales ranged from 1 hour to 1 day (2.6-111 ks) with a median of about 4 hours ($\sim$14 ks).

If we see a heating response in the far-infrared, we expect there to be a time lag between this and the X-ray flare, since the photons take time to travel to the disk. The typical timescale for photons to reach the part of the disk that emits in the far-infrared traveling roughly at the speed of light is a few days (Billot et al., 2012). If we do not see a time lag, this could indicate we are not seeing a heating response but emission from the

star itself, since its SED will have some emission at longer wavelengths as mentioned in Sections 1.2.3 and 1.3.

1.3 Telescopes

In this study, we used archival images taken by the Herschel Space Observatory and the XMM-Newton Space Telescope, both operated by the European Space Agency (ESA). In this section we briefly describe these telescopes, as well as the detectors on them that took our observations.

1.3.1 Herschel Space Observatory

All details in this section were found on the ESA website[3] or the Herschel Observer's Manual (ESA, 2014). The Herschel Space Observatory, operated by the ESA from 2009 to 2013, was the largest infrared telescope ever launched and the first that was sensitive to wavelengths from far-infrared to submillimeter (55-672 μm). In its lifetime, it executed over 35,000 scientific observations and collected more than 25,000 hours worth of scientific data (ESA, 2013). It was approximately 7.5 meters long with a diameter of 4 meters. The primary mirror of the telescope had a diameter of 3.5 meters which is the largest ever designed for a space telescope.

It was equipped with three instruments: Heterodyne Instrument for the Far Infrared (HIFI), a high resolution spectrometer; Photodetector Array Camera and Spectrometer (PACS), an imaging photometer and low/medium resolution grating spectrometer for wavelengths in the range of 55-210 μm; and Spectral and Photometric Imaging REceiver (SPIRE), an imaging photometer and medium resolution Fourier Transform Spectrometer (FTS) for wavelengths in the range of 194-672 μm. We use observations taken by PACS because it covers the wavelengths we are interested in, thus we limit our discussion of Herschel to PACS and overview it in the next section.

As previously mentioned, Herschel observations are primarily probing material with a temperature peaking in the observing wavelength, which for our data is 160μm and 100 μm, thus about 18-29K. This corresponds to material further out in the disk where it is colder, about 10^2 AU from the central object (with the typical outer radii of protostellar disks being about 100-400 AU in the Coronet Cluster as per Sicilia-Aguilar et al., 2013), in

---

[3]https://www.cosmos.esa.int/web/herschel/home
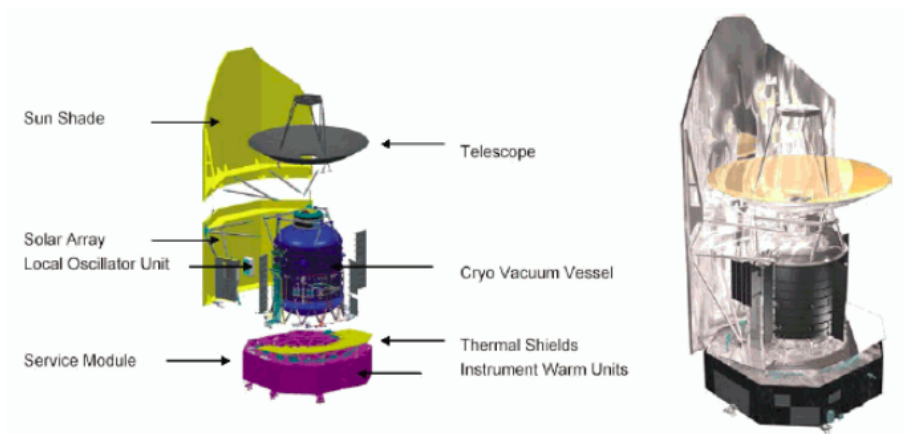
Figure 1.2: Herschel Space Observatory (image from ESA website).

contrast to near-infrared studies which probe the inner disk at < 0.05-0.1 AU (temperature structure of the disk from Lesniak & Desch, 2011). However it is important to note that due to the shape of the SED, hot material can also emit at longer wavelengths at the tail of the SED (in this case, that would be the star itself). This means that if the star's emission varies, the far-infrared will also vary to a small degree. This effect is less noticeable the further away the peak wavelength is from the observing wavelength, so for Herschel, the emission from the outer disk should dominate what we observe.
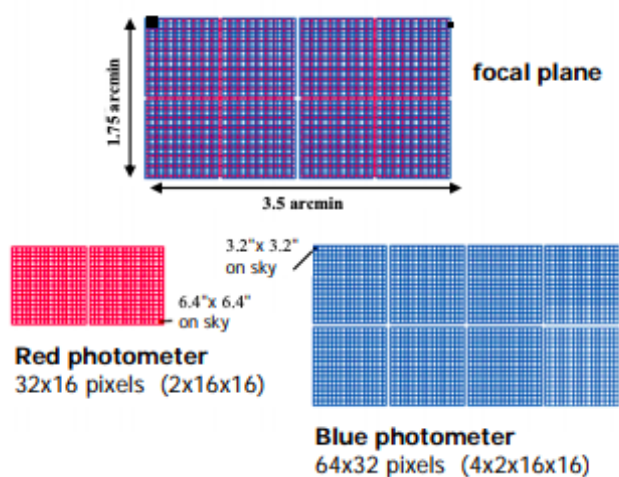
Figure 1.3: From the PACS Factsheet[4]

---

[4]http://herschel.esac.esa.int/Docs/Flyers/PACS_flyer_21May2010.pdf.

The Photodetector Array Camera and Spectrometer (PACS) Photometer

The PACS photometer is a far-infrared instrument aboard the Herschel Space Observatory that consists of a threeband imaging photometer and an integral field spectrometer, allowing it to operate either as a spectrometer or photometer. It operated from 24 May 2009 to 30 April 2013.

The camera contains two bolometer detector arrays: the first with 64×32 pixels called the "blue" array, and the second with 32×16 pixels called the "red" array. The "blue" array has a pixel size of 3.2" x 3.2" and the "red" array has a pixel size of 6.4" x 6.4" (this can be seen in Figure 1.3). These provided an instantaneous field-of-view of 3.5×1.75 arcmin^2 as seen in Figure 1.3. The "blue" array was coupled with a blue (70 μm) and green (100 μm) filter and the "red" array was coupled with a red (160 μm) filter. This allowed for all observations to be taken simultaneously in two bands: either the blue and red or green and red channels. The angular resolutions (PSF) of each of the three bands are as follows: 5.6" (70 μm), 6.8" (100 μm) and 11.3" (160 μm). For more details see the PACS instrument paper (Poglitsch et al., 2010) and the final version of the PACS Handbook[5].

1.3.2   XMM-Newton

All details in this section were found in the XMM-Newton Users Handbook v.2.19.

X-ray telescopes work differently to conventional mirror telescopes designed for normal incidence because when X-rays strike a mirror surface at a perpendicular angle, they are either transmitted or absorbed, not reflected. Thus X-ray telescopes have to have mirrors with a very low angle of reflection, called grazing incidence mirrors. The mirrors are made of ceramic or metal foil and then covered in a thin coat of reflective material, typically gold or iridium (the XMM-Newton telescope is made of aluminum covered in a layer of gold and nickel as seen in Figure 1.4). The incident X-rays are then reflected onto CCDs (charge-coupled devices) which record the time the photon arrives, location where it hits the camera, and the energy of the photon.

The "X-ray Multi-Mirror" (where XMM gets its name) mission was proposed in 1982 because before the late 1970s only four galaxies had been observed to emit X-rays. It's overall configuration was developed by 1987 and built on ESA's previous X-ray space observatory Exosat, which ran from 1983 to 1986, making 1780 X-ray observations and

---

[5]www.cosmos.esa.int/documents/12133/996891/PACS+Explanatory+Supplement/

proving that an eccentric orbit was very helpful in allowing for long and uninterrupted observations. XMM-Newton was launched in December 1999 and is still operating today.

The XMM-Newton Spacecraft is the largest scientific satellite ever launched by the European Space Agency at a weight of 4 tonnes and a length of 10 meters. It has a 48 hour elliptical orbit that takes it from 7 to 114 thousand km from Earth which means that for every orbit, it spends 40 hours outside of Earth's obscuring radiation belts (where Earth's magnetic fields trap particles thus they do not reach the telescopes). And its orbit means Earth's atmosphere does not block out celestial X-rays.
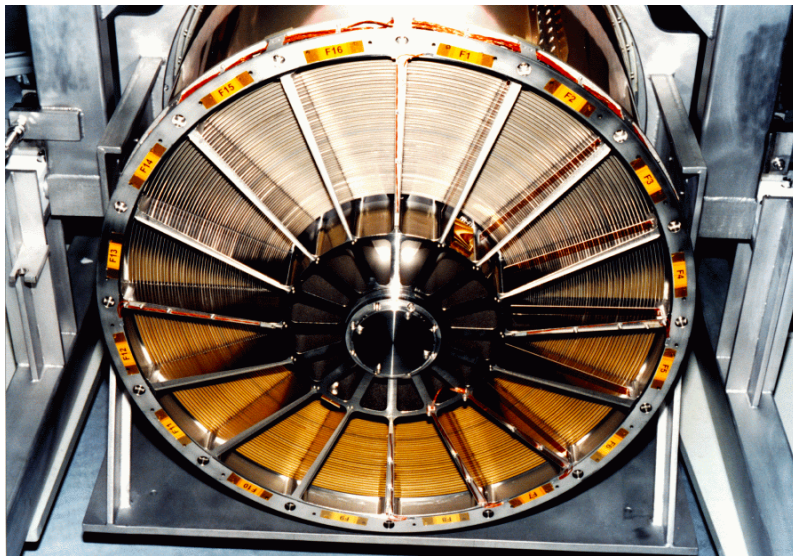
Figure 1.4: Photo of one of the X-ray mirror modules. Photons enter one end and exit the other end where they enter a detector or the Reflection Grating Arrays. (Photo courtesy of D. de Chambure, XMM-Newton Project, ESA/ESTEC).

XMM-Newton has three X-ray telescopes on board, each with 58 gold-coated Wolter I grazing-incidence mirrors nested in a coaxial and cofocal configuration as seen in Figure 1.4. This design and layout was created to obtain the highest effective area (which increases by nesting a number of mirrors) for a wide range of energies. In order to provide enough reflectivity at higher energies the mirror system has a very shallow grazing angle of 30'.

XMM-Newton contains six total science instruments: the European Photon Imaging Camera (EPIC), which includes 3 X-ray CCD cameras for imaging, photometry, and medium resolution spectroscopy; the Reflection Grating Spectrometer (RGS), which consists of two high-resolution spectrometers; and the Optical Monitor (OM), which performs optical/UV monitoring and low resolution spectroscopy. Our images were taken by EPIC using all three X-ray CCD cameras, which we will describe next.
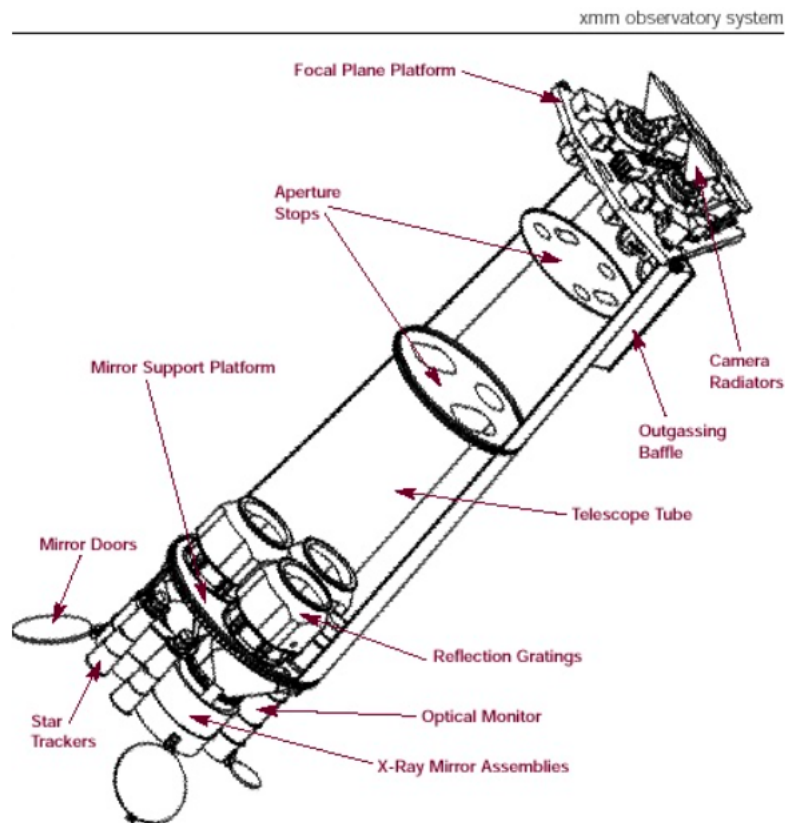
Figure 1.5: XMM-Newton spacecraft. The Focal Plane Platform (FPP) is where the two Reflection Grating Spectrometer (RGS) cameras, an EPIC PN and two EPIC MOS imaging detectors are located. The Mirror Support Platform is where the three X-ray telescopes as well as the Optical Monitor (OM) are. The OM is a separate telescope at the other end of the telescope tube from the FPP. Image from the ESA XMM-Newton website[6].

European Photon Imaging Camera (EPIC)

XMM-Newton carries three X-ray CCD cameras: two Metal Oxide Semi-conductor CCD arrays (MOS) and one pn CCD known as the pn camera (a pn CCD is a backside illuminated, 3-phase CCD on a fully depleted silicon substrate). These three instruments comprise EPIC. They are located on the Focal Plane Platform (FPP) as seen in Figure 1.5. The MOS cameras are located behind the X-ray telescopes that have the RGS gratings equipped. These gratings divert about half of the incident flux from the telescope to the RGS detectors. Thus when we also take the structural obstruction into account, the MOS cameras receive only about 44% of the incoming flux while the pn camera has an unobstructed beam of flux from the X-ray telescope.

The focal length of the X-ray telescope is 7.5 m. The angular resolution of the pn and

MOS cameras is 1.1" and 4.1" respectively. The telescope's field of view is 30 arcmin and detects an energy range of 0.15 to 15 keV. For a comprehensive description of the EPIC PSF see Read et al. (2011).

The EPIC cameras operate in photon-counting mode and produce event lists. These lists are a table with one entry line per received event which list a number of attributes such as position, arrival time, and energy. This is great for a variability study since it means we can know everything that was coming from our sources on the smallest timescales and adjust our light curve's binning to highlight what was happening at that time.

1.4   Variability

In this section we detail the mechanisms of variability in both the far-infrared and X-ray. It is important to note we are particularly interested in variability when looking at simultaneous measurements since it allows us to see how the different processes causing the variability may be correlated by comparing the variability observed in different wavelengths at the same time.

1.4.1   Far-infrared variability (Billot et al., 2012)

The study by Billot et al., 2012 (referred to as Billot12 for the remainder of this section) of the Orion Nebula Cluster (ONC) was the first photometric monitoring of YSO variability in the far-infrared. They were the first study to find that protostars do exhibit variability in the far-infrared, which was not previously known or expected since it was believed that no processes are happening on short timescales in the cold outer part of the disk, where far-IR emission originates. Thus we used their setup so we can try and corroborate their results with a new set of protostars in a different young cluster.

They used the Herschel PACS photometer in the blue (70μm) and red (160μm) wavelength channels simultaneously, spanning an area of 35' by 35'. They took two images in each epoch, a scan and cross-scan, rotating 90 degrees to filter out instrumental drifts from the extended emission. The epochs were spread out across two months (February-April 2011) lasting 2.5 days each.

To process the data, Billot12 started with the PACS standard pipeline Level 1 images and then calibrated and processed the data themselves as the standard pipeline that we used was not yet in its final version when Billot12 did their study.

Due to the highly structured extended emission of the ONC, which would make source-finding algorithms very hard to fine tune, they opted to use visual inspection of the combined blue image to identify point-like sources and found 43 objects, of which 80% were found in the red image as well. We opted for the same approach due to the similar extended structure of the Coronet Cluster.

For each point source in each epoch, they measured the photometry within a small aperture centered on the PSF (Herschel PSF discussed in Section 2.1.3) core of the source. The encircled energy (which is the energy measured within the aperture used for photometry) measured here is not the total source flux as the total flux is distributed over a large area due to the PSF shape (Section 2.1.3). To account for this, they corrected the fluxes with the aperture correction factors derived from the PSF. These correction factors are in Table 2.1 in Section 2.1.3. The aperture sizes that they used are 4 arcsecs in the blue and 8 arcsecs in the red, due to these being similar in encircled energy (48.7% for the blue and 52.7% for red as seen in Table 2.1). For the background annulus, they used inner/outer radii sizes of 6"/8" and 10"/16" for the blue and red bands respectively. To determine the flux uncertainties they used the following method: taking multiple aperture/annulus sizes around the source, the typical flux variation was used as the error. Billot12 found errors to mostly be around 5% with some reaching 20% when in areas of highly structured background. They also found errors to be higher in the red band, most likely due to the structured background and some of these sources being extended at this wavelength.

To make their light curves as reliable as possible, they deemed any light curve with a point having an error greater than 5% as "inaccurate". Of their original 43 sources, only 17 passed this selection criterion in the blue band and 6 in the red band. Also, since having only six (due to having six epochs) data points makes it difficult to separate source variability from photometric error, Billot12 only attributed flux variations greater than ~10% to a source's intrinsic variability.

With this criteria in mind, they found 8 out of 17 blue sources to have peak-to-peak flux variability with the highest observed variability to be 21%. As an example of how the far-infrared variability may look, we have included one of their variable light curves in Figure 1.6. This source was variable in both bands and showed the same trend in both. Billot12 conclude that far-infrared emission can vary on timescales as short as a couple of weeks but admit that since they were only sensitive to timescales of 10-50 days, there could have been even shorter term variability they could not see. This is where the timescales
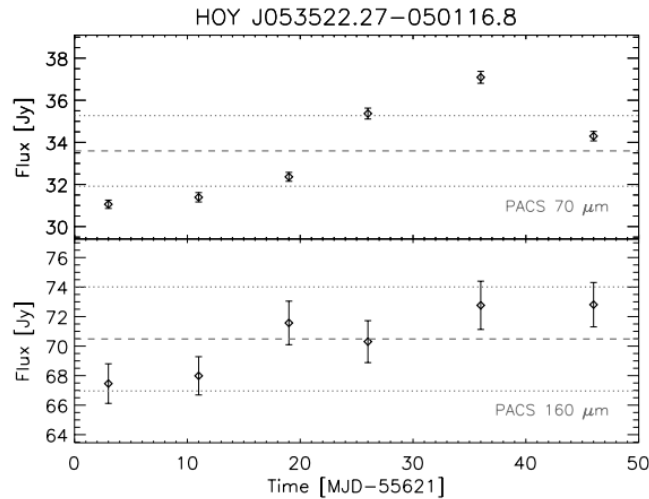
Figure 1.6: Figure 2 from Billot et al. (2012). This is the light curve of HOY J053522.27-050116.8 in the Orion Nebula, which was classified as variable by Billot et al. (2012) with a variability of 19% in the 70μm band and 12% in the 160μm band. Referring to our Section 2.3.3, this light curve is very similar to our S CrA light curve: both have small errors in the 70μm and similar variability in both bands.

of our observations fit in nicely, since we are probing timescales of 1-16 days.

Billot12 hypothesizes that the far-infrared variability could be the result of energetic photons generated in an accretion shock on an embedded protostar being reprocessed by the surrounding envelope and eventually escaping in the far-IR. The variations in the accretion luminosity due to the accretion events in the central protostar then propagate outwards and warm up the outer envelope (at distances of 10^2-10^3 AU from the central object) which would lead to detectable far-infrared variations. They also discuss another scenario presented by Flaherty & Muzerolle (2010) consisting of a variable scale height of the inner edge of the disk casting a shadow on the outer disk, which would cool down the far-IR emitting disk. Flaherty & Muzerolle (2010) tested various models that could cause this, but Billot12 pointed out that simultaneous near-IR imaging would be needed to verify these models.

1.4.2   X-ray variability

Protostellar cores are generally hidden inside enormous gas envelopes. Since radiation at energies greater than 1 keV is less affected by foreground extinction than optical light is, hard ($\sim$2-7 keV) X-rays are especially good at penetrating the thick molecular clouds and hard X-ray observations have revealed high-energy activity associated with Class I objects (Koyama et al., 1996; Vievering et al., 2019). The origin of X-ray emission

from T Tauri stars is not fully understood. It is believed the bulk is a result of coronal magnetic activity due to the hot plasma temperature (>10-30 MK) derived from their X-ray spectra (Preibisch et al., 2005) and lack of X-ray and optical/near-IR variability correlation Forbrich et al., 2007 (if they were correlated this would point towards accretion possibly being an important source of X-ray emission from YSOs). However, other studies have found that some of the X-ray emission originates from accretion shocks (Kastner et al., 2002) or shocks in the innermost part of the stellar jets (Güdel et al., 2007). But according to Preibisch et al. (2005), the data from COUP shows that accretion shocks are not the main cause of X-ray emission from T Tauri stars since the majority of the X-ray emission is hard and X-ray emission from accretion should be very soft due to the low temperature in the shock zones.

Early protostars are all well established X-ray emitters, with Class I protostars having been known for a while (e.g. Grosso et al., 1997; Imanishi et al., 2001) and Class 0 protostars more recently (e.g. Hamaguchi et al., 2005; Grosso et al., 2020). Thus these high energy processes start very early in this evolutionary sequence.

For more information about X-ray flares from young stars, see Getman's papers such as Getman et al. (2008); Getman et al. (2008); Getman & Feigelson (2021); Getman et al. (2021). Some X-ray variability studies of the Coronet Cluster are discussed in greater detail in the next section.

1.5   Coronet Cluster

For our multi-wavelength study of YSO variability, we chose the Coronet Cluster due to its proximity (149.4 ± 0.4 pc, Galli et al., 2020), young age (0.5-1 Myr, Sicilia-Aguilar et al., 2011), and well known population of YSOs. Due to these properties, it is one of the most interesting regions for studying low-mass star formation and thus it has been extensively studied already since its discovery in 1984 by Taylor & Storey in the near-infrared. This means we have plenty of past studies in various wavelengths to compare to, which allows us to already know where most of its members are and compare our photometry to past studies (we compare our far-IR photometry to the Herschel study by Sicilia-Aguilar et al., 2013 in Chapter 5). This is the first Herschel study of the Coronet Cluster looking for far-infrared variability.

The first Coronet Cluster members discovered to be variable were R CrA and T CrA

in 1960 by Herbig and they were among the first stars discovered with jets and disks (Ward-Thompson et al., 1985). The nebula surrounding R CrA had already been known to be variable since the beginning of the 20th century (Knox Shaw, 1916; Reynolds, 1916). Herbig concluded that R CrA and T CrA were young and thus any surrounding stars would be as well. This prompted an interest in the region which led to the first major optical and infrared survey of the region by Knacke et al. (1973) who discovered infrared excess around many of the variable stars, which indicated the presence of circumstellar material. They also derived the age of these variable stars to be ∼1 Myr. Later, many studies were conducted by various groups in multiple wavelengths, including in the infrared (Nutter et al., 2005; Sicilia-Aguilar et al., 2013), X-ray (Neuhäuser & Preibisch, 1997; Forbrich & Preibisch, 2007), radio (Brown, 1987), millimeter (Cazzoletti, P. et al., 2019), and optical (Galli et al., 2020).

Koyama et al. (1996) first discovered many Coronet sources in the X-ray that we will discuss in the next section: the Class I protostars IRS 1, IRS 2, IRS 5, and IRS 7, as well as the T Tauri star IRS 6.

Forbrich & Preibisch (2007) used sensitive Chandra images, the deepest X-ray image so far of the Coronet, to present a thorough review and comprehensive inventory of the X-ray source population of the Coronet Cluster, which we use as a reference multiple times throughout this paper.

In this section, we introduce the source population of the Coronet Cluster that we will be analyzing later in the paper and then discuss some relevant recent studies of the Coronet Cluster. X-ray and far-infrared images of the Coronet can be seen in Figure 1.7.

1.5.1 Source population

The population of stars in the Coronet is very well studied and for a thorough review of the Corona Australis star-forming region see Neuhäuser & Forbrich (2008). For a wider context, multi-wavelength review of the Coronet Cluster, see Peterson et al. (2011). For a deep look at the X-ray population see Forbrich & Preibisch (2007).

Using past studies and looking at our images, we chose a core sample of well known protostars at a few different evolutionary stages to photometrically analyze in this study. The sources in the central cluster are all young as it is an active star-forming region. Here

---

[7]This research has made use of ESASky, developed by the ESAC Science Data Centre (ESDC) team and maintained alongside other ESA science mission's archives at ESA's European Space Astronomy Centre (ESAC, Madrid, Spain).
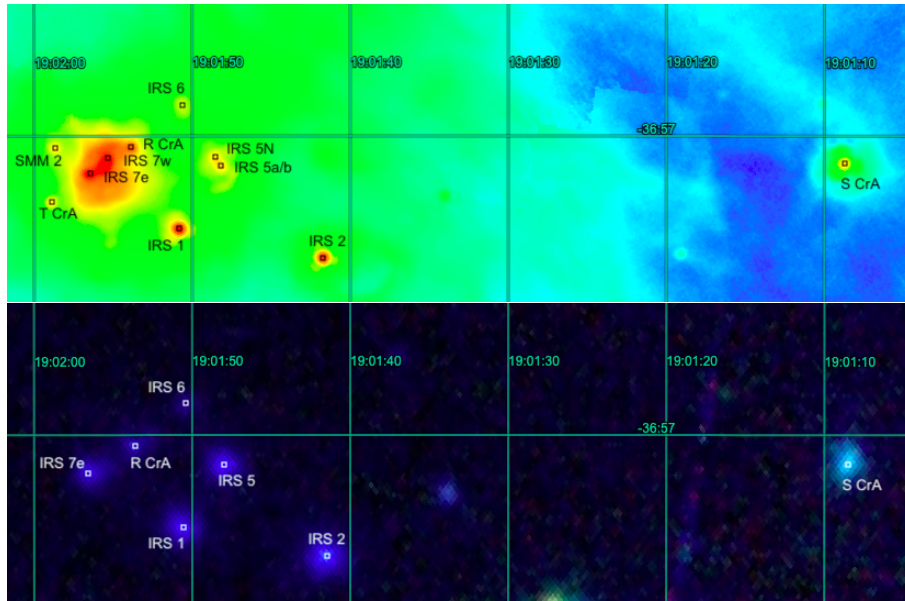
Figure 1.7: Images of the Coronet Cluster taken from ESASky[7]. Sources labeled are those we analyze in this study, discussed in Section 1.5.1. The top image is Herschel PACS 100 μm with a rainbow color scale. Bottom image is XMM-Newton EPIC RGB (red: 0.3-0.7 keV; green: 0.7-1.2 keV; blue: 1.2-7 keV).

we will introduce the protostars we focus on for this study (presented in order of youngest class to oldest). In Section 3.4, we also list all X-ray sources detected in the field of view of our XMM observations so as to have a brief overview of the variability of other stars in the region and compare generally with our results.

The IRS 7 complex

We begin with the youngest class, the candidate Class 0 protostar, IRS 7e, which was discovered by Hamaguchi et al. (2005) and proposed to be transitioning between Class 0 and Class I by Groppi et al. (2007) making it the youngest source in this study. The X-ray spectral fit performed by Forbrich & Preibisch (2007) yielded a plasma temperature of 80 MK and such a high temperature indicates that the detected X-ray emission is dominated by magnetic activity (Forbrich & Preibisch, 2007). IRS 7e was the most variable X-ray source detected by Forbrich et al. (2007) and one of the strongest far-infrared emitters detected by Sicilia-Aguilar et al. (2013).

IRS 7w is a Class I protostar (Forbrich & Preibisch, 2007) that has previously been seen to have the highest amount of far-infrared emission in the Coronet (Sicilia-Aguilar et al., 2013) and is also one of the most variable X-ray emitters (Forbrich et al., 2007).

Other components of IRS 7 are a radio source 5 arcseconds north of 7w (Brown, 1987)

as well as three additional weak radio sources (Forbrich et al., 2007), which we did not detect in our datasets.

The Class I protostars IRS 2, IRS 5, IRS 5N, IRS 1, and SMM 2

IRS 2 is an embedded young protostar with spectral type K2V (Nisini et al., 2005). Its SED indicates it is a Class I protostar (Nutter et al., 2005). Nisini et al. (2005) derived an age of about $\sim$0.5-2 x 10^6 years and a mass of $\sim$1.4-1.8 M$_\odot$.

IRS 5 is a binary with a separation of $\sim$0.75 arcsec (Nisini et al., 2005). We were not able to resolve IRS 5a and 5b with XMM or with Herschel due to angular resolution. The previous near-infrared Spitzer study of the Coronet by Peterson et al. (2011) was also not able to resolve IRS 5a/b. But they were resolved in infrared by Nisini et al. (2005) with VLT spectroscopy. However, we did detect a close source just northeast of IRS 5a/b, IRS 5N, but only in our green Herschel photometry. So for the X-ray photometry as well as the red Herschel photometry, we refer to the complex collectively as IRS 5, but for the green Herschel data we differentiate IRS 5a/b and IRS 5N. IRS 5a/b and 5N are all Class I protostars (Forbrich & Preibisch, 2007). IRS 5 has a spectral type K4 (Meyer & Wilking, 2009). Nisini et al. (2005) derived the age of IRS 5a to be $\sim$0.3-1.3 x 10^6 years and its mass to be 0.5-0.9 M$_\odot$.

IRS 1 was first discovered by Strom et al. (1974). Its SED indicates it is a Class I protostar (Forbrich & Preibisch, 2007) with a dust temperature of 30K. Nisini et al. (2005) derived IRS 1's spectral type to be K5-M0, its age to be $\sim$1-6 x 10^5 years, and a mass of $\sim$0.4-0.75 M$_\odot$.

SMM 2 is an embedded protostar (Sicilia-Aguilar et al., 2013) first detected by Wilking et al. (1997) at 2 μm. It has since been detected in a range of infrared and submillimeter wavelengths including 1.2 mm (Chini et al., 2003), 850 μm and 450 μm (Nutter et al., 2005), 1.3 mm (Peterson et al., 2011), and 100 μm and 160 μm (Sicilia-Aguilar et al., 2013). However, it was not detected in the deepest X-ray inventory of the Coronet by Forbrich & Preibisch (2007) with Chandra and we do not detect it with XMM either. Chini et al. (2003) and Nutter et al. (2005) proposed it was likely a Class I object and thus the latter assumed a disk dust temperature of 30K to calculate an envelope mass of 0.3 M$_\odot$.

The T Tauri stars S CrA and IRS 6, and the Herbig stars R CrA and T CrA

S CrA is not in the Coronet Cluster but is about 45 arcsec from the center of the Coronet and is a member of the Corona Australis star-forming region. However it is in the field of view of both of our observations and is often included in studies of the region, thus we include it in this study. S CrA is a Double Classical T Tauri star first documented in 1945 by Joy. It is known to be a visual binary with separation of 1.4 arcsec and its binary spectral types are K3 and its companion's is M0 (Prato et al., 2003; McCabe et al., 2006). Nutter et al. (2005) found the slope of the SED to be consistent with a type II YSO, indicating a temperature of 30K. Assuming this temperature, the mass of S CrA is 0.1 $M_\odot$ (Nutter et al., 2005).

IRS 6 is a binary T Tauri star with a separation of 0.6 arcsec and with spectral type M1 (Meyer & Wilking, 2009) and SED Class II (Peterson et al., 2011), though we were not able to resolve the binary. Nisini et al. (2005) derived it to have an age of 0.5-1.8 x 10^6 years. IRS 6 was found to be a weak X-ray emitter by Forbrich et al. (2006) in both the Chandra and XMM-Newton data.

R CrA is a binary Herbig Ae star also first documented in 1945 by Joy and one of the first stars in the cluster to be found to be variable (Herbig, 1960). Herbig Ae/Be stars are characterized by a strong infrared excess due to their warm circumstellar disk, are experiencing accretion, and are the more massive counterparts of T Tauri stars. R CrA's spectral type is highly debated, and estimates vary from F5 (e.g. Hillenbrand et al., 1992) and A5 (e.g. Chen et al., 1997), to B8 (e.g. Bibo et al., 1992). It has a companion star with a separation of ~18.7 AU discovered in 2019 by Cugno et al.. The age of R CrA was calculated by Sissa, E. et al. (2019) as 1.5 Myr. They also calculate the masses of the components of the binary as $M_a = 3.02 \pm 0.43$ $M_\odot$ and $M_b = 2.32 \pm 0.35$ $M_\odot$, which makes the total mass of the binary $M = 5.34 \pm 0.8$ $M_\odot$.

T CrA is a binary Herbig star with spectral type F0e (Acke & van den Ancker, 2004). Along with R CrA, it was one of the first two stars in the Coronet to be documented as variable Herbig (1960). They were also some of the first intermediate-mass stars to be discovered to have jets and disks (Ward-Thompson et al., 1985). Forbrich et al. (2007) found T CrA to be variable in the optical but barely visible in the X-ray.

1.5.2   Relevant recent studies of the Coronet Cluster

The most recent Herschel study of the Coronet Cluster was performed by Sicilia-Aguilar et al. (2013) as part of the Herschel Gould Belt study. They analyzed Herschel data in the red (160 μm) and green (100 μm) bands taken on 18 April 2011. The parameters of their study allow for a direct comparison of fluxes to ours and we will do so later in Chapter 5. They confirmed a population of very young protostars with very evolved disks. They found the brightest far-infrared peak to come from the IRS 7 complex, a binary composed of IRS 7e and IRS 7w (the latter of which is brighter in infrared). In this study they were not able to resolve IRS 5a and 5b, which have a separation of ∼0.75 arcsec (Nisini et al., 2005) and found them to be surrounded by a considerable amount of extended emission. They discuss the structure and possible reasons for the extended emission around IRS 5a/b, as well as for a few other sources. This emission is outside the scope of our study, but for further information about it, refer to Sicilia-Aguilar et al. (2013).

In 2011, Sicilia-Aguilar et al. compared optical spectroscopy with HAWK-I/VLT near-infrared imaging, and APEX/LABOCA 870μm mapping of the Coronet Cluster. They identified 18 objects with known spectral types and extinction and placed them on a color-magnitude diagram to estimate the age of the cluster as younger than previously estimated: <2 Myr, probably 0.5-1 Myr. This new younger age is consistent with many of the properties of the Coronet, such as the substantial clouds, the compactness of the region, and the embedded Class 0 and I protostars. However they also estimated that only about 50-65% of low mass stars have protoplanetary disks and an overall very low accretion rate which is actually indicative of an older population.

Forbrich et al. (2006) looked at archival X-ray images of the Coronet Cluster taken by Chandra in October 2000 and June 2003 and by XMM-Newton in April 2001 and March 2003 covering a total of 154 ks. They found nine sources with Chandra and eight with XMM, of which the three brightest were Class I protostars IRS 1, 2, and 5. They found IRS 5 to be the most variable Class I protostar and IRS 1 and 2 to exhibit more steady flux, but did not observe any discernible flares from any of these sources. They also discuss the Class 0 candidate IRS 7e, which they detected to be the most variable X-ray source in their dataset. Their focus was on low mass young stars but they also discuss the Herbig Ae star R CrA due to its very large infrared excess which indicates it is at a very early evolutionary state. Although past X-ray studies had not been able to resolve R CrA from IRS 7 and IRS 9 (Koyama et al., 1996), both the Chandra and XMM datasets do resolve

R CrA.

The first simultaneous multi-wavelength monitoring of Class I protostars was performed by Forbrich et al. (2007). They compared simultaneous X-ray, radio, near-infrared, and optical observations of the Coronet Cluster taken over the course of one week in August 2005. They found seven objects detected in all bands. Most of these sources exhibited X-ray variability and many also displayed near-IR/optical variability, but no reliable radio variability was detected. They found no time correlation between the X-ray and near-IR or optical variability. However they only had 1-2 days between each of their five epochs, and thus were only sensitive to variability on timescales of a 1-5 days. In our simultaneous monitoring, we cover a larger amount of time with spacing of 1, 2, 4, and 8 days so we may see variability on slightly longer timescales.

Chapter 2

Herschel

In this chapter we describe our Herschel observations and methods used to process them. We detail how we extracted our photometry. We then discuss the photometry of the source population we observed and will focus on for this study, first introduced in Section 1.5 of the introduction. Last we present the Herschel light curves of these sources and highlight any observed variability.

2.1 Observations and Methods

2.1.1 Observations

The Herschel PACS Photometer was operating simultaneously in the red (wavelength of 160 μm) and green (100 μm) channels with a field of view of 3.5' x 1.75' in each. Ten total images of the Coronet Cluster were taken. Two images were taken per day, a scan and a cross-scan at 90 degrees, on 2012 on March 13, 14, 16, 20, and 28. The scan and orthogonal cross-scan were recommended as they provide good sensitivity and even coverage. The choice of dates was very intentional, with separations of 1, 2, 4, and 8 days between epochs to attempt to probe multiple different timescales. Each of the ten images was taken for a duration of 2532 seconds. The SPG version was v.14.2.0, the observing mode was "scan map" and a point mode of "line scan" with medium scan speed of 20 arcsec/s which is best for bolometer performance and always used for surveys of smaller fields. Due to the time it takes Herschel to make the map, we only get one flux measurement for the entire observation epoch and so we cannot probe timescales smaller than the observation length of 2532 seconds (about 40 minutes).
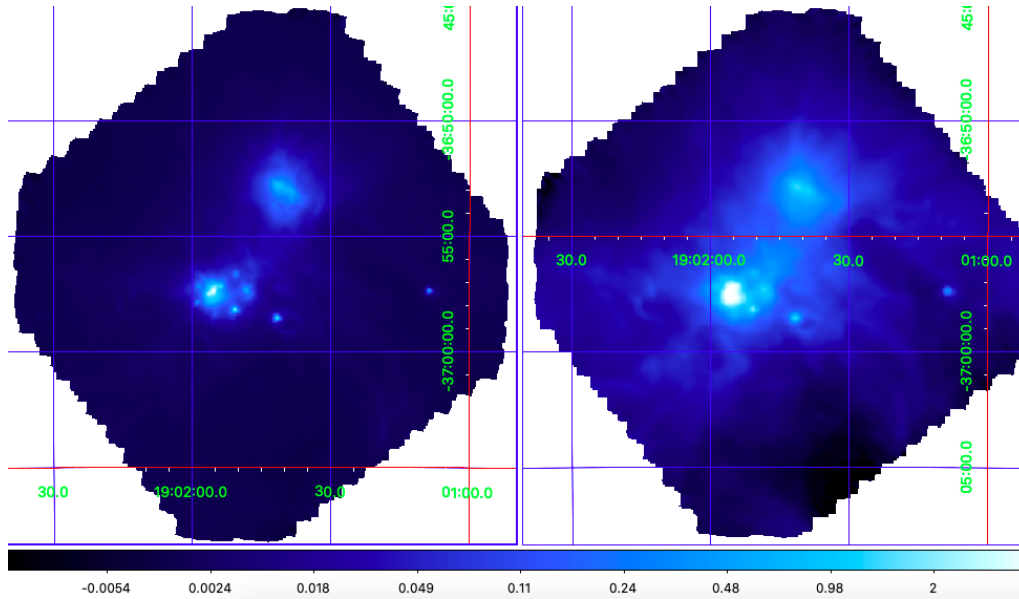
Figure 2.1: Level-3 maps (described in Section 2.1.3) made by combining all five images taken during our observing campaign in the green (100 μm) band on the left and combining all five images taken in the red (160 μm) band on the right. Map size is 20' by 20'. Color bar in units Jy/pixel.

2.1.2   Herschel Interactive Processing Environment (HIPE)

As the Herschel Interactive Processing Environment (HIPE) is now in its final version, we used the already processed data available on the Herschel Science Archive (HSA). Available on the archive are level-0 data products, which is the raw telemetry data measured by the instrument. Then there are level-1 data which is the level-0 data calibrated and converted to physical units. Level-2 data products are the result of the level-1 data being processed to such a stage that scientific analysis can be performed. Next, level-2.5 PACS photometric products are a scan and cross scan combination map of the level-2 products. These maps are produced with JScanam, Unimap, and the high-pass filter (HPF) pipelines, the last of which is recommended for point sources. We used all three maps when analyzing our data and found the HPF to be the most sensitive for our purposes. This is discussed in Section 2.1.4 and all three maps' light curves are in Figure 2.3. Level-3 products are a stacked image of all level-2.5 images taken of the same field of view with two options for the map: HPF combined with JScanam or combined with Unimap. We used the level-3 stacked image to initially identify significant point sources as it is the deepest image.

In summary, we have ten images in each of the two bands that are science ready (level-2), two from each epoch. As there are five epochs, we used the five level-2.5 products for the photometric time domain analysis.

2.1.3   Photometry

Due to the extended emission (discussed in 1.5.2) around the center of the Coronet Cluster, the point source finding algorithm given in HIPE, 'source extractor' is very difficult to adjust so that it only identifies sources and not the background nebula. Therefore we decided to pick out point-like sources by visually inspecting the deepest green map (the level-3 combination of all ten images taken at 100μm). We then did the same thing with the level-3 red map to identify sources at 160 μm. These maps are in Figure 2.1.

We looked for known YSOs and in green we found eleven total sources, nine of which are in the central region and in red we found eight sources with six in the central region. These are listed, along with their coordinates, SED class, and flux in Table 3 in Section 2.2. They are also labelled in Figure 2.2.
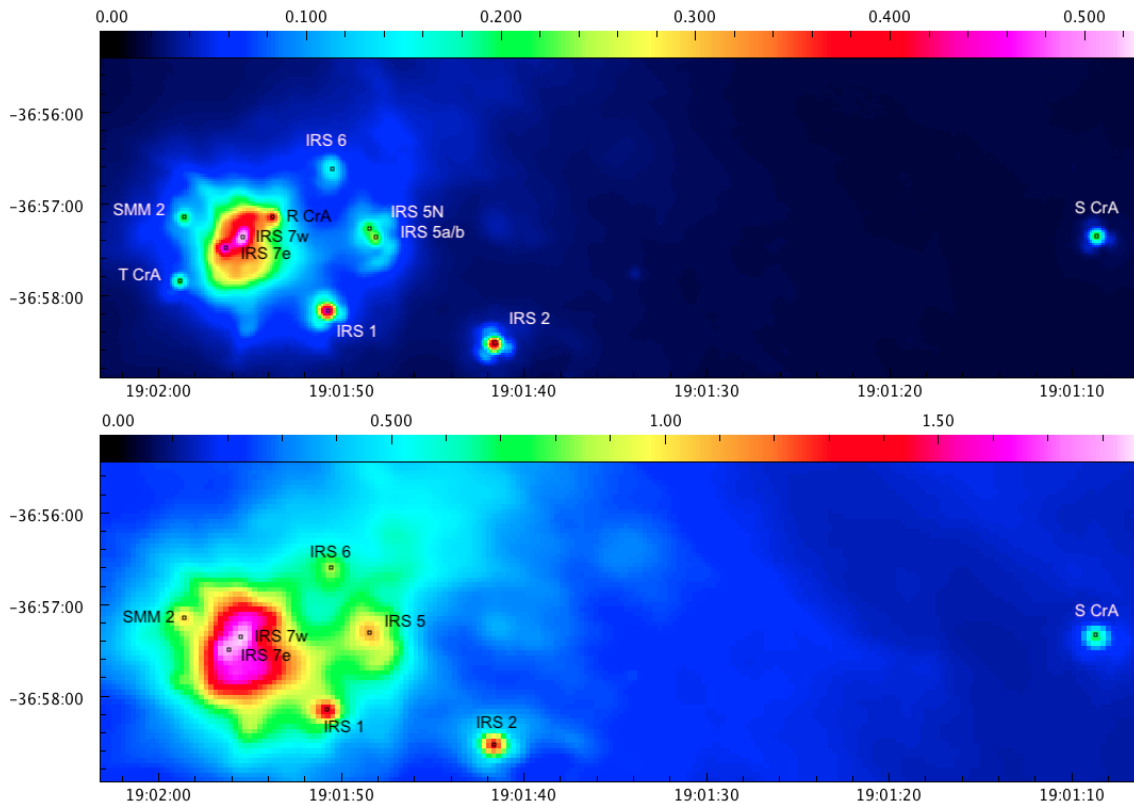
Figure 2.2: Level-3 (all epochs combined) 100 μm (green) image with sources labeled (top) and 160 μm (red) image with sources labeled (bottom). The color bars are in units of Jy/pixel.

We performed photometry on each of the sources we identified in each of the five epochs, first using the level-2.5 scan and cross scan combined HPF maps in green and then red. Then we did photometric analysis of the level-2 images to check for variability

on the short timescales between the scan and cross scan (scale of minutes) as well as to verify there were no significant errors between the scan and cross-scan images.

We used the HIPE "annular point source photometry" task to perform all of our photometry. This task measures the flux of an inner aperture and then subtracts a background measurement found by taking a flux measurement of an annulus around the central aperture (sizes of the apertures and annuli we used are discussed later in this section and listed in Table 2.2). The algorithm used for the background subtraction is DAOPhot, described in Stetson (1987) "DAOPHOT - A computer program for crowded-field stellar photometry" (this is the recommended method). The annulus shape of the background measurement is very useful in this case because a few sources are on a slope of background flux due to the central nebula and this shape allows this extra signal to cancel at least to first order (Stetson, 1987). The algorithm finds the mode, or the most frequently observed brightness value, in the annulus and multiplies it by the area of the source aperture to find the background. The mode is used because it is a maximum-likelihood estimator, meaning it minimises the probability of a large error. This method is preferred because it allows for contamination from other sources thus is better in crowded regions (Stetson, 1987). How we chose the aperture and annulus radii is described next.

The shape of the PACS Photometer PSF is characterized by the following, according to the Herschel documentation: (1) a narrow core that is round in the blue and green bands but slightly elongated in spacecraft Z direction in red, (2) a tri-lobe pattern seen in all bands due to the imperfect shape of the Herschel primary mirror, and (3) knotty structured diffraction 'rings' at sub-percent level, clearly seen in blue and green. To a small extent, the PSF wings around each source affects the determination of the source and background flux. However, due to the much greater effects of the structured background emission, which can affect the flux we measure, increasing it, it is best to choose an aperture that is small so as to minimize effects of the background emission, especially for the central Coronet sources. Our error measurement, which we discuss in Section 2.1.3, also shows how much the background affects the flux measurement since sources surrounded by structured emission will have higher errors due to the uncertainty of whether their flux is contaminated by the background or by nearby sources. This is the standard procedure recommended in the documentation, as well as by other similar studies (e.g. Billot et al., 2012).

So taking that into account, we chose a small standard aperture/annulus radius (10" aperture, 16"/23" annulus, all sizes listed in Table 2.2) for our red images that appeared

to encompass as much of the source flux as possible without any background emission. We then chose a green standard aperture/annulus size that had the closest encircled energy percentage to the red (7" aperture, 11"/16" annulus, see Table 2.2) using Table 2.1 to find the closest match in encircled energy. We started with this standard size on all of the eleven sources, however it was not the best fit for many of our sources due to some sources being too close together in the center of the cluster as well as due to the background emission in the center of the cluster. Some sources that were further out from the center of the cluster were not as affected by the structured background and so we used a larger radius for our aperture photometry so as to measure a larger encircled energy of the source.

We had to use a smaller aperture radius for IRS 5a/b and 5N as they are very close together (see Figure 2.2) and the standard size would have included flux from the neighboring source. We also used a larger background annulus that went around both of them, so one's background measurement did not include flux from the other source. And we used a smaller size aperture and annulus for R CrA and SMM 2 due to the strong structured background emission around each of them.

With S CrA, IRS 2, and IRS 1 we used a larger aperture radius since there is minimal structured emission around them and they are far away from all other sources so a small radius was not needed. A larger aperture is preferred so as to capture as much of the energy of the source as possible since the flux is distributed over a larger range than the size of the aperture. However, for all sources we correct for the percent energy encircled, as described next.

All of our sources are point sources, but the brighter ones look bigger due to the PSF. The fraction of a point source that is contained within a given aperture (called the Encircled Energy Fraction or EEF), in other words the radial profile of the PSF, is what links together the point-spread function and flux calibration. The EEFs are very carefully calculated and underlie the PACS flux calibration. When running the aperture photometry task in HIPE, only the value of the flux within that finite aperture is given. But the total flux of each source is actually distributed over a larger area. To account for this, correction factors are available as calibration files through HIPE. These have been applied to all flux measurements we obtained. The EEF, and thus correction factors, are listed in Table 2.1. Due to this aperture correction, we can directly compare measurements for different sources, so for example a source that is twice as bright as another is so not only because it has a larger aperture.

radius ['']	Encircled Energy Fraction			radius ['']	Encircled Energy Fraction		
	blue	green	red		blue	green	red
2	0.192	0.141	0.060	32	0.896	0.891	0.861
3	0.353	0.278	0.127	33	0.898	0.893	0.864
4	0.487	0.413	0.209	34	0.900	0.895	0.867
5	0.577	0.521	0.298	35	0.902	0.896	0.870
6	0.637	0.595	0.384	36	0.904	0.898	0.873
7	0.681	0.641	0.461	37	0.905	0.900	0.876
8	0.719	0.673	0.527	38	0.907	0.902	0.879
9	0.751	0.700	0.579	39	0.908	0.903	0.882
10	0.774	0.727	0.619	40	0.910	0.905	0.884
11	0.791	0.753	0.649	41	0.911	0.906	0.886
12	0.802	0.776	0.673	42	0.913	0.908	0.888
13	0.812	0.795	0.694	43	0.914	0.909	0.890
14	0.820	0.808	0.712	44	0.916	0.910	0.892
15	0.829	0.818	0.729	45	0.917	0.912	0.894
16	0.837	0.826	0.746	46	0.919	0.913	0.896
17	0.845	0.832	0.761	47	0.920	0.914	0.897
18	0.852	0.837	0.776	48	0.921	0.915	0.899
19	0.858	0.842	0.789	49	0.922	0.917	0.901
20	0.863	0.847	0.800	50	0.924	0.918	0.902
21	0.867	0.852	0.809	51	0.925	0.919	0.904
22	0.870	0.857	0.817	52	0.926	0.920	0.905
23	0.874	0.863	0.824	53	0.927	0.921	0.906
24	0.877	0.867	0.830	54	0.929	0.922	0.908
25	0.880	0.872	0.835	55	0.930	0.923	0.909
26	0.883	0.876	0.839	56	0.931	0.924	0.910
27	0.885	0.879	0.843	57	0.932	0.925	0.911
28	0.888	0.882	0.847	58	0.933	0.926	0.912
29	0.890	0.885	0.850	59	0.935	0.928	0.913
30	0.892	0.887	0.854	60	0.936	0.929	0.914
31	0.894	0.889	0.857	61	0.937	0.929	0.915

Table 2.1: Aperture correction factor applied to fluxes depending on aperture size used when extracting photometry and band. These are used by the HIPE and a thorough explanation as well as this table are in Balog et al. (2013).

For the red images, we used the equivalent aperture/annulus size to match the green's encircled energy (as taken from Table 2.1) except for with IRS 7e and 7w, where the annulus would have intersected the other source so we used a larger background annulus that encircled both sources, but the same equivalent aperture.

The same aperture and annulus size was used in each epoch for each source and was consistent when we took the photometry using different maps and when we took the level 2 photometry. The aperture size and annulus size for each source are listed in Table 2.2.

The HIPE task included an option for "centroiding" to find the center of the source before performing the photometry. This works by taking a square region with a length four times the target radius and fitting it with a 2D Gaussian plus a constant. If a fit is found, then the "centroiding" keyword is set to "success" and the coordinates are updated. We attempted centroiding on each source in each epoch and then visually inspected the

source	GREEN (arcsec)			RED (arcsec)		
	aperture	inner annulus	outer annulus	aperture	inner annulus	outer annulus
S CrA	7	11	16	10	16	23
IRS 2	7	11	16	10	16	23
IRS 5	4	15	20			
IRS 5N	4	15	20	7	22	28
IRS 6	5	7	11	8	10	16
IRS 1	7	11	16	10	16	23
R CrA	4	6	8			
IRS 7w	4	6	8	7	22	28
IRS 7e	4	4.5	6.5	7	20	24
SMM 2	4	6	8	7	9	12
T CrA	5	7	11			

Table 2.2: List of all sources of which we took Herschel photometry. Aperture and background annulus sizes used for green and then red photometry.

results, as suggested by the task literature. But due to the proximity of the central sources and the extended background emission, this did not work well on our sources. So just as Billot et al. (2012) did, we visually inspected the image to find the center of the source and used those coordinates for our photometry. The center coordinates used are listed in Table 2.3. The coordinates used for the red photometry were slightly different and listed in Table 2.4 further below. These differences are due to uncertainty in the determination of the centroid, as these sources obviously did not move on such short timescales, but the incoming flux can be slightly displaced on the detector so we wanted to measure our detected flux as precisely as possible and thus used the best fit center for the green versus red images. The same central coordinates were used between epochs and since we are in search of time dependent variability, these small differences in position between bands do not affect our results.

There was a possibility to see time-resolved variability with the Herschel data by comparing the scan and cross scan of each epoch. These time-resolved epochs are detailed in Section 4.1. They were taken concurrently with just 63 seconds between and each lasted for 2532s ($\sim$42 minutes) thus comparing them could show us if there was variability on timescales of minutes. Thus we performed the photometry task on all of the pairs of level-2 maps for each of the five epochs in the green band. In doing so we could also check for systemic errors across epochs possibly due to the task performed to combine epochs when creating the level-2.5 maps. However we found each set of scan and cross scan measurements to be consistent with the photometry of the combination (level-2.5

map) we already took. Within each epoch none of the time-resolved measurements varied by more than 3 sigma, thus we did not observe variability on this short timescale.

Error Calculation

Due to the PACS Photometer bolometer arrays being extremely stable with gain variations of 1% over a year (Billot et al., 2012), uncertainties in flux are mostly due to the background level estimates. Therefore the Herschel Data Analysis Guide (2017) recommends the following method for calculating the error for the flux measurements: "Currently the best way to determine the photometric error is to place several apertures on the background around the source, and to measure the flux within these apertures. The standard deviation of the values gives the photometric error on the source" (p.213-214). This was the procedure we followed with all of our Herschel photometry.

2.1.4   Comparison of different map types and bands

The Herschel photometry is very reliable and most error is due to background, which is how we calculated the errors on each of our flux measurements. But we still checked for other possible sources of error, first by comparing the light curves in the red and green channels. In Section 2.3 we compare the light curves of these two bands for each source and find that most of them have the same shape (and for those that don't, each data point is still within 3 sigma). As the green and red images were taken with different detectors, this helps prove the reliability of the initial detections.

The light curves presented for each source in Sections 2.3 and 4.3 were all created using the HPF map as it is recommended for point sources. However, three total maps were available so the next step we took was performing photometry on the five level-2.5 JScanam and then Unimap maps. The light curves of all three maps are in Figure 2.3. We found that the photometry of these two maps was consistent within the errors (3 sigma) of the HPF light curves, thus there is likely no error in the processing stage. We also discussed in Section 1.4.1 why Billot et al. (2012) trusted the Herschel photometry when looking for far-infrared variability.
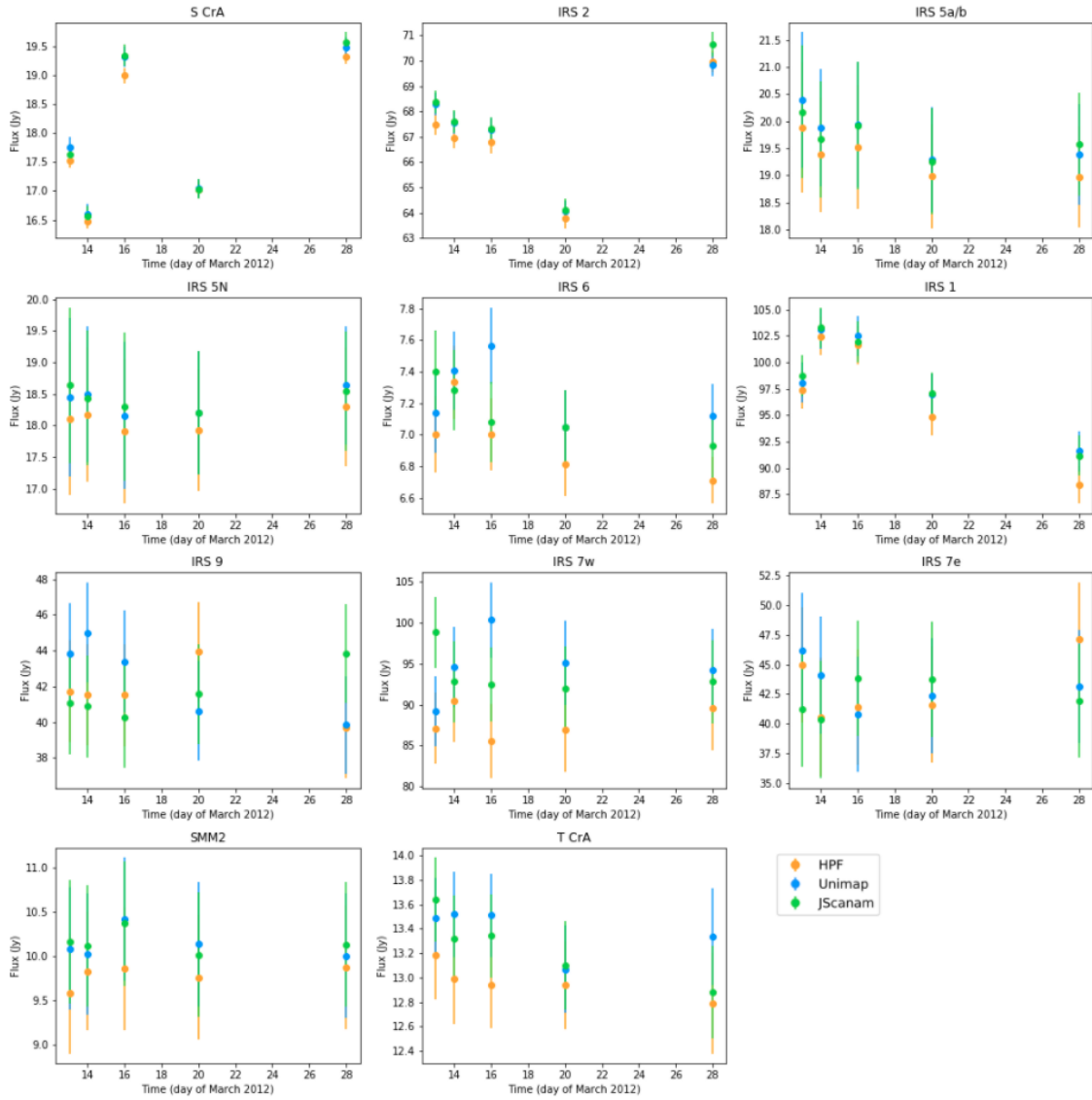
Figure 2.3: Light curves generated with each of the three maps: HPF (in orange), Unimap (in blue), and JScanam (in green) for each source in the green band.

2.2 Far-infrared source population results

All of the far-infrared sources we found are protostars. The majority of the sources found are Class I protostars. These are IRS 2, IRS 5a/b, IRS 5N, IRS 1, SMM 2, and IRS 7w. We then found two T Tauri stars: S CrA and IRS 6, as well as two Herbig Ae/Be stars: R CrA and T CrA. Lastly there is one candidate Class 0 protostar, IRS 7e. The canonical age of Class I protostars is estimated to be about 10^5 years old and the Class 0 protostars are about 10^4 years old (Nisini et al., 2005).

The average flux across epochs for each source varies between 7 Jy and 156 Jy and is listed in Table 2.3. The brightest sources in the green band are both Class I protostars:

Coordinates		Name	SED Class	Average Flux (Jy)	
				Green (100 µm)	Red (160 µm)
19:01:08.634	-36:57:20.10	S CrA	II	17.9 ± 0.1	13.0 ± 0.1
19:01:41.550	-36:58:31.60	IRS 2	I	67.0 ± 0.4	50.6 ± 1.6
19:01:48.123	-36:57:21.91	IRS 5a/b	I	19.3 ± 1.1	30.1 ± 2.1
19:01:48.457	-36:57:16.31	IRS 5N	I	18.1 ± 1.1	
19:01:50.450	-36:56:38.10	IRS 6	II	7.0 ± 0.2	10.1 ± 1.0
19:01:50.744	-36:58:10.44	IRS 1	I	97.0 ± 1.8	64.3 ± 4.6
19:01:53.809	-36:57:09.09	R CrA	II	41.7 ± 2.8	
19:01:55.411	-36:57:22.05	IRS 7w	I	87.9 ± 4.8	156 ± 21
19:01:56.390	-36:57:28.40	IRS 7e	0/I	43.1 ± 4.9	102 ± 21
19:01:58.599	-36:57:09.55	SMM 2	I	9.8 ± 0.7	14.3 ± 2.3
19:01:58.804	-36:57:50.79	T CrA	II	13.0 ± 0.4	

Table 2.3: List of all eleven green far-infrared sources and eight red sources, their SED class and our observed average flux across all five epochs in both red and green wavelengths. Sources for SED class listed in Section 1.5.1 introducing each source. In red, R CrA is a nondetection (this can be seen in Figure 2.13), IRS 5N cannot be resolved from IRS 5a/b, and T CrA is also not detected (as can be seen in Figure 2.2).

IRS 1, with an average flux across all five epochs of 97 ± 1.8 Jy, and IRS 7w, with an average flux of 88 ± 4.8 Jy. In the red band, IRS 7w is the brightest with an average flux of 156 ± 21 Jy. On average, the Class 0 and I protostars are much brighter than the Class II protostars; in red they are over five times brighter.

2.3   Far-infrared variability

To quantify whether a source is variable or not, we compared the peak to peak variability with the propagated error (Equation 2.3) and if the signal to noise (sigma) was greater than 3, we considered the source to exhibit variability. The fluxes measured in each epoch and in each band, with error, and the peak to peak variability for each source are listed in Table 2.4.

We next detail each of the sources' variability, listed starting with the youngest by SED class. We made light curves comparing the green (100μm) and red (160μm) band detections to check for consistency and to see if there is variability in one or both bands. These are seen for each source later in this chapter. We will discuss how we found S CrA, IRS 2, and IRS 1 to exhibit variability in the green band and S CrA to be the only source variable in the red. IRS 6 also exhibited some possible variability with a $2 < S/N < 3$ in green. S CrA had the highest rate of variability.

The errors given with the variability for each source were calculated using error prop-

Herschel Far-Infrared
Flux Time Series Measured at 100μm and 160μm from 2012 March

Coordinates	Source Name	Flux (Jy)					Flux Variability
		March 13	March 14	March 16	March 20	March 28	
				PACS 100 μm (green)			
19:01:08.634 -36:57:20.10	S CrA	17.5 ± 0.1	16.5 ± 0.1	19.0 ± 0.1	17.0 ± 0.1	19.3 ± 0.1	**17% ± 1%**
19:01:41.550 -36:58:31.60	IRS 2	67.5 ± 0.4	67.0 ± 0.4	66.8 ± 0.4	63.8 ± 0.4	70.0 ± 0.4	**10% ± 1%**
19:01:48.123 -36:57:21.91	IRS 5a/b	19.9 ± 1.2	19.4 ± 1.1	19.5 ± 1.1	19.0 ± 1.0	19.0 ± 0.9	[5% ± 8%]
19:01:48.457 -36:57:16.31	IRS 5N	18.1 ± 1.2	18.2 ± 1.1	17.9 ± 1.1	17.9 ± 1.0	18.3 ± 0.9	[2% ± 8%]
19:01:50.450 -36:56:38.10	IRS 6	7.0 ± 0.2	7.3 ± 0.2	7.0 ± 0.2	6.8 ± 0.2	6.7 ± 0.1	[9% ± 4%]
19:01:50.744 -36:58:10.44	IRS 1	97.4 ± 1.8	102.5 ± 1.8	101.6 ± 1.8	94.8 ± 1.8	88.4 ± 1.8	**16% ± 3%**
19:01:53.809 -36:57:09.09	R CrA	41.7 ± 2.8	41.5 ± 2.8	41.5 ± 2.9	43.9 ± 2.8	39.7 ± 2.8	[11% ± 11%]
19:01:55.411 -36:57:22.05	IRS 7w	87.1 ± 4.3	90.4 ± 5.0	85.5 ± 4.5	86.9 ± 5.2	89.6 ± 5.2	[6% ± 8%]
19:01:56.390 -36:57:28.40	IRS 7e	45.0 ± 4.9	40.6 ± 5.0	41.4 ± 4.9	41.6 ± 4.9	47.1 ± 4.8	[16% ± 18%]
19:01:58.599 -36:57:09.55	SMM 2	9.6 ± 0.7	9.8 ± 0.7	9.9 ± 0.7	9.8 ± 0.7	9.9 ± 0.7	[3% ± 10%]
19:01:58.804 -36:57:50.79	T CrA	13.2 ± 0.4	13.0 ± 0.4	12.9 ± 0.4	12.9 ± 0.4	12.8 ± 0.4	[3% ± 4%]
				PACS 160 μm (red)			
19:01:08.600 -36:57:21.30	S CrA	13.1 ± 0.1	12.4 ± 0.1	13.5 ± 0.1	12.6 ± 0.1	13.4 ± 0.1	**9% ± 1%**
19:01:41.644 -36:58:31.07	IRS 2	50.8 ± 1.6	50.4 ± 1.6	49.7 ± 1.6	49.1 ± 1.6	52.8 ± 1.7	[8% ± 5%]
19:01:48.466 -36:57:18.62	IRS 5	30.1 ± 2.0	29.5 ± 2.2	31.2 ± 2.1	30.6 ± 2.1	29.3 ± 2.1	[6% ± 10%]
19:01:50.450 -36:56:34.90	IRS 6	10.3 ± 1.1	10.2 ± 1.1	9.9 ± 1.1	10.2 ± 1.0	10.0 ± 0.9	[5% ± 16%]
19:01:50.928 -36:58:09.06	IRS 1	64.0 ± 4.8	67.0 ± 4.6	65.3 ± 4.7	63.9 ± 4.4	61.4 ± 4.5	[9% ± 11%]
19:01:55.411 -36:57:22.05	IRS 7w	154 ± 21	159 ± 21	161 ± 21	153 ± 22	152 ± 21	[6% ± 20%]
19:01:56.390 -36:57:28.40	IRS 7e	101 ± 21	102 ± 21	99 ± 21	104 ± 22	104 ± 21	[4% ± 31%]
19:01:58.599 -36:57:09.55	SMM 2	14.7 ± 2.4	14.1 ± 2.3	14.7 ± 2.3	15.1 ± 2.3	13.1 ± 2.3	[16% ± 27%]

Table 2.4: List of the aperture corrected fluxes detected in each epoch for all eleven green sources and eight red sources. The last column lists the peak to peak variability for each source in each band. Variability with a signal to noise < 3 is not considered significant and is listed in brackets. Significant variability is in bold. The error attached for the variability was calculated using the error propagation equation (Equation 2.3).

agation. We took the standard error propagation equation (Equation 2.1) and applied the peak to peak variability equation (Equation 2.2), thus deriving Equation 2.3 for our error propagation.

$$\Delta f = \pm \sqrt{\sum_{i=1}^{n} \left(\frac{\delta f}{\delta x_i} \right)^2 (\delta x_i)^2} \tag{2.1}$$

$$f_{\text{Flux Variability}} = \frac{\text{max flux}}{\text{min flux}} - 1 \tag{2.2}$$

$$\Delta_{\text{Flux Variability}} = \frac{\text{max flux}}{\text{min flux}} \sqrt{\left(\frac{\text{error of max flux}}{\text{max flux}} \right)^2 + \left(\frac{\text{error of min flux}}{\text{min flux}} \right)^2} \tag{2.3}$$

2.3.1   The Class 0 protostar IRS 7e

As the source in the earliest evolutionary stage, IRS 7e is a Class 0 protostar that had a peak to peak far-infrared variability of 16% ± 18% in the green band and 4% ± 31% in the red band. Due to the very low signal to noise ratio, we cannot say if the source is

variable or not in the far-infrared.
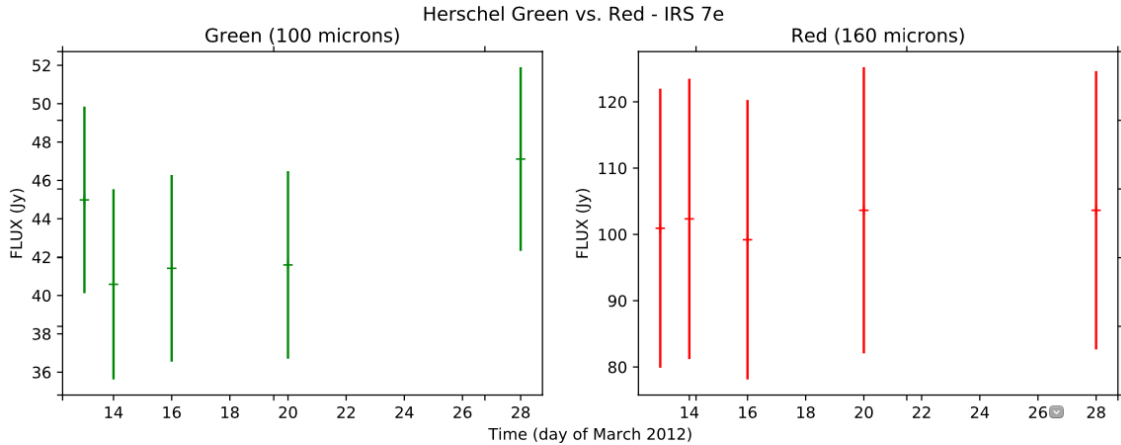
Figure 2.4: Green band (100 μm) and red band (160 μm) Herschel light curves of IRS 7e.

2.3.2   The Class I protostars IRS 2, IRS 5a/b, IRS 5N, IRS 1, IRS 7w, and SMM 2

IRS 2's light curves in both the red and green bands show decreasing flux in the first four epochs with a spike in the final epoch. The measured peak to peak variability of this spike is 10% $\pm$ 1% in green and 8% $\pm$ 5% in red. With a high signal to noise of 10 in green (1.5 in red) we classify IRS 2 as having exhibited variability during our green far-infrared observations.
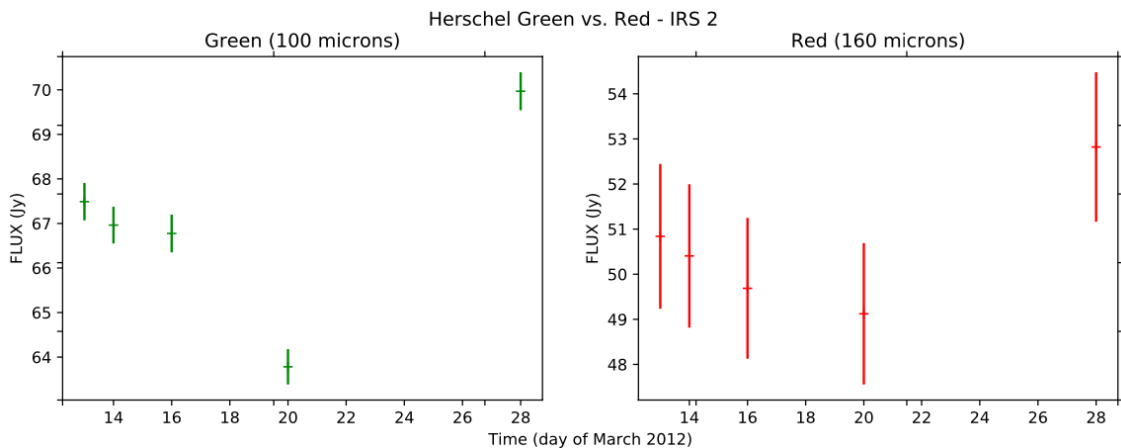
Figure 2.5: Green band (100 μm) and red band (160 μm) Herschel light curves of IRS 2.

IRS 5a/b had variability in the green band of 5% $\pm$ 8% and IRS 5N had green band variability of 2% $\pm$ 8%. IRS 5a/b and 5N were not resolvable in the red band, so the photometry taken of both has a variability of 6% $\pm$ 10%. None of these had an S/N over

1, so we classify them both as not variable in the far-infrared for this observation set.
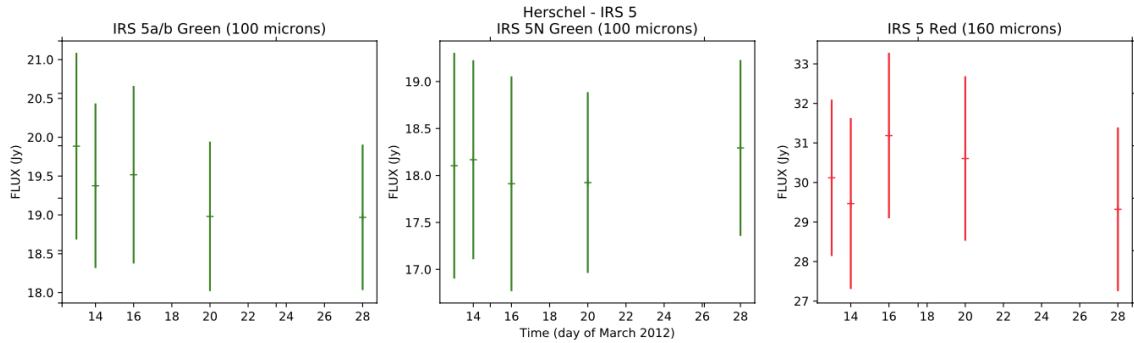
Figure 2.6: Green band (100 μm) and red band (160 μm) Herschel light curves of IRS 5. IRS 5a/b and 5N were resolvable in the images taken in the green band, so those light curves are listed separately.

IRS 1 exhibits 16% $\pm$ 3% variability in green and 9% $\pm$ 11% variability in red. In the green light curve, we see a peak in the second epoch and then gradually the flux diminishes, however in the red the errors are too large to discern a shape. This is a nice example where we see both the rise and the fall of the flare and it gives us possible timescales of a flare (though we cannot be sure what was happening between epochs), but it appears we can see a far-infrared flare on timescales of about 6-7 days.
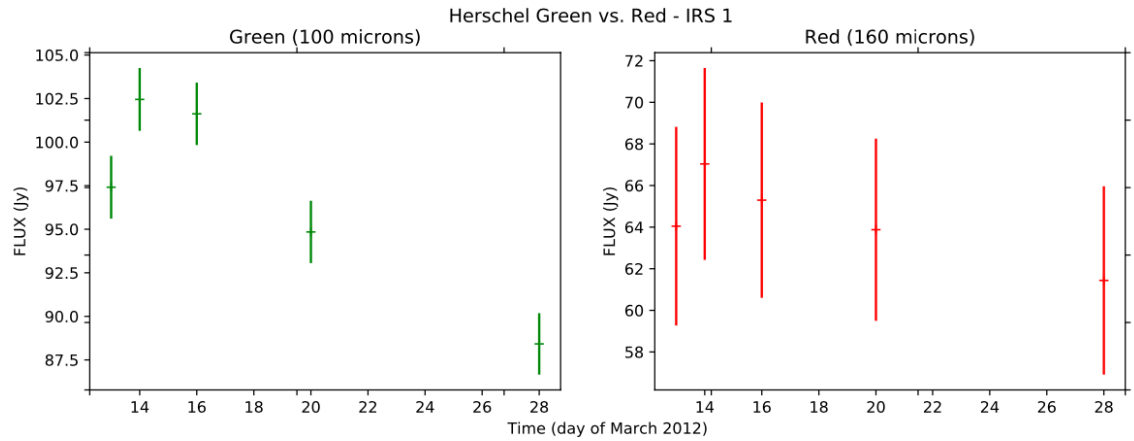
Figure 2.7: Green band (100 μm) and red band (160 μm) Herschel light curves of IRS 1.

IRS 7w had a measured far-infrared variability in the green band of 6% $\pm$ 8% and red band variability of 6% $\pm$ 20%. With such high errors and neither measurement having S/N > 1, we do not consider this source variable during our observations.
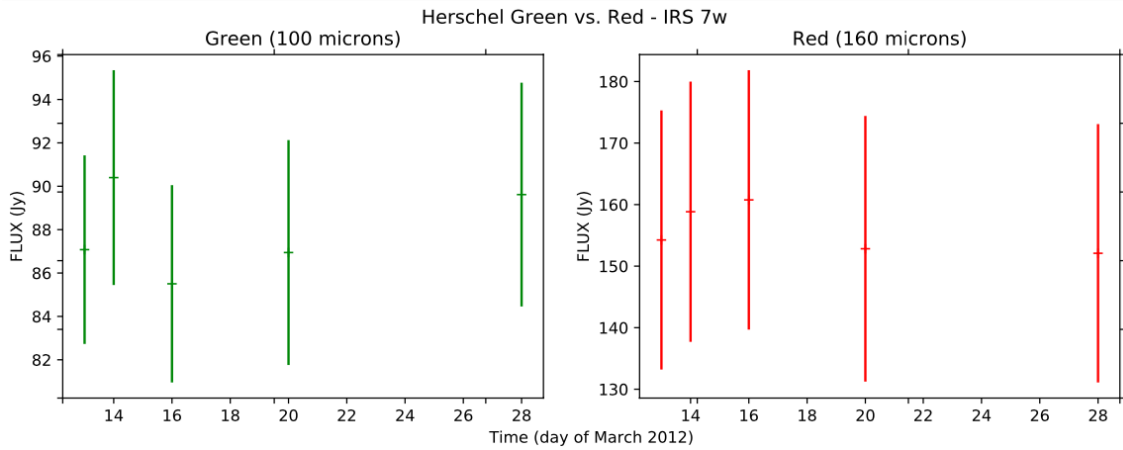
Figure 2.8: Green band (100 μm) and red band (160 μm) Herschel light curves of IRS 7w.

SMM 2 has a variability of $3\% \pm 10\%$ in green and $16\% \pm 27\%$ red. Neither observation has S/N > 1 so we do not classify this Class I protostar as variable.
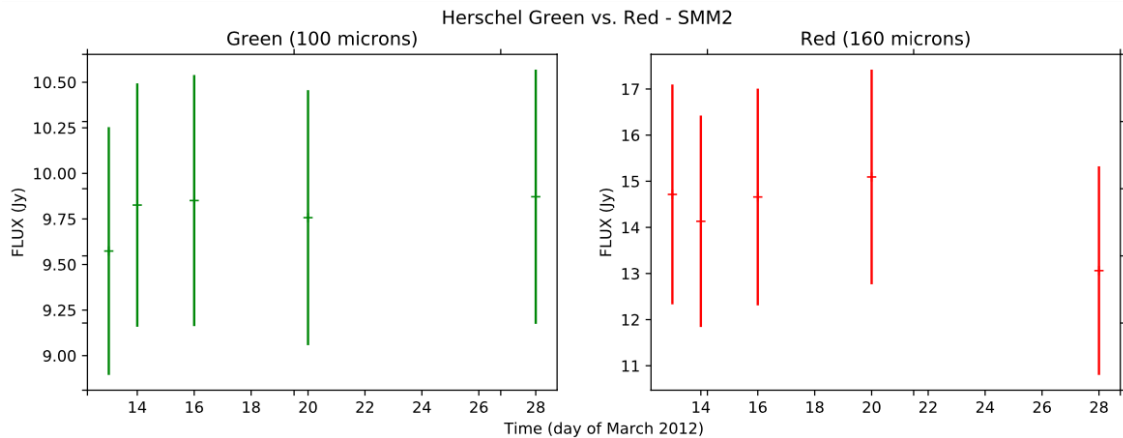
Figure 2.9: Green band (100 μm) and red band (160 μm) Herschel light curves of SMM 2.

2.3.3 The T Tauri stars S CrA and IRS 6, and the Herbig stars R CrA and T CrA

S CrA is a T Tauri star with $17\% \pm 1\%$ peak to peak variability in green and $9\% \pm 1\%$ variability in red. Though the variability differs, the shape of the light curve is the same in both, which helps strengthen the reliability of our data. S CrA is also the only source with detectable variability (S/N > 3) in red.
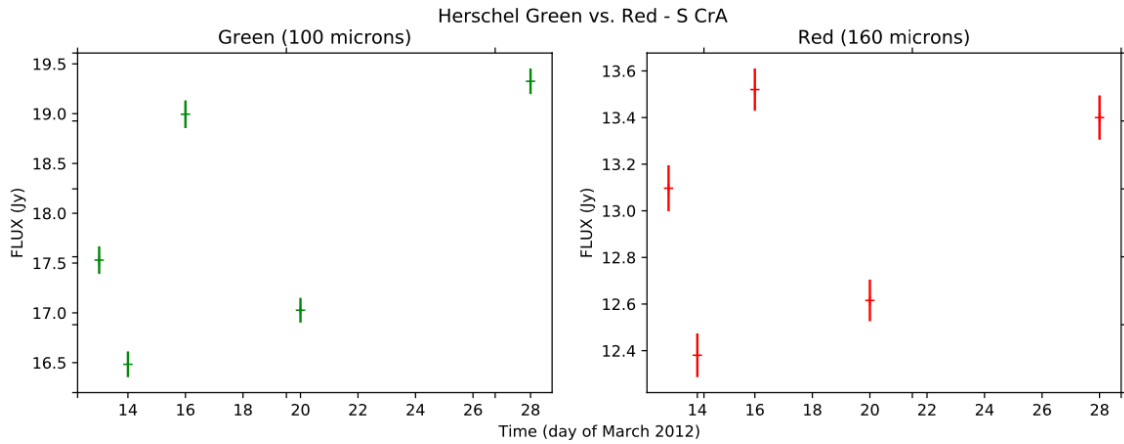
Figure 2.10: Green band (100 μm) and red band (160 μm) Herschel light curves of S CrA.

IRS 6 is a T Tauri star with 9% $\pm$ 4% variability in green and 5% $\pm$ 16% variability in red. Due to the large errors of the red photometry, we cannot be sure if the two light curves follow the same pattern in change of flux. In green, errors are moderately high with 2 < S/N < 3, so IRS 6 seems to exhibit some variability.
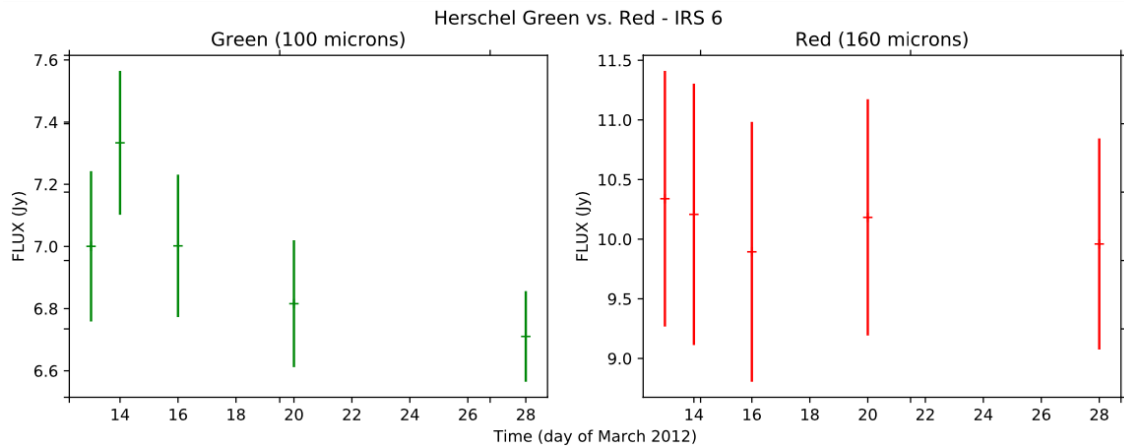
Figure 2.11: Green band (100 μm) and red band (160 μm) Herschel light curves of IRS 6.

The Herbig Ae star R CrA was not observed in the red band because the angular resolution (11.3") is less than in green (6.8") and it is not resolvable. This can be seen in Figure 2.13 where we have a side by side comparison of the location of R CrA in the green versus the red image. In the green, it had a variability of 11% $\pm$ 11% with a possible peak in the fourth epoch. The high errors are due to the complex emission surrounding R CrA, as well as its close proximity to IRS 7w and 7e. Because of these errors we cannot say if R CrA was variable during our observation.
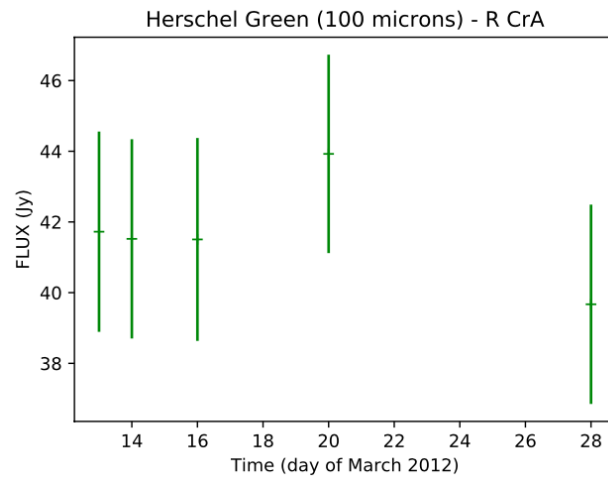
Figure 2.12: Green band (100 μm) Herschel light curve of R CrA.
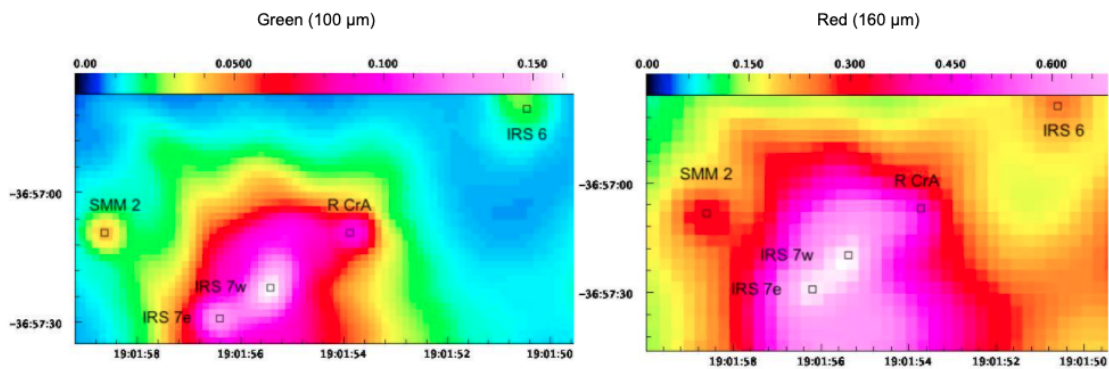
Figure 2.13: The location of R CrA is labelled in both images. On the left is the green image and on the right is the red, both from the first epoch (R CrA was not variable and all five epochs appear the same). We can see that in the red, R CrA is not detected, due to angular resolution. The units of the color bars are Jy/pixel.

T CrA was not visible in the red band. In the green, it had a variability of 3% ± 4%. With this S/N < 1, we do not consider it variable.
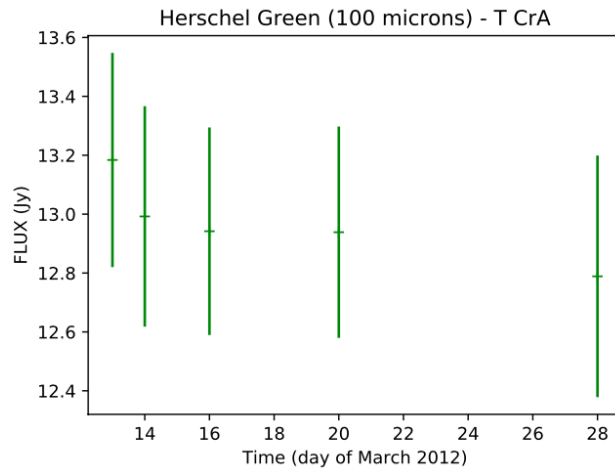
Figure 2.14: Green band (100 μm) Herschel light curve of T CrA.

In summary, the Herschel observations had a duration of ~2.5 ks for each epoch. During our observations the Herschel PACS photometer was operating simultaneously in the green (100 μm) and red (160μm) channels. We used the already processed Herschel images available on the HSA to conduct our photometry. Using the image taken in the green band, we identified and then extracted the photometry of eleven sources, of which nine are in the central region of the Coronet Cluster. In the red band image we detected eight of those sources. All sources are previously known far-infrared emitters. The overall brightest sources in green were the Class I protostars IRS 1 and IRS 7w. The brightest sources in red were IRS 7w and IRS 7e. On average, the Class 0 and I protostars were much brighter than the Class II protostars. We next looked for variability by plotting light curves of all five observed epochs in the green and red channels. We found three variable sources in green: S CrA, IRS 2, and IRS 1, and only one variable red source: S CrA. The most variable source was S CrA in both bands with 17% $\pm$ 1% peak to peak variability in green and 9% $\pm$ 1% in red.

Chapter 3

XMM-Newton

In this chapter we describe our XMM observations and the methods we used to process them. We detail how we extracted our photometry. We then discuss the source population we observed in the X-ray and will focus on for this study, first introduced in Section 1.5 of the introduction. We also list the source detections found in the field of view of our observation using the 4XMM Source Catalogue (Section 3.4). Lastly we present the XMM light curves of our sample of sources and highlight any observed variability.

3.1 Observations and Methods
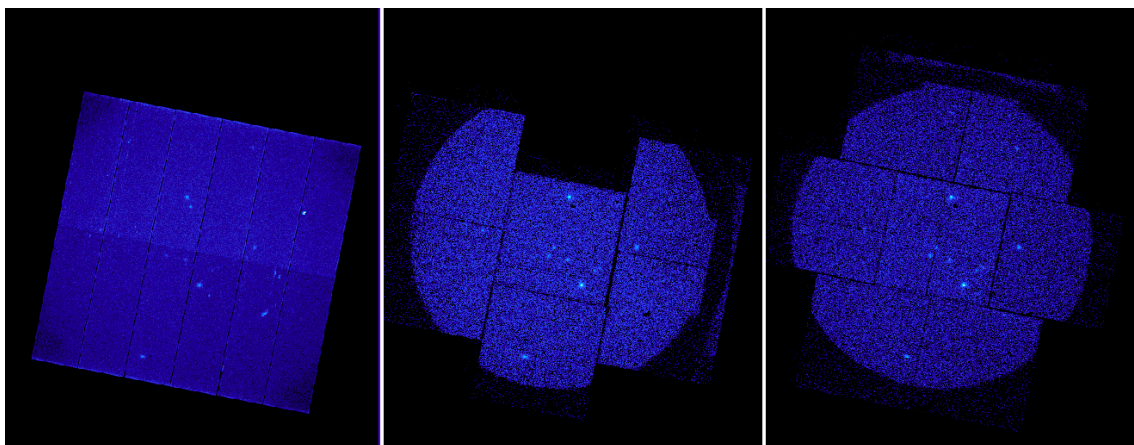
Figure 3.1: Image taken by XMM-Newton on the first day of observing, March 13 2012 with the pn detector (left), MOS1 detector (center), and MOS2 detector (right).

3.1.1   Observations

The XMM-Newton EPIC cameras were observing the Coronet Cluster simultaneously with the Herschel PACS photometer. Each of the three cameras were operating and recorded an event list including timestamps and energies during the observing time on each of the five days. The length of the observation varied per camera and day between 5041 and 8628 seconds (or about 1.5 to 2.5 hours). The exact observation lengths are listed in Table 3.1 below. The cameras all ran in full frame mode with the THIN1 filter.

	13 Mar 2012	14 Mar 2012	16 Mar 2012	20 Mar 2012	28 Mar 2012
pn	6685	6840	5041	7041	5041
MOS1	6315	8421	6622	8622	6623
MOS2	6330	8426	6627	8628	6628

Table 3.1: Duration in seconds of each exposure from each camera per epoch. Date in 2012.

An important note is that in the first epoch, the pn camera and the MOS cameras were not running concurrently. Each of the three cameras was observing for about 2 hours, but the pn camera started observing just 30 minutes before the MOS cameras stopped, leaving an overlap of just one time bin in our 1200 second light curves. This is discussed in greater detail in Section 4.1 along with figures. As a result, the first epoch is not expected to necessarily match between cameras, and could allow us to see variability on timescales of just minutes or hours if there are differences between the pn and MOS camera's light curves.
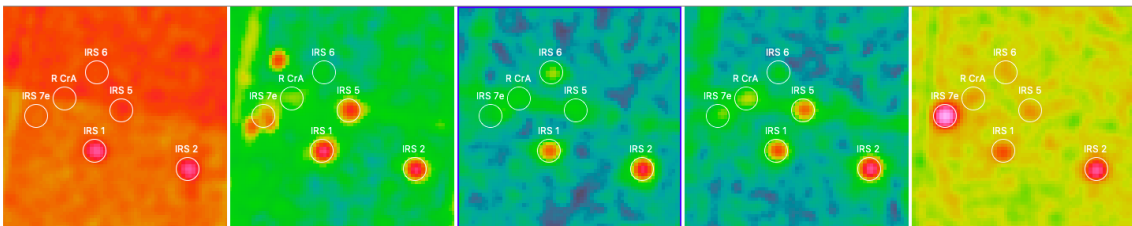
Figure 3.2: Image taken by the XMM Newton pn detector of the Coronet Cluster on each of the five observing days. Order from left to right: 2012 March 13, 14, 16, 20, and 28. The color scale is the same in all five images with red/yellow being areas with higher count rates and blue/green being lower count rates.

3.1.2 Science Analysis System (SAS)

The Science Analysis System (SAS) was developed by the Survey Science Centre (SSC) and Science Operations Centre (SOC). It is a suite of about 125 programs and scripts developed to perform data reduction, extraction, and analysis on XMM-Newton data. The Pipeline Processing System (PPS) is a superset of the SAS suite and Perl scripts maintained and updated by the SOC and the Guest Observer Facility at the NASA/Goddard Space Flight Center.

SAS creates detector response files and provides barycentric corrected event timing information. SAS also includes source-detection software for the European Photon Imaging Camera (EPIC) and the Optical Monitor telescope (OM). After downloading our Observation Data Files (ODF) and PPS science files, we used SAS for both of its main uses to create calibrated event lists and to extract light curves.

3.1.3 Photometry

To make a light curve we first created an image using the event list via the SAS command "evselect". We looked at Figure 1.7 to locate all visible Coronet Cluster sources. Once we had the central coordinates, we chose an aperture and annulus size that would encircle as much visible flux as possible without overlapping any other sources. The same size was used for all sources and is described next.

For the light curve extraction, we also used the SAS command "evselect" but to pick out good events and make a source+background light curve. We chose to produce a light curve with a rates column, versus a counts column. The aperture size had a radius of 13.5 arcsecs as this was the largest it could be for all sources without overlap. The encircled energy (as described in Section 2.1.3) for this size aperture is 0.65 and the SAS task we use when extracting the light curve automatically applies this correction. As the data is a continuous event list, we then chose a bin size for the light curve. We tested with many sizes, trying to make sure the errors were not too high (if the bin size is too small), but without missing any important variability (if the bin size is too large). We found a bin size of 1200 seconds or 20 minutes to be optimal. This was used when creating light curves of each individual epoch, seen in Section 3.3.1. We also performed the photometry using a bin that encompassed the entire epoch for later comparison to the Herschel data, as Herschel provides one flux measurements for the entire epoch.

We next used "evselect" to extract a background light curve using the same selected

central coordinates and bin size. The background annulus had an inner radius of 16 arcsecs and an outer radius of 22.5 arcsecs, again with this being the largest annulus we tried that did not overlap other sources or annuli.

The last command necessary for creating a light curve is "epiclccorr". It corrects for vignetting (which is a reduction in brightness around the periphery of a camera due to the mirror placement and geometry of the telescope), bad pixels, PSF variation and quantum efficiency, as well as for variations affecting the stability of the detection within the exposure, like dead time and Good Time Intervals (GTIs, or the interval when the telescope was operating properly). It takes in the files created for the first two commands and outputs a final background corrected light curve.

Since the final length of observation is different between epochs, the amount of bins also varies. The first, second and fourth epochs are about 7000s, or about 2 hours in length, so we have 6 bins of 20 minutes each. The third and fifth epochs are about 5000s long, or 83 minutes, so there are only 4 bins of 20 minutes each. The exact lengths of observation are listed in Table 3.1 above. In Section 3.3.1 we have the light curves for each source and we can see that there are a different number of data points for the epochs with different exposure times.

3.1.4   Comparison of different detectors

We created light curves using the photometry from each of the images taken with each of the three cameras, which all ran independently of each other. The light curves we used to quantify our variability in Section 3.3 are all from the pn detector since it has an unobstructed view and therefore the higher count rates and better accuracy of count rates. But we then compared the pn detector light curves with the MOS1 and MOS2 light curves as a way to check for error from the detector. We could not average the three detectors' measurements together because we only looked at count rates, not flux, and count rates for different instruments cannot be directly averaged

Most of the full-epoch binned light curves have the same shape except where we cannot compare shape due to non-detections. The one source where the light curves from the different cameras do not follow the same pattern is IRS 5, and it is only epoch 1 that does not match. One possible reason, as we previously mentioned and later detail in Section 4.1 is that the pn and MOS cameras were not running concurrently in the first epoch, so different flux measurements are not totally unexpected and could even be indicative of

short timescale variability. However, since the MOS cameras also do not have the same shape light curve, it could just be due to error since the MOS camera's measurements are still within 3 sigma of each other in that epoch, thus this difference is likely not significant.

The pn light curve for IRS 6 appears to have a much larger flare in the third epoch than MOS1 and MOS2 have. Since the MOS cameras only receive about 44% of the incoming flux and the pn camera is unobstructed, it is not surprising for the pn fluxes to be higher, however for IRS 6 the MOS cameras measured have a count rate that is about 27% of the pn count rate. However, since all other epochs for all three cameras had flux measurements within 3 sigma of zero, rendering them non-detections and effectively zero, yet all three cameras had a flare in the third epoch of between four and ten times the average flux of the other epochs, this similarity in shape and pattern helps verify that IRS 6 did in fact flare in the third epoch, we just cannot be sure by how much. Since we found no systematic variations in the shape of the light curves between pn and MOS, this helps us trust the light curves and our calculated errors.

3.2   X-ray source population results

We used the 4XMM Serendipitous Source Catalogue to identify all of the sources in the field of view of our observations. First we discuss the sources in the central Coronet Cluster. Of the eleven sources we identified with Herschel, we detected seven with XMM (the nondetections are discussed in Section 4.2, which compares the source populations in the different bands). These are listed in Table 3.2 along with the average flux from each detector. Not all sources were detected in all five epochs (for details see Table 3.3) so the average is of the epochs detected. Since the flux rate is an average, we calculated the errors listed using the error propagation equation 3.1 as applied to the errors from the fluxes in the epochs that the source was detected in.

$$\text{Delta}_{\text{Flux Rate}} = \sqrt{\frac{1}{N} \sum_{i}^{N} error_{i}^{2}} \tag{3.1}$$

All of the X-ray sources that we found in the Coronet are protostars. Three of the sources found are Class I protostars, these being IRS 2, IRS 5, and IRS 1 and two are Class II protostars, these being the T Tauri stars S CrA and IRS 6. We also detected one Herbig Ae star, R CrA, and one Class 0 protostar, IRS 7e.

XMM-Newton Sources and average count rates

Coordinates		Name	Average Flux Rate (counts/ksec)		
			pn	MOS1	MOS2
19:01:08.600	-36:57:21.30	S CrA	135 ± 12	35 ± 5	39 ± 4
19:01:41.550	-36:58:31.60	IRS 2	131 ± 9	45 ± 4	44 ± 4
19:01:48.020	-36:57:22.40	IRS 5	164 ± 16	23 ± 3	24 ± 3
19:01:50.450	-36:56:38.10	IRS 6	28 ± 4	6 ± 2	9 ± 2
19:01:50.660	-36:58:09.90	IRS 1	87 ± 8	30 ± 3	34 ± 3
19:01:53.670	-36:57:08.30	R CrA	51 ± 11	8 ± 2	6 ± 1
19:01:56.390	-36:57:28.40	IRS 7e	111 ± 8	95 ± 5	33 ± 3

Table 3.2: Table of all detected XMM sources, their coordinates and names, and their average fluxes detected by each camera.

We list the epoch-averaged fluxes detected for each source in Table 3.2 as detected by each of the cameras. However, since the MOS cameras only receive only 44% of the incident flux, we consider the pn camera to be the most reliable for flux and will use those count rates when discussing the brightest sources and also later in our general analysis. We will, however, use the MOS detections later in Section 3.3 when looking at relative variability.

The average count rate of our sources is between 27 and 163 counts/ksec. The overall brightest source detected by the pn camera was IRS 5 with an average flux of 163.8 ± 16.5 counts/ksec although the brightest single detection came from IRS 7e in the fifth epoch with a flux of 306.1 ± 13.1 counts/ksec (see Table 3.3), which we will discuss in greater detail when we look at variability in Section 3.3.1. Overall the Class I sources were brighter than the Class II sources (on average 78% higher flux).

Not all sources were detected in all epochs. Any detections with S/N < 3 were considered non-detections and replaced with an upper limit of 3 sigma as seen in Table 3.3.

We did detect IRS 7w but only in the third epoch with all three cameras. Due to its proximity to R CrA and IRS 7e, taking the photometry would be quite difficult, especially getting an accurate background measurement. A more complicated photometry extraction is outside the scope of this work, thus we did not extract this photometry, but note it in our future work in Section 7.

3.3 X-ray variability

Of our core seven sources, all exhibited some level of X-ray variability, which is to be expected in young stars. The most variable was the candidate Class 0 protostar, IRS 7e,

which had a flare in the final epoch of 10-36 times the flux seen in the other epochs.

In this section we will discuss the variability of all sources by looking at the light curves of the count rate as measured by each of the three XMM cameras. We present two different time binnings, the first being a bin of the entire length of the observation from each of the five epochs, allowing us to search for variability on timescales of days to weeks. Then we will look at the light curves with a time resolution of 1200 seconds (20 minutes) which may give insight into variability on the scale of minutes to hours.

			XMM-Newton X-ray					
			Flux Time Series from 2012 March					
Coordinates		Source Name	Rate (counts/ksec)					Peak to Peak Variability
			March 13	March 14	March 16	March 20	March 28	
			pn detctor					
19:01:08.600	-36:57:21.30	S CrA	258 ± 20	117 ± 8	104 ± 9	54 ± 6	143 ± 13	380% ± 60%
19:01:41.550	-36:58:31.60	IRS 2	166 ± 13	99 ± 6	124 ± 8	127 ± 6	139 ± 10	70% ± 20%
19:01:48.020	-36:57:22.40	IRS 5	251 ± 27	258 ± 16	53 ± 9	150 ± 11	108 ± 14	390% ± 90%
19:01:50.450	-36:56:38.10	IRS 6	<25	<6	28 ± 4	<5	<17	>420%
19:01:50.660	-36:58:09.90	IRS 1	156 ± 13	100 ± 6	67 ± 6	58 ± 4	55 ± 7	180% ± 40%
19:01:53.670	-36:57:08.30	R CrA	106 ± 19	20 ± 6	27 ± 7	48 ± 7	54 ± 11	420% ± 180%
19:01:56.390	-36:57:28.40	IRS 7e	<29	14 ± 3	<9	12 ± 3	306 ± 13	>3500%
			mos1 detector					
19:01:08.600	-36:57:21.30	S CrA	74 ± 7	33 ± 4	30 ± 4	12 ± 2	26 ± 5	500% ± 130%
19:01:41.550	-36:58:31.60	IRS 2	54 ± 4	33 ± 3	44 ± 4	43 ± 3	52 ± 4	60% ± 20%
19:01:48.020	-36:57:22.40	IRS 5	26 ± 3	42 ± 3	9 ± 2	24 ± 2	14 ± 2	360% ± 100%
19:01:50.450	-36:56:38.10	IRS 6	<6	<3	6 ± 2	<3	<6	>130%
19:01:50.660	-36:58:09.90	IRS 1	45 ± 4	37 ± 3	27 ± 3	21 ± 2	21 ± 3	120% ± 40%
19:01:53.670	-36:57:08.30	R CrA	<7	<4	7 ± 2	6 ± 2	11 ± 3	>180%
19:01:56.390	-36:57:28.40	IRS 7e	<6	<4	<4	<3	95 ± 5	>2790%
			mos2 detector					
19:01:08.600	-36:57:21.30	S CrA	68 ± 6	38 ± 4	35 ± 4	13 ± 2	39 ± 5	410% ± 100%
19:01:41.550	-36:58:31.60	IRS 2	50 ± 5	30 ± 3	42 ± 4	49 ± 3	52 ± 4	70% ± 20%
19:01:48.020	-36:57:22.40	IRS 5	34 ± 4	39 ± 3	8 ± 2	31 ± 3	10 ± 3	370% ± 120%
19:01:50.450	-36:56:38.10	IRS 6	<7	<3	9 ± 2	<3	<6	>260%
19:01:50.660	-36:58:09.90	IRS 1	55 ± 5	41 ± 3	27 ± 3	25 ± 2	22 ± 3	140% ± 40%
19:01:53.670	-36:57:08.30	R CrA	<8	<4	<5	6 ± 1	<7	>40%
19:01:56.390	-36:57:28.40	IRS 7e	<7	4 ± 1	<4	4 ± 1	90 ± 6	>2200%

Table 3.3: Source detections from each of the XMM-Newton cameras. Fluxes listed are in counts/ksec and bins had length of the entire epoch length. Detections with S/N < 3 were replaced with a 3 sigma upper limit. The final column gives the peak to peak variability and the error is calculated with Equation 2.3, just like the Herschel data. The variability is given as a lower limit to variability where the lowest flux was an upper limit.

While we took the photometry at the known location of each of these seven sources for each of the five epochs, in some cases the signal to noise was low enough that we consider it a non-detection. In this case, we give a conservative upper limit of 3 sigma (three times the error) and use this for our variability calculation later on as well. This is represented in the light curves in this section by an arrow that begins at 3 sigma and points down to zero, so the top represents the upper limit, but the bottom shows the value could be anywhere in that range. We chose S/N < 3 as our criteria for a non-detection because this is a conservative limit that still allows us to see when sources have a flare.

3.3.1   The Class 0 protostar IRS 7e

IRS 7e was the most variable source during our observation. It had a flare in the final epoch with flux 10-36 times greater than previous epochs. In Figure 3.3 we see the light curves with binning of the entire epoch, taken with all three cameras. For all three cameras, the detections in the first and third epoch had a S/N < 3 so we consider them possible non-detections. For these, we include an upper limit of 3 sigma in our flux table, and this is shown in the light curves as an upper limit arrow. For just the MOS1 camera, the flux measurements for epoch 2 and epoch 4 also had S/N < 3. This difference from the other cameras was interesting as, especially the two MOS detectors, should not be vastly different. We compared the two camera's S/N for these detections and found they were within 2 sigma. So the variations between detectors here are not significant.

The variability was calculated as a lower limit since all three light curves had epochs where the flux had a S/N < 3 and was thus converted to an upper limit. Due to the flare in the final epoch, these variabilities were very high, with a flare of at least 36 times the flux of the previous epochs as measured by the pn detector. The MOS1 and MOS2 cameras also recorded this large flare but with fluxes 29 and 23 times greater than the previous epochs respectively.

The fact that the signal to noise was no higher than 4 in epochs 1-4 for all detectors also shows how vast the flare in the fifth epoch was since for the flare the S/N was greater than 16 for all detectors. This made it our most significant flare.

Since all detections with S/N < 3 are considered non-detections, for the time-resolved light curves with binning 1200s we only have reliable light curves for the fifth epoch as every bin in epoch 1-4 except for one bin was a non-detection. These can be seen in Figure 3.4. The flare in the fifth epoch was detected by all three cameras with very high S/N. During the flare we see there was no variability on timescales of minutes to hours because the signal to noise of the variability was less than 3.

Figure 3.3: XMM X-ray light curves of IRS 7e. Flux rate detected by pn, MOS1, and MOS2 cameras for entire epoch observation length. Arrows represent 3 sigma upper limits where the S/N of the measured flux was less than 3 and thus considered a non-detection.
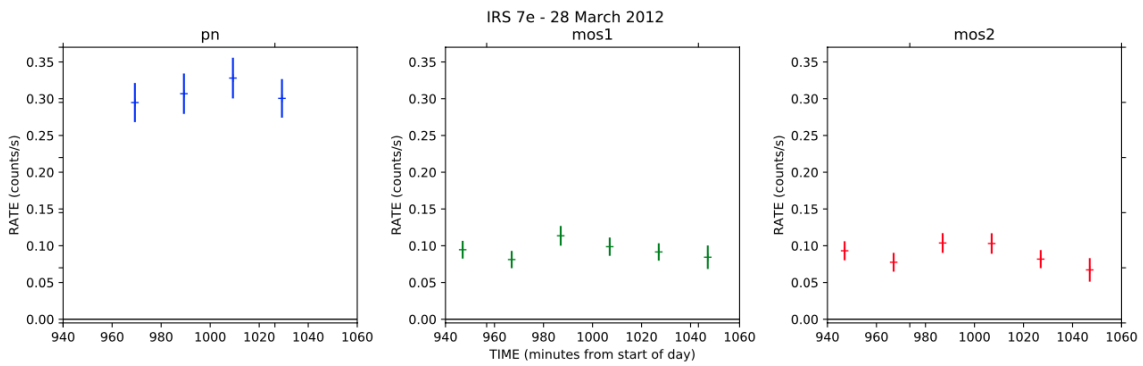
Figure 3.4: Time-resolved X-ray light curves of IRS 7e from each of the three XMM cameras during the fifth epoch on 28 March 2012. Time binning of 1200 seconds (20 minutes).

3.3.2 The Class I protostars IRS 2, IRS 5, and IRS 1

The Class I protostar IRS 2 was the source that exhibited the least variability during our observation. Of the flux detected by the pn camera, binned to the entire epoch length, the maximum variability observed was $70\% \pm 20\%$. This is still considered variable as the errors were low with signal-to-noise > 4, as seen in the light curve in Figure 3.5. The variability also followed the same pattern for the MOS1 and MOS2 cameras, which showed peak to peak variability of $60\% \pm 20\%$ and $70\% \pm 20\%$ respectively.

The light curves taken with binning 1200 seconds from all three cameras can be seen in Figure 3.6 below. On these timescales of minutes and hours within the epochs, we saw no significant variability with errors being too large in comparison to the possible variations and no consistency between cameras.

Figure 3.5: XMM X-ray light curves of IRS 2. Flux rate detected by pn, MOS1, and MOS2 cameras for entire epoch observation length.

Figure 3.6: Time-resolved X-ray light curves of IRS 2 from each of the three XMM cameras. Time binning of 1200 seconds (20 minutes). Arrows represent 3 sigma upper limits where the S/N of the measured flux was less than 3 and thus considered a non-detection.

IRS 5 was our most variable Class I protostar, with the second epoch having almost 5 times more flux than the third (variability $390\% \pm 90\%$), as detected by the pn camera and seen in Figure 3.7 below. The MOS1 and MOS2 cameras had similar variability at $360\% \pm 100\%$ and $370\% \pm 120\%$ respectively.

On smaller timescales, within the epochs, we see some possible variability, but all with S/N < 3, which is the conservative upper limit we took for the epoch long time binned

Figure 3.7: XMM X-ray light curves of IRS 5. Flux rate detected by pn, MOS1, and MOS2 cameras for entire epoch observation length.

photometry. Due to slight variability not being consistent across detectors we do not consider IRS 5 variable on these small time scales during our observations.
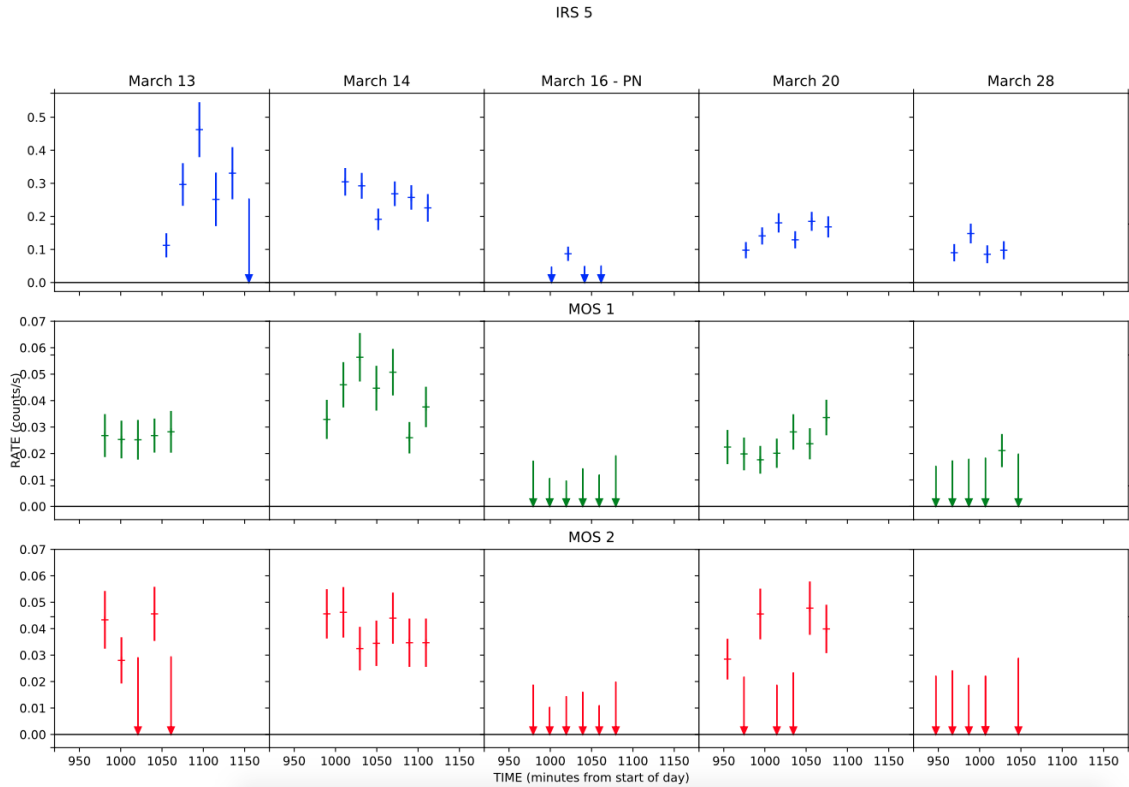
Figure 3.8: Time-resolved X-ray light curves of IRS 5 from each of the three XMM cameras. Time binning of 1200 seconds (20 minutes). Arrows represent 3 sigma upper limits where the S/N of the measured flux was less than 3 and thus considered a non-detection.

IRS 1 has the most interesting variability because it starts with high flux in the first epoch and then gradually declines, indicating a flare either before our observation began or right at the start of the observation. The peak to peak variability for fluxes taken with the pn camera is $180\% \pm 40\%$. For the MOS1 camera it's $120\% \pm 40\%$ and for MOS2 camera

it's 140% ± 40%. The full epoch binned light curves for all three cameras' detections are seen in Figure 3.9 where the nice steady decline is easily seen and all three cameras have the same shape and seem to settle on a baseline count rate by the fourth epoch. As discussed in Section 3.1.4, the MOS cameras only receive about 44% of the incoming flux while the pn camera is unobstructed, and in the case of IRS 1, the flux measured in the final epochs even matched that, as the MOS cameras fluxes are ∼44% of the pn cameras flux.

The light curves of all three cameras at binning 1200 seconds are in Figure 3.10. Similar to IRS 5, there is some variability on these timescales, but due to the low signal to noise and because the variability is not consistent between the pn and MOS detectors, we cannot be sure of whether it is actual variability or noise.
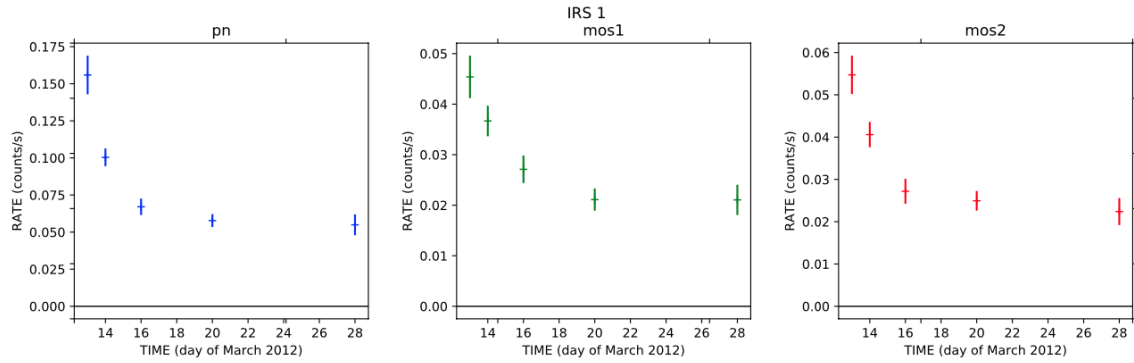
Figure 3.9: XMM X-ray light curves of IRS 1. Flux rate detected by pn, MOS1, and MOS2 cameras for entire epoch observation length.
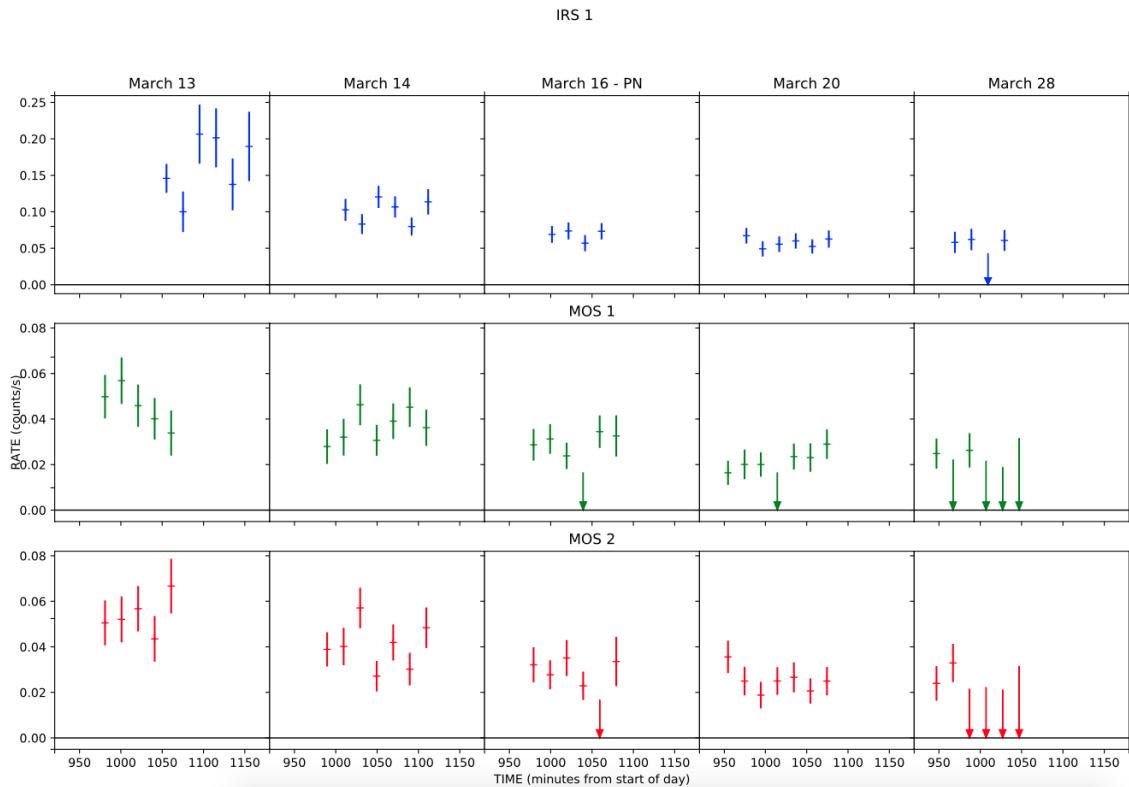
Figure 3.10:   Time-resolved X-ray light curves of IRS 1 from each of the three XMM cameras.   Time binning of 1200 seconds (20 minutes).   Arrows represent 3 sigma upper limits where the S/N of the measured flux was less than 3 and thus considered a non-detection.

3.3.3   The T Tauri stars S CrA and IRS 6

S CrA has an interesting light curve since it seems to start with high flux levels, decline over the next three epochs, and then begin to rise again in the final epoch, indicating possible flaring on timescales of a couple weeks. The peak to peak variability detected with the pn camera was $380\% \pm 60\%$. The MOS cameras follow the same flux pattern with MOS1 having variability $500\% \pm 130\%$ and MOS2 having variability $410\% \pm 100\%$.

The light curves binned at 1200s for each of the detectors are plotted in Figure 3.12. While it appears there may be some variability on these timescales, the errors are too high and no variability has a S/N > 3. There was also no consistency between detectors. Thus we found no reliable variability on timescales of minutes to hours from S CrA.
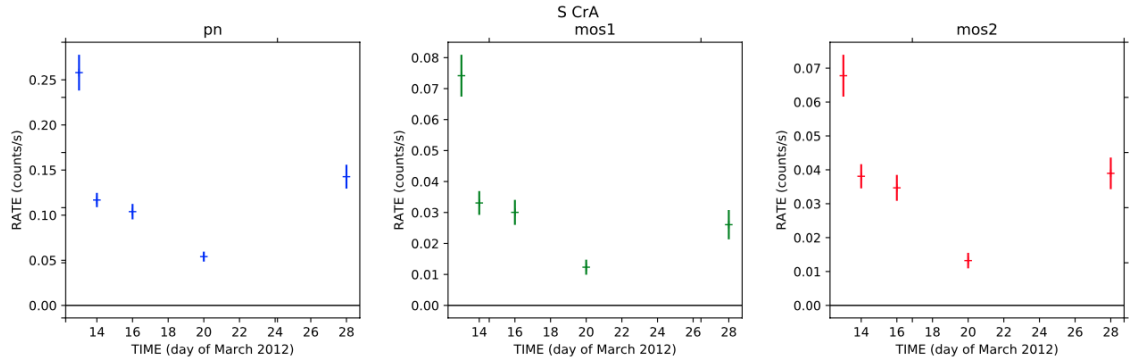
Figure 3.11: XMM X-ray light curves of S CrA. Flux rate detected by pn, MOS1, and MOS2 cameras for entire epoch observation length.
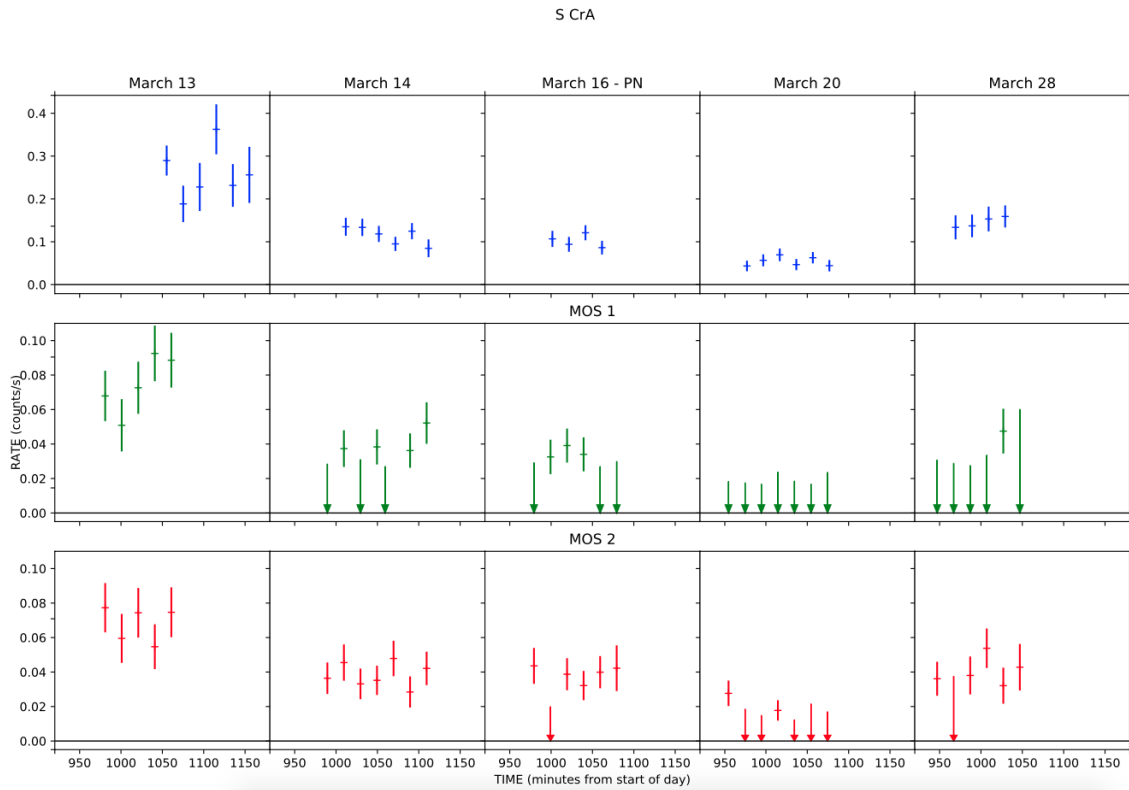
Figure 3.12: Time-resolved X-ray light curves of S CrA from each of the three XMM cameras. Time binning of 1200 seconds (20 minutes). Arrows represent 3 sigma upper limits where the S/N of the measured flux was less than 3 and thus considered a non-detection.

IRS 6 has a signal to noise of less than 3 in epochs 1, 2, 4 and 5 for all cameras, so we consider those non-detections and instead of a count rate, we have given a conservative upper limit of 3 sigma. We visually inspected these images and there is no obvious source at the location of IRS 6, only noise, for those four epochs across all three cameras, which helps verify there are no significant detections during those epochs. We observed what

could then be considered a small flare in the third epoch consistent across all three cameras. For the 20 minute time-resolved light curves, out of the 88 flux bins across all three cameras only five bins had S/N > 3 thus there is no variability we can reliably comment on at these timescales.
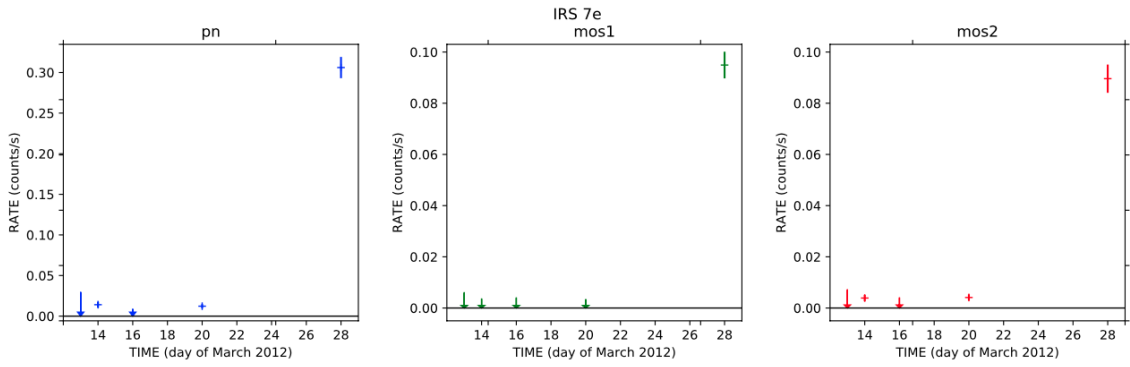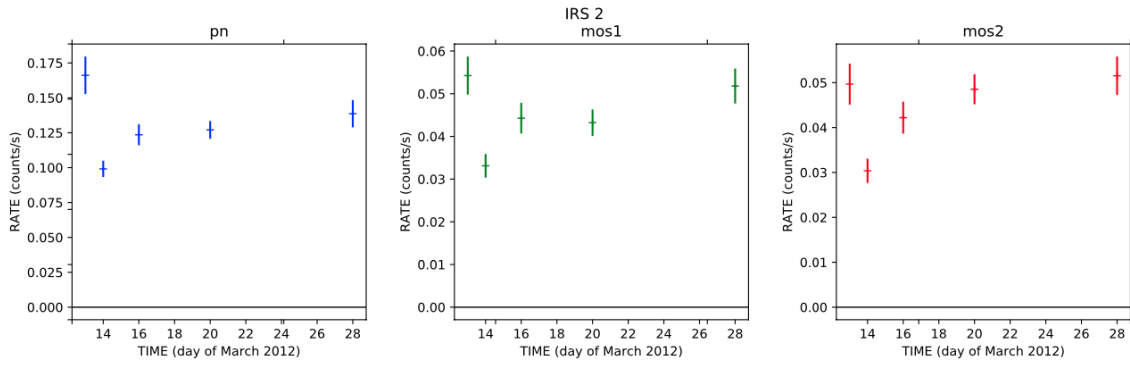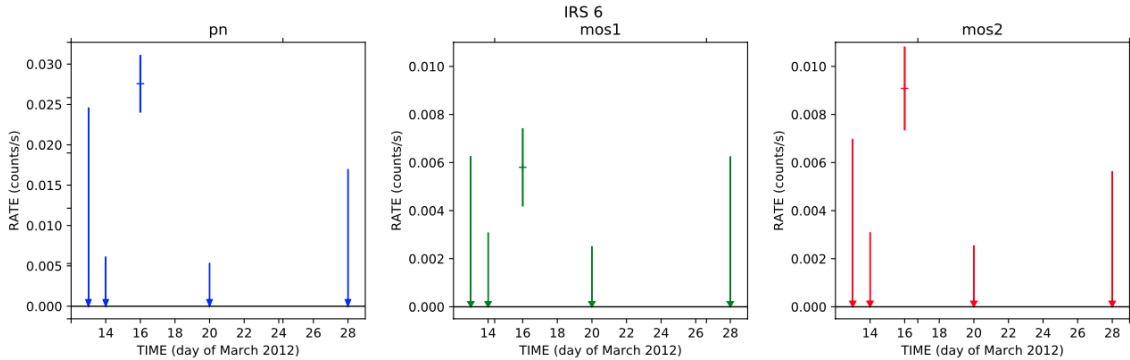

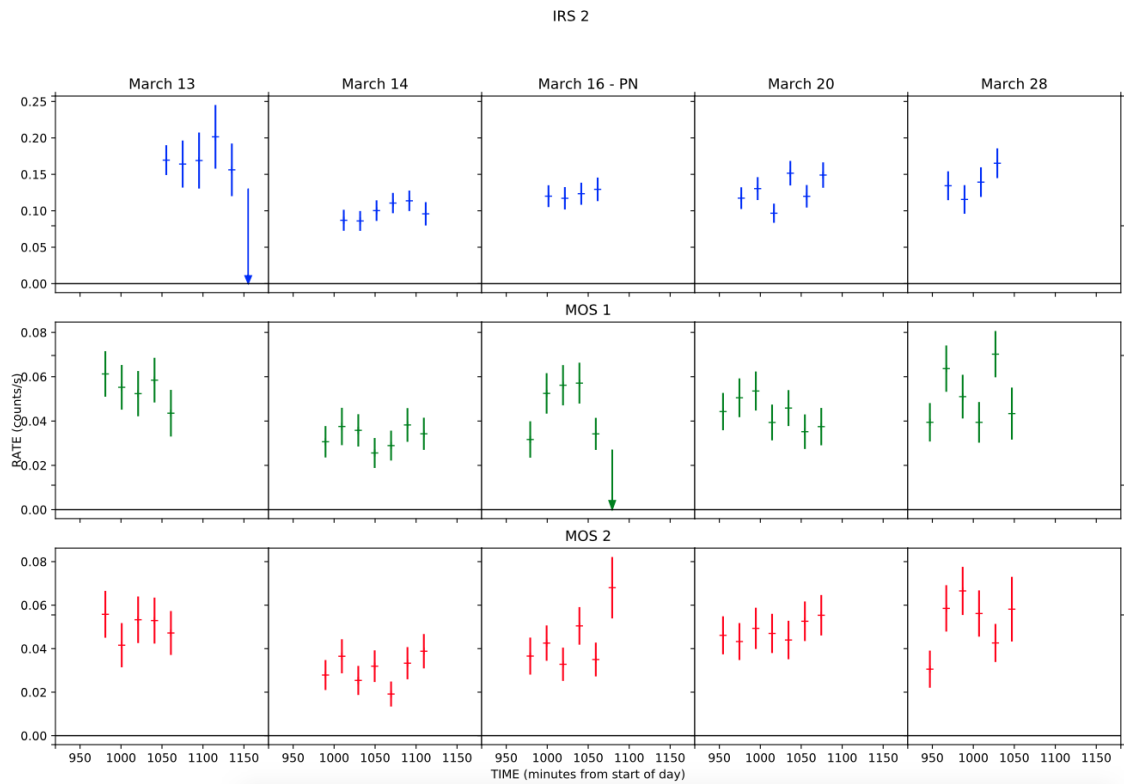Figure 3.13: XMM X-ray light curves of IRS 6. Flux rate detected by pn, MOS1, and MOS2 cameras for entire epoch observation length. Arrows represent 3 sigma upper limits where the S/N of the measured flux was less than 3 and thus considered a non-detection.

3.3.4   The Herbig Ae star R CrA

R CrA overall had the least reliable photometry, which is unsurprising given its proximity to IRS 7, causing possible contamination. However, we did extract a reliable light curve using the pn camera photometry with full epoch binning. For the MOS1 camera, the first two epochs had detections with S/N < 3. And the MOS2 detections from four of the five epochs had S/N < 3. As we previously did with other sources, detections with S/N< 3 were considered non-detections and converted to a 3 sigma upper limit in these light curves seen in Figure 3.14 below.

In the full epoch binned light curve from the pn camera, R CrA appears to have a flare in the first epoch, with peak to peak variability of 420% ± 180%. Unfortunately we only see this with the pn camera, as the MOS cameras both have a non-detection in the first epoch. This could be due to the pn/MOS time offset, which we discuss more in Section 4.1. The MOS1 camera also did not detect R CrA in the second epoch. Thus the peak to peak variability of >180% is given as a lower limit since the lowest flux is the upper limit in epoch 2. The MOS2 camera only detected R CrA in the fourth epoch and so the upper limit to variability is >40%. So overall, R CrA did exhibit some variability but due to the high errors and lack of agreement between the detectors, we cannot be sure of how variable it was.

We generated and analyzed the light curves with binning of 1200s for R CrA as we did with the other sources. However, similarly to IRS 6, of the 88 total flux bins across all three cameras, only five had a S/N > 3. Therefore there is no variability we can reliably comment on for these timescales.
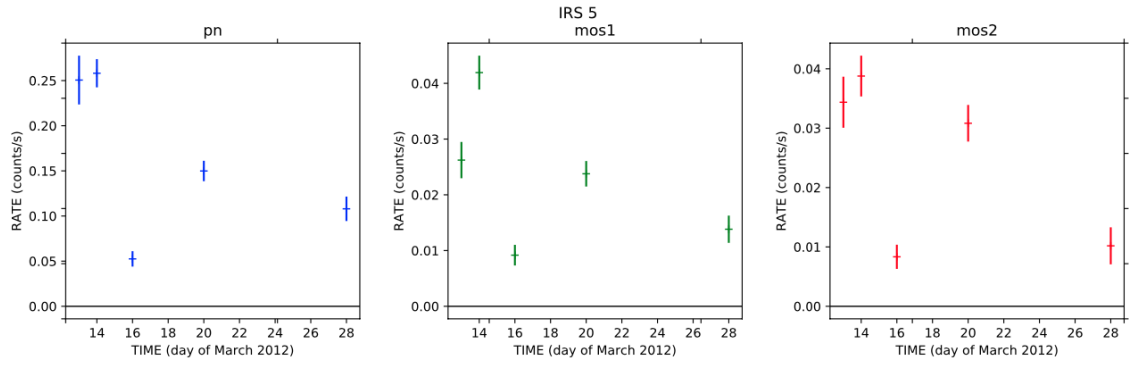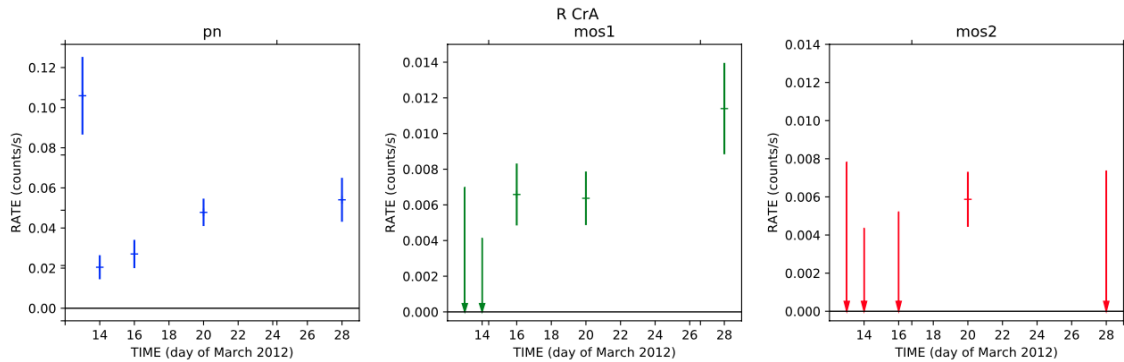

Figure 3.14: XMM X-ray light curves of R CrA. Flux rate detected by pn, MOS1, and MOS2 cameras for entire epoch observation length. Arrows represent 3 sigma upper limits where the S/N of the measured flux was less than 3 and thus considered a non-detection.

3.4   4XMM Catalogue sources

The 4XMM Serendipitous Source Catalogue (Webb et al., 2020) is produced by The XMM-Newton Survey Science Centre and includes all source detections from all observations made by XMM-Newton in its 20 years. To learn more about how the data is processed and how the catalogue is produced, see Webb et al. (2020). Since our XMM images cover a larger field of view than just the Coronet Cluster, we decided to use the 4XMM Serendipitous Source Catalogue to identify all the sources in the field of view of our observations. We did so to look at the general variability between epochs of other YSOs in the vicinity of the Coronet and possibly identify any new sources in this deep XMM observation.

The catalogue allows us to set parameters on the region and dates that we want source detections from and then download as a spreadsheet with a large variety of information, including count rates, total counts, error, and exposure time to name a few. Since the 4XMM Catalogue detections are found using a standardized process, not all possible detections are sources, thus each detection is assigned a "detection likelihood" that is calculated using many factors and is also detailed in Webb et al. (2020). We use this metric as a part of our assessment on whether a detection is a source or just noise.

We started by downloading all possible source detections from our observations and after a visual assessment as well as a thorough comparison with past literature to find previously identified sources and rule out what appears to be noise, we came up with the following criteria for sources: (1) Each source must have at least one epoch observation with detection likelihood greater than 15. (2) Remove extended sources since we are only interested in point sources. (3) Remove sources on chip gaps. The first criteria was chosen because many possible sources were only detected in one epoch with detection likelihoods (DL) below 15 and, on our images, these were indistinguishable from the background noise. So any "sources" detected only once with such a low likelihood did not seem to be actual sources. All sources detected only once with DL greater than 15 however were very obviously sources on the map and were found in previous literature. But we did allow for detections with lower DL for sources that had a detection in another epoch with DL > 15 since it was already a verified source, so allowing that detection to be part of our data set gave us more variability information.

Some detections were combined with other sources if they were very close (within the positional error) and the source had no significant detection in the same epoch as the new combined detection. These were: (1) ISO-CrA 134 and J190126.1-365918 in epoch 20 and (2) HD 176386-B and J190139.1-365330 in epochs 16, 20, and 28.

Two detections were removed due to being on the chip gap after we visually inspected the images and saw no evidence of a source. Both also had no detections in other previous observations (4XMM J190135.4-365803 and 4XMM J190138.5-370230).

After implementing this criteria, a total of 47 sources were detected. These are listed in Table 3.4. Of these, 19 were detected in all five epochs. We found 38 YSOs: one Class 0 protostar, six Class I protostars, thirteen Class II protostars, seventeen Class III protostars, and one Herbig Ae/Be star (all classifications found in Peterson et al., 2011; Forbrich & Preibisch, 2007; Sicilia-Aguilar et al., 2008). We also found one quasar in our field of view, and eight previously unclassified sources. Of these eight, two were listed in Forbrich & Preibisch, 2007 (J190137.0-365601 and J190221.2-365012). That leaves the following six sources that we detected but have not previously been identified as cluster members in X-ray: 4XMM J190031.5-365212, 4XMM J190047.2-364747, 4XMM J190104.5-370326, 4XMM J190128.2-365927, 4XMM J190243.4-370225, and 4XMM J190248.6-365225. We discuss these in greater detail in Chapter 5.

We calculated the variability and variability error in the same way we did with our

own photometry. Detections with count rates having S/N < 3 were replaced with an upper limit of 3 sigma which then gave us a lower limit of variability, as seen in Table 3.4 (only one detection provided no meaningful constraints and was removed as an obvious non-detection due to having S/N ~ 0.002). We detected a total of 21 sources that had a peak to peak variability with S/N > 3 and classified these as variable, which is the same process we used for our own photometry. We then also have six sources that were detected in only one epoch and we consider these variable as they appear to be flaring for one epoch while their flux fades into the background for the other epochs. For these we calculated a lower limit on the variability by using the faintest detected source flux in the data as the minimum flux.

Of the 47 detected sources, 27 showed some level of variability (seven of these are the seven sources we have already introduced as our core sample and we will next discuss their variability using the photometry we took in the next section). Of the total 27 variable sources, eleven are Class III protostars, eight are Class II protostars, five are Class I protostars, one is a Class 0 protostar, and two have not been previously classified. The most variable source found in the Catalogue was IRS 7e. The most variable source that is not part of our core sample is the Class III protostar VSS VIII-27.

On average by class, the most variable were the Class 0, which, per Table 3.5, had an average variability that was more than 3 sigma greater than the other three class's average variabilities. While the Class II and III protostars are marginally more variable than the Class I protostars, all three have overlapping 3 sigma intervals, thus are not significantly different, especially due to the small sample size. These sample sizes, averages, and propagated errors can be seen in Table 3.5. Due to the relatively small sample sizes, especially for Class 0 with only one in our sample, we cannot say if these classes are, on average, always more variable, but only that this was the case during our observations.

Name	Epochs detected in (out of 5)	SED Class	Count Rate Variability
IRS 7e	**3**	**0/I**	**1777% ± 200%**
IRS 7w	**1**	**I**	**>1230%**
IRS 5	**5**	**I**	**357% ± 84%**
IRS 9	**1**	**I**	**>157%**
IRS 1	**5**	**I**	**142% ± 22%**
G-36	3	I	70% ± 44%
IRS 2	**5**	**I**	**49% ± 10%**
CrA-18	**2**	**II**	**509% ± 83%**
IRS 6	**4**	**II**	**453% ± 105%**

TY CrA	**5**	**II**	**435% ± 10%**
ISO-CrA 127; CrA-13	**1**	**II**	**>292%**
S CrA	**5**	**II**	**289% ± 33%**
ISO-CrA 134; CrA-40	**5**	**II**	**196% ± 29%**
HBC 680; CrA-30	**5**	II	**>128%**
IRS 13; CrA-16	4	II	123% ± 73%
HBC 677	5	II	120% ± 44%
ISO-CrA 146; CrA-56	4	II	93% ± 71%
ISO-CrA 159; CrA-31	5	II	90% ± 68%
HD 176386-B; CrA-54	**5**	**II**	**81% ± 15%**
CrAPMS 8; GP g2; CrA-6	4	II	>76%
R CrA	4	Herbig Ae	91% ± 43%
VSS VIII-27; CrA-66	**5**	**III**	**1416% ± 111%**
ISO-CrA 141	**3**	**III**	**762% ± 155%**
ISO-CrA 93; CrA-7	**1**	**III**	**>460%**
ISO-CrA 136; CrA-69	**5**	**III**	**425% ± 74%**
ISO-CrA 137; CrA-14	**5**	**III**	**354% ± 52%**
CrA-71	**3**	**III**	**330% ± 111%**
VSS VIII-26; CrA-72	5	III	139% ± 49%
CrA-4111	3	III	78% ± 48%
V702 CrA; CrAPMS 2; CrA-74	**5**	**III**	**67% ± 5%**
R14; CrAPMS 9; CrA-65	4	III	63% ± 27%
HBC 679; VSSt 24; CrA-75	**5**	**III**	**60% ± 10%**
Hα 13; CrA-73	**5**	**III**	**59% ± 18%**
HD 176270; CrAPMS 10	**5**	**III**	**56% ± 13%**
ISO-CrA 133; CrA-67	3	III	52% ± 47%
ISO-CrA 135; CrA-68	2	III	51% ± 24%
V709 CrA; CrAPMS 1; CrA-70	**5**	**III**	**43% ± 3%**
CrA-468; LS-RCrA 2	3	III	39% ± 38%
J190248.6-365225	**1**	–	**>395%**
J190243.4-370225	**1**	–	**>137%**
J190137.0-365601	3	–	88% ± 56%
J190047.2-364747	3	–	>82%
J190031.5-365212	2	–	35% ± 35%
J190104.5-370326	2	–	18% ± 40%
J190221.2-365012	2	–	13% ± 43%
J190128.2-365927	2	–	3% ± 3%
G-115 (quasar)	4	quasar	76% ± 44%

Table 3.4: List of sources detected in our field of view consistent with the criteria outlined in Section 3.4. Variability percentage is listed if the source was detected in more than one epoch and sources detected in only one epoch have a lower limit to their variability which we calculated using the lowest source flux from this data as a minimum. Sources with at least one upper limit detection also have a lower limit of variability listed. Variable sources (criteria is the same as our photometry and discussed in Section 3.1) are in bold. Sources are listed in order by spectral class and then by most variable. Names and SED class from Peterson et al. (2011); Forbrich & Preibisch (2007); Sicilia-Aguilar et al. (2008).

In summary, the XMM observations had durations ranging from 5-8.6 ks ($\sim$ 84-143

SED Class	Number of sources (not from core sample)	Percent that are variable	Average variability
Class 0	1 (0)	100%	$1780\% \pm 200\%$
Class I	6 (3)	83%	$150\% \pm 20\%$
Class II	13 (11)	62%	$240\% \pm 20\%$
Class III	17 (17)	65%	$250\% \pm 20\%$

Table 3.5: Percentage of (classified) sources of each class that we consider variable, which was the same criteria we used previously in this section, that being the peak to peak variability having $S/N > 3$. We also consider sources only observed in one epoch to be variable, since they had an increase in flux during that epoch making them detectable. In parentheses under total sources, we list how many were not from our core sample discussed previously.

minutes) per epoch. All three EPIC cameras observed the Coronet Cluster simultaneously, except for on 13 March 2012, where the pn and MOS cameras only overlapped by 30 minutes. We generally used the photometry from the pn camera for our analysis as it received an unobstructed beam of flux from the X-ray telescope, whereas the MOS cameras only receive 44% of the incident flux. We detected seven of the eleven Herschel sources, all of which were previously known X-ray emitters. We used SAS to create calibrated event lists and to extract light curves from the images for each of these sources. We extracted two sets of light curves per source and per camera, one with time resolution encompassing the entire length of each epoch, and one with time bins of 1200s, to search for even shorter term variability within epochs. On average, the brightest source was IRS 5, however the brightest single epoch detection came from IRS 7e, which flared in the final epoch. IRS 7e was also the most variable source with the final epoch having a count rate up to 36 times higher than previous epochs. All sources exhibited some variability and on average the Class 0 and II sources were the most variable. We last used the 4XMM Source Catalogue to find all the sources in our observation's field of view. We detected 47 sources, of which 27 were variable. The most variable class on average in our observation was Class 0.

Chapter 4

Comparison

In this section, we first discuss the observations from our two observatories, discussing the impact of any differences. Then we compare the sources and source photometry extracted in the two bands. And last we compare light curves and variability of the sources in the far-infrared and X-ray.

4.1 Observation comparison

The Herschel and XMM observations were taken on concurrent days, but the exact observation times didn't always overlap. Below is a table with the start and end times of each observation from each camera, as well as the duration of the observations, and a graph highlighting the differences.

	HERSCHEL FAR-INFRARED						XMM-NEWTON X-RAY								
	scan			cross scan			pn			MOS1			MOS2		
Date	Start Time	End Time	Duration	Start Time	End Time	Duration	Start Time	End Time	Duration	Start Time	End Time	Duration	Start Time	End Time	Duration
2012-03-13	15:59:07	16:41:19	2532	16:42:22	17:24:34	2532	17:35:14	19:26:39	6685	16:20:53	18:06:08	6315	16:20:53	18:06:23	6330
2012-03-14	15:59:04	16:41:16	2532	16:42:19	17:24:31	2532	16:51:46	18:45:46	6840	16:29:30	18:49:51	8421	16:29:30	18:49:56	8426
2012-03-16	16:04:15	16:46:27	2532	16:47:30	17:29:42	2532	16:41:33	18:05:34	5041	16:19:17	18:09:39	6622	16:19:17	18:09:44	6627
2012-03-20	15:37:03	16:19:15	2532	16:20:18	17:02:30	2532	16:16:46	18:14:07	7041	15:54:30	18:18:12	8622	15:54:30	18:18:18	8628
2012-03-28	15:31:42	16:13:54	2532	16:14:57	16:57:09	2532	16:09:17	17:33:18	5041	15:47:01	17:37:24	6623	15:47:01	17:37:29	6628

Table 4.1: Start time, end time, and duration of each observation for each of the XMM cameras and the Herschel camera on each of the five observation days.

As we discussed in previous sections, while comparing wavelengths we are not able to compare on timescales of seconds to hours as no significant time-resolved data was available with Herschel and was often unreliable with XMM. In our conclusions we will only discuss variability on timescales of days and weeks, thus these small differences in observation times do not affect our results or conclusions.

Lastly, we do not compare our data to other Herschel or XMM observations of the
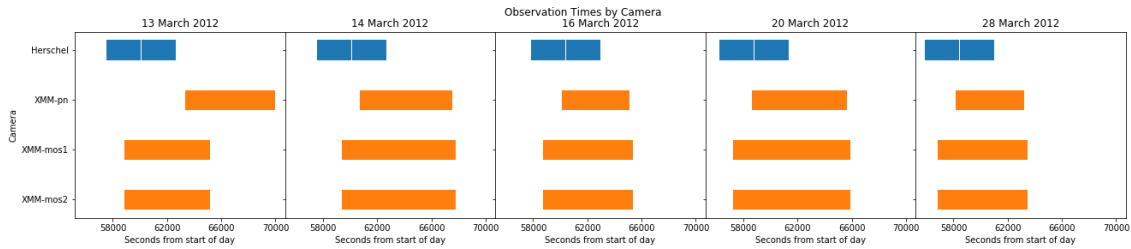
Figure 4.1: Figure 34 Figure of the beginning to end time of each camera's observation. In blue are the Herschel observation times. There are two bars because there was a scan and then a cross scan that started 63 seconds later. Each of the Herschel observations lasted 2532 seconds. The three XMM cameras (in orange) took different images of varying lengths, but the two MOS cameras always started at the same time and ended 5 to 15 seconds apart. The only observations not to overlap within epochs are the Hershel and XMM-pn camera on the first day, where the pn observation began about ten minutes after the Herschel one ended.

Coronet because our main objective is to look for short timescale variability correlations thus we need the X-ray and far-IR observations to be in the same time domain and no other Herschel observations have simultaneous XMM observations of the Coronet. Later in Chapter 5 we do compare our Herschel photometry to Sicilia-Aguilar et al. (2013) which helps verify that our measured source fluxes are reasonable. But since the overall goal of the project is the simultaneous variability comparison, other observations would not be helpful for those purposes.

4.2   Comparing source populations

We identified eleven Coronet sources with Herschel. Of these, we found seven visible/ resolvable with XMM. We discuss the differences in source population next.

IRS 5a/b and 5N, which were resolvable in far-infrared, were not resolvable in X-ray, so we refer to them as the combined object IRS 5 in our X-ray photometry.

We also were unable to resolve IRS 7w in our X-ray dataset. IRS 7w may have flared in epoch 3 but was not resolvable in any other epochs. And due to its proximity to IRS 7e and R CrA, photometry extraction would have been more complex than our methods we used for all other sources and thus outside the scope of this project so we leave it in our future work section, Chapter 7.

Lastly we did not detect the far-infrared sources SMM2 or T CrA in X-ray. Forbrich & Preibisch (2007) also did not detect SMM2 in their deep Chandra data and they only detected T CrA as a very faint source (14 counts) and noted that in the first Chandra X-ray

observation of the Coronet (Skinner et al., 2004) T CrA was also only faintly detected with 4 ± 2 counts. Forbrich & Preibisch (2007) determine that T CrA is the weakest emitter of the T Tauri stars in the region, suggesting it is the hottest object in the Coronet Cluster.

Thus our XMM data did not resolve IRS 5a/b or IRS 7e/w and did not detect SMM2 or T CrA. However, there are no sources from our core sample in the Coronet region that were detected by XMM-Newton but not by Herschel.

4.3 Variability comparison

We performed a correlation test, calculating the Pearson Correlation Coefficient, which is a statistical measure of the degree of linear correlation between two variables (meaning here the XMM fluxes and the Herschel fluxes) on each of our sources. With this test, we also calculated the p-value which gives how statistically significant the correlation is (this is the null hypothesis probability where the null hypothesis is that there is no correlation). Generally a null hypothesis probability of $< 5\%$ would indicate a statistically significant result. However due to the small sample size of only five epochs, none of our sources had very low null hypothesis probabilities, but several of them are below 20%, and thus we discuss those.

IRS 1 is interesting because the X-ray flux is highest in the first epoch and then only declines, indicating a possible X-ray flare either at the beginning of our observation time or shortly before it started (see Section 1.2.4 for flare timescales). The far-infrared light curve has a peak in the second epoch and similarly steadily declines. This could possibly indicate an X-ray event followed by a heating response in the far-infrared. Thus for IRS 1 we calculated the Pearson Correlation Coefficient with a one and two epoch offset, meaning matching the first four X-ray epochs with the last four far-IR epochs, as well as the first three X-ray and last three far-IR. This was to attempt to line up the peak in each flare as the light travel time would be seen as a few days offset. For the one epoch offset, the Correlation Coefficient was 0.84, which is considered a strong positive correlation, and the null hypothesis was 16%. With a two epoch offset, we got a correlation of 0.99 and probability 8%. We did calculate the coefficient with no offset and it was only 0.36 with a probability of 55%

We cannot be completely sure of the time delay between the X-ray flare and far-infrared response due to only having five data points and not knowing what happened between our

data points, but taking into account the average decay timescale of an X-ray flare (1-1.5 days as discussed in Section 1.2.4) and knowing the far-IR peaked sometime between the first and third epoch, it appears the time delay was 1-4 days, which is the time lag that we would expect due to light travel time, as discussed in Section 1.2.3.

Figure 4.2: On the left is the light curve of IRS 1 using the flux detected by the XMM-Newton pn camera with time bins of the entire epoch observation time. On the right is the light curve of IRS 1 of the flux detected by the Herschel PACS photometer in the green channel and combining the scan and cross scan images (level 2.5 processing, hpf map).

To further the analysis of this possible flare with a heating response, we would have liked to calculate the size of the flare and whether it is possible for this size X-ray flare to cause this amount of disk heating. Alexander et al. (2004) model how X-ray flares may affect the disk and we could use this to discuss how this could heat up the circumstellar material and possibly calculate if this size of flare could have caused this amount of disk heating. This was not within the scope of this project though and is included in future work (Section 7).

It is unfortunate that our observation didn't go a bit later since there was a very large X-ray flare seen from the Class 0 protostar IRS 7e in the last epoch, increasing by 25 times. But we do not know if there would have been a far-infrared delayed response, nor if the X-ray flare had just begun or was already ending, due to the closest data point being eight days prior. What this does tell us is there was no instantaneous far-infrared response, since the Herschel data we do have of IRS 7e is very constant within the errors, similarly to the X-ray data from epoch 1-4 before the flare. The Pearson Correlation Coefficient for IRS 7e, with no offset, was 0.8 with 11% null hypothesis probability, but again this is not low enough to definitively be significant.

Figure 4.3: On the left is the light curve of IRS 7e using the flux detected by the XMM-Newton pn camera with time bins of the entire epoch observation time. On the right is the light curve of IRS 7e of the flux detected by the Herschel PACS photometer in the green channel and combining the scan and cross scan images (level 2.5 processing, hpf map).

IRS 2 is very interesting too since it seems there could have been an X-ray flare at the beginning of the observation or before it and then another smaller flare over the last three epochs, increasing by 40% ± 10%. Then in response the Herschel data is also coming down from a flare in the first four epochs and then increases in the final epoch by 10% ± 1%. This could possibly be another instance or two of an X-ray flare with a far-infrared heating response and with time delays of about a week. But due to the small number of epochs measured, we cannot be sure (and the Pearson Correlation Coefficient was very low and insignificant in this case). We do include in our future work section a calculation of the later X-ray flare size to see if it could cause the final epoch flare in the far-infrared.

Figure 4.4: On the left is the light curve of IRS 2 using the flux detected by the XMM-Newton pn camera with time bins of the entire epoch observation time. On the right is the light curve of IRS 2 of the flux detected by the Herschel PACS photometer in the green channel and combining the scan and cross scan images (level 2.5 processing, hpf map).

S CrA is also interesting as the timescales of the variability seem to differ between the
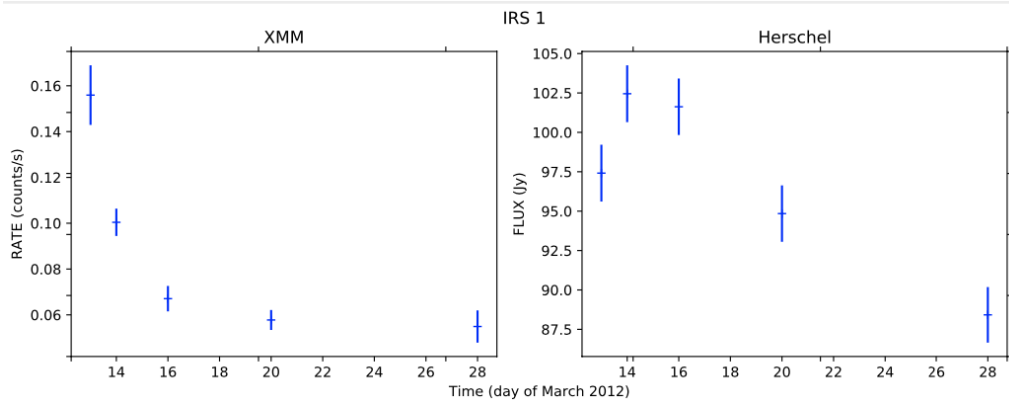
Figure 4.5: On the left is the light curve of S CrA using the flux detected by the XMM-Newton pn camera with time bins of the entire epoch observation time. On the right is the light curve of S CrA of the flux detected by the Herschel PACS photometer in the green channel and combining the scan and cross scan images (level 2.5 processing, hpf map).

far-infrared and X-ray detections. The X-ray light curve seems to flare, then decrease in the first three epochs, then increase again in the fifth epoch, indicating possible flaring on timescales of a couple weeks. However the far-infrared light curve shows the flux decreasing then increasing then decreasing again between each epoch. This indicates variability on timescales of a couple days. As we do not know what was going on between epochs we cannot be sure that the X-ray light curve did not also have daily variability between epochs, but as we did not find variability within the epochs on timescales of hours, this seems unlikely. But we still cannot rule out that there was variability on daily timescales coming from the star and that the far-infrared emission came from the tail of the SED. The far-infrared detections are probing the circumstellar disk and we know there are no processes happening on timescales of days, so it is interesting what could be causing this. S CrA is especially interesting since it is quite far removed from the other sources so there is likely no interference from the central structured background emission or other bright sources. There was no significant correlation calculated here, with or without offset.

R CrA seems to have an X-ray flare in the first epoch with flux four times higher than the next epoch, only one day later. But since it is the first epoch, the flare could have peaked earlier. It's unfortunate the errors in the Herschel data are so great (but not unexpected due to the complicated emission R CrA sits in) but due to this we cannot say if there was a far-infrared response. There was no significant correlation between the light curves when we ran our correlation test.
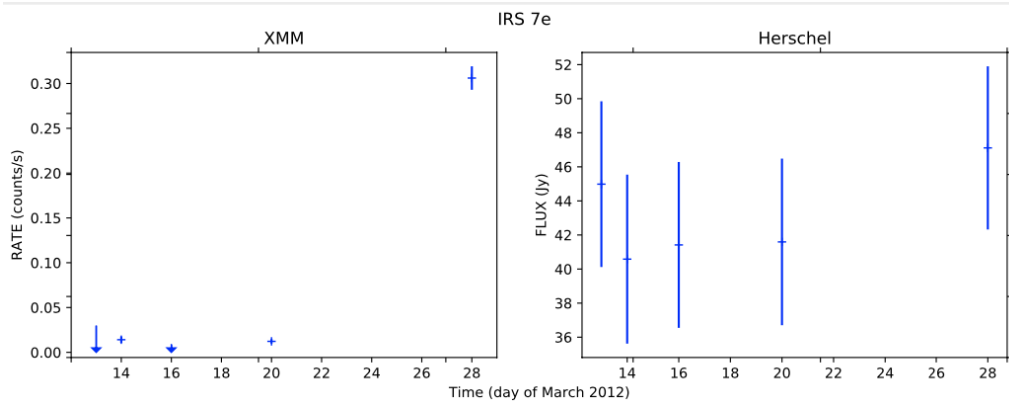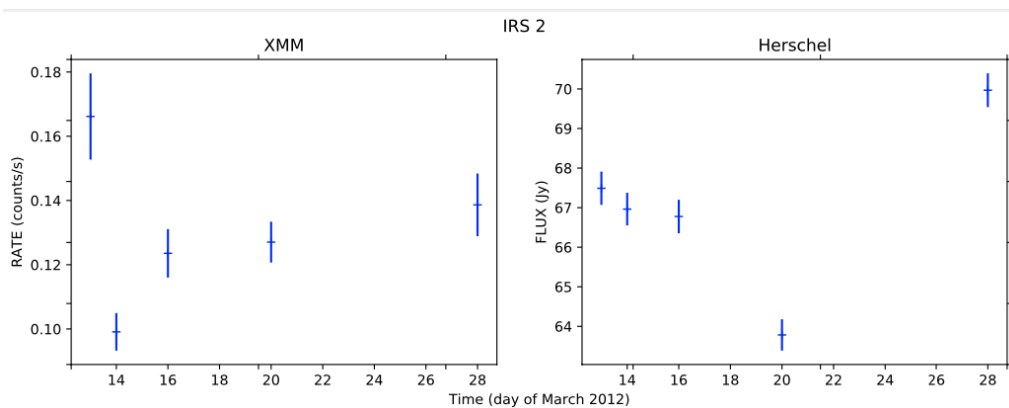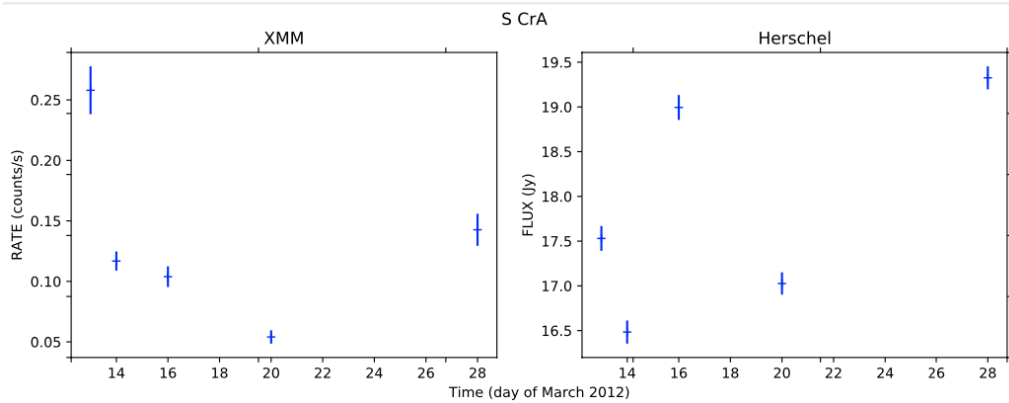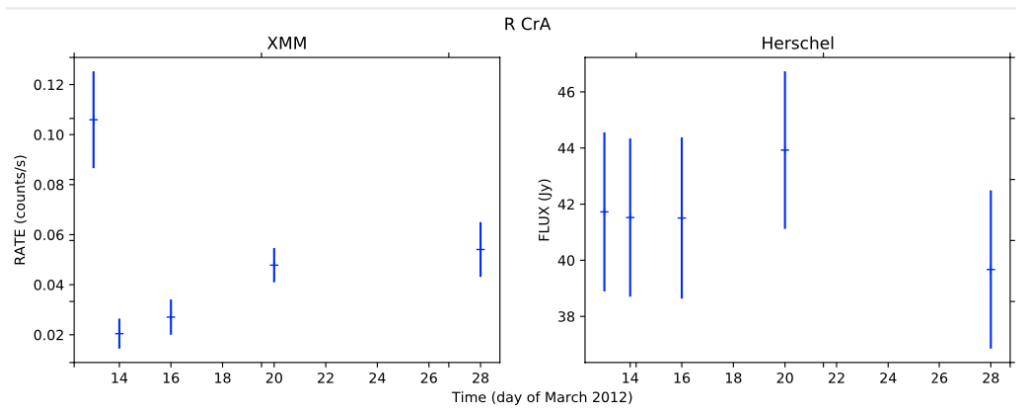
Figure 4.6: On the left is the light curve of R CrA using the flux detected by the XMM-Newton pn camera with time bins of the entire epoch observation time. On the right is the light curve of R CrA with the flux detected by the Herschel PACS photometer in the green channel and combining the scan and cross scan images (level 2.5 processing, hpf map)

Chapter 5

Discussion

5.1 Herschel

We found three sources to exhibit far-infrared variability. S CrA, IRS 2, and IRS 1 were variable in the green (100 μm) band and S CrA also showed variability in the red (160 μm) band. We can trust these were variable due to our conservative error estimates and our classification of variability based on S/N being greater than 3. These results verify what Billot et al. (2012) found using Herschel images of the Orion Nebula Cluster: that it is possible to observe variability in the far-infrared. As discussed in the introduction, the dynamical timescales of the far-infrared emitting material in the outer disk are much longer than the days to weeks variability we observed. Thus the mechanism responsible for this variability must be close to the central protostar. Flaherty et al. (2011) found evidence of a correlation between the accretion rate and the infrared excess. Billot et al. (2012) hypothesizes that the far-infrared variability could be the result of energetic photons generated in an accretion shock on an embedded protostar being reprocessed by the surrounding envelope and eventually escaping the protostar in the far-IR. The variations in the accretion luminosity due to the accretion events in the central protostar then propagate outwards and warm up the outer disk which would lead to detectable far-infrared variations.

Results comparison to Sicilia-Aguilar et al. (2013)

We did not find any new far-infrared sources as compared with the previous Herschel study of the Coronet Cluster by Sicilia-Aguilar et al. (2013). We compared our flux measurements to theirs and used our averaged fluxes over all five epochs since we did not

have variations greater than 17%. See Table 5.1 for this comparison.

	Herschel Photometry			
	Sicilia-Aguilar et al. (2013)	Our measurements	Sicilia-Aguilar et al. (2013)	Our measurements
	April 2011	March 2012	April 2011	March 2012
	100 μm (green) Flux (Jy)		160 μm (red) Flux (Jy)	
S CrA	17.7 ± 2.6	17.9 ± 0.1	13.6 ± 2.7	13.0 ± 0.1
IRS 2	82 ± 12	67.0 ± 0.4	61 ± 12	50.6 ± 1.6
IRS 5a/b	19.4 ± 2.8	19.3 ± 1.1	23 ± 5 *	30.1 ± 2.1 *
IRS 5N	15 ± 3	18.1 ± 1.1		
IRS 6	9.2 ± 1.3	7.0 ± 0.2	11 ± 2	10.1 ± 1.0
IRS 1	97 ± 14	97.0 ± 1.8	70 ± 14	64.3 ± 4.6
R CrA	71 ± 10	41.7 ± 2.8		
IRS 7w	476 ± 69	87.9 ± 4.8	880 ± 170 **	156 ± 21
IRS 7e	162 ± 24	43.1 ± 4.9		102 ± 21
SMM 2	12 ± 2	9.8 ± 0.7	25 ± 5	14.3 ± 2.3
T CrA	12 ± 2	13.0 ± 0.4	13 ± 3	

* Flux is for IRS 5a/b + IRS 5N as they were not resolved in red by Sicilia-Aguilar et al. (2013) or by our study.
** IRS 7e+w was unresolved in the 160μm photometry

Table 5.1: Comparison of our Herschel photometry (averages of all five epochs) to Sicilia-Aguilar et al. (2013) Herschel photometry taken 18 April 2011, about 11 months before ours.

We found our green and red flux were both within 3 sigma of their measurements for S CrA, IRS 2, IRS 6, IRS 1, and SMM 2. For R CrA and T CrA, which we were not able to resolve in red, the green flux was within 3 sigma as well. Our green flux measurements for both IRS 5a/b and IRS 5N were within 3 sigma of theirs. In red we did not resolve IRS 5a/b from IRS 5N and neither did Sicilia-Aguilar et al. (2013). Thus both of us took the photometry of IRS 5a/b + IRS 5N and our measurements were again with 3 sigma of theirs.

So the only flux measurements that were outside of 3 sigma were those of IRS 7e and 7w, their fluxes were far higher than ours, but they note that their values are uncertain due to proximity to other sources so that contamination could account for the differences. However this is interesting and could perhaps be an indicator of long term variability from IRS 7e and 7w. In their data IRS 7w was the brightest source in both bands, and in ours it was the brightest in the 160 μm band and the second brightest in the 100 μm band.

5.2 XMM-Newton

All of our X-ray sources exhibited some variability. We found the most variable of the X-ray sources was IRS 7e and IRS 5 was the most variable Class I protostar, which were the

results that Forbrich et al. (2007) observed as well. Forbrich et al. (2007) also detected a large flare in the X-ray from IRS 7e and they concluded that it was not due to an accretion shock but to circumstellar magnetic activity. Interestingly, in their dataset, the X-ray count rate of IRS 5 doubled between observations taken a day and a half apart. Between our second and third epoch, taken two days apart, we see the count rate of IRS 5 decrease by a factor of five.

5.2.1 4XMM Catalogue sources

Out of the 47 X-ray sources we found in the 4XMM Serendipitous Source Catalogue, six were not listed in the main CrA X-ray population papers (Forbrich & Preibisch, 2007; Peterson et al., 2011). We are interested in whether these are CrA members or background sources. Since X-ray is a good tracer for YSOs, this already makes them likely members. We also check to see if they are listed in any other catalogues as members, as this helps verify that they are not background galaxies. 4XMM J190031.5-365212 is listed as a source by Galli et al. (2020), which is the most recent census of Corona Australis since Peterson et al. (2011) but in the optical band, making our observation the first X-ray detection and verifying it as a cluster member. None of the other five sources have been verified as CrA cluster members by previous papers but four are listed in catalogues (matched using Vizier and setting the search radius to the positional error given in the 4XMM catalogue for each detection). 4XMM J190047.2-364747 and 4XMM J190248.6-365225 are listed as large-amplitude variable stars by Mowlavi et al. (2021). 4XMM J190104.5-370326 is only listed in the Cordoba Durchmusterung (Thome, 1994) which is a visual survey of southern stars. 4XMM J190243.4-370225 is listed in the near-infrared survey of R CrA by Haas et al. (2008). Lastly, 4XMM J190128.2-365927 is not listed in any catalogues besides 4XMM. When looking at the images from the two epochs in which this source is detected, it seems it is very close (4-5 arcsecs) to ISO-CrA 136. So while these two detections are technically distinct as their positional errors do not overlap, based on the image it is questionable if they are actually two sources, but we cannot be sure due to the angular resolution. Thus it is plausible that we have identified five or six new X-ray cluster members.

5.3   Light curve comparison

When comparing the Herschel to the XMM light curves, IRS 1 presented as the most interesting. The X-ray light curve peaked in the first epoch, followed by a steady decline. The far-infrared light curve peaked in the second and third epoch, and then declined. We found a strong positive correlation (using the Pearson Correlation Coefficient test) at an offset of one epoch, but with a 16% null hypothesis probability. Thus we cannot conclusively say there is a correlation due to the small sample size. This X-ray flare followed by a far-infrared flare could be an indication that the possible heating response seen by Flaccomio et al. (2018) on the inner disk due to X-ray flares may also be happening in the outer disk, where the far-infrared emission primarily originates. We cannot be sure if this is a response in the far-infrared since we could be picking up on the X-rays emitted due to the fact that even X-ray flares have some far-infrared emission at the tail of their SED, but this is unlikely since the flares were not simultaneous (the correlation coefficient was much lower when we calculated it with no epoch offset) and we would expect them to be simultaneous if all we were seeing was the X-ray emission. A good check we have included as future work would be to calculate the total luminosity of each of the flares to see if this size X-ray flare could have caused this size of infrared response using methods described in Alexander et al. (2004) (described in the future work section) and then use this to discuss how this could heat up the circumstellar material.

IRS 2 gave a second instance of a possible X-ray flare with a heating response, although with no significant correlation calculated. The XMM light curve peaked in the first epoch, indicating a possible flare, then decreased and again began to steadily increase again in the last three epochs by $40\% \pm 10\%$, which could be a second smaller flare. The Herschel light curve showed declining flux over the first four epochs (which was compared with the decreasing flux in the first two X-ray epochs and indeed, with an offset of two epochs, we calculated a moderate positive correlation, again with a low significance due to the very small sample size). The Herschel light curve then flares in the final epoch by $10\% \pm 1\%$, which could be a response to the X-ray flare in the later epochs, which could fit into our expected timescale of a response happening a few days after a flare. As part of our future work we would also like to calculate the sizes of these flares.

We found two more sources that had possible heating responses (but neither with significant statistical correlations from the Pearson Correlation Coefficient test, likely due

to the small sample size). R CrA had an X-ray flare in the first epoch and the far-infrared flux increased by 10% in the fourth epoch. However both of these measurements had errors so high that the S/N was ∼ 1-2. Secondly, it is possible that S CrA, which had an X-ray flare in the first epoch with flux almost four times higher than the following epochs and then infrared peaks in the third and fifth epochs, could have been an X-ray flare with a heating response. But since the infrared light curve has two peaks, it is hard to say which may have been the response. However it is possible there was another X-ray flare between the fourth and fifth epoch since that was the largest gap at eight days and X-ray flares usually happen on shorter timescales of hours to a couple days. In that case the far-IR flare we see in the fifth epoch could be a response to that. But without more time resolution we cannot be sure. Thus the far-infrared flare in the third epoch could be a heating response to the X-ray flare in the first epoch, giving us a time delay of about three days, but since the overall shape of the light curves are different, and we do not calculate a significant statistical correlation, we cannot be sure.

5.3.1   Most and least variable sources

We compared the light curves of S CrA, which was our most variable Herschel source. The XMM light curve started with a significant flare, then decreased and again flared in the final epoch, indicating flares on timescales of a couple weeks. The first flare was an increase of 380% ± 60% from the lowest epoch. However, the Herschel light curve decreases then increases then decreases again every epoch, seemingly having variability on timescales of days. This is surprising as we expect X-rays to be much more variable and the disk (which is what the far-infrared is probing) to not have any variability on these short timescales. It is possible the X-ray light curve did have variability we did not detect between epochs, however our time-resolved light curves did not show any variability on timescales of minutes to hours.

Our most variable X-ray source was IRS 7e which flared in the final epoch with flux 36 times higher than previous epochs. It is unfortunate our observation did not go further so we cannot be sure if there was an infrared response after the X-ray flare nor if the X-ray flare had just begun or was already ending due to that epoch being eight days after the previous observation. This also means we cannot make any conclusions about the length of the flare, except that it lasted during the entire observation which lasted almost two hours, as we see in the time-resolved light curve, and was constant during that time. The

Herschel photometry we have was quite constant, similarly to the XMM photometry from epochs 1-4, with a slight increase of $16\% \pm 18\%$ in the final epoch in the 100 μm band, but with errors too large to render it significant. Our Pearson Correlation Coefficient was 0.8, which is a strong positive correlation, and with a null hypothesis probability of 11%. While this is not enough to definitively say there is a correlation, due to sample size and errors, it is pretty low and shows that at least the steady flux in epochs 1-4 could be correlated.

IRS 5 is a good example of what we expected to see with our previous understanding of X-ray and far-infrared emission: in X-ray it was the most variable Class I protostar with variability of $390\% \pm 90\%$ yet its far-infrared emission was very constant, with measured variability being $5\% \pm 8\%$ for IRS 5a/b and $2\% \pm 8\%$ for IRS 5N. Thus, here we highlight that the least variable far-infrared source (IRS 5N) is not the same as the least variable in X-ray. In X-ray, the least variable source was IRS 2, which was, in contrast, one of our most variable Herschel sources.

In fact, when checking if the variable sources in one wavelength are variable in the other wavelength, we generally find quite the opposite. The most variable X-ray source, IRS 7e, was not the most variable in the far-infrared; actually it exhibited no reliable variability in the far-infrared. The most variable far-infrared sources, S CrA, IRS 1, and IRS 2, all exhibited some level of X-ray variability, but IRS 1 and IRS 2 were the least variable X-ray sources. Only S CrA was one of the more variable sources in both wavelengths. And our results were consistent with past studies that protostars are variable in the X-ray, even when constant in the far-infrared. Thus, at least within our small sample, there is not a correlation between general variability in X-ray and far-infrared.

5.3.2 SED class comparison

On average, when looking at classes, the most variable sources between wavelengths were somewhat consistent, since in X-ray the Class 0 and Class II protostars were most variable, while in far-infrared, the Class II protostars were the most variable. However we do not draw any global conclusions about which class protostars are most variable in X-ray due to our small sample size and also because this is a much debated and previously studied topic. For example, Forbrich & Preibisch (2007) found that in the Coronet Cluster, the Class I objects were more variable than the Class II and III objects in X-ray. They said this may be due to magnetic reconnection events causing frequent flares since the high plasma

temperatures of the younger stars show the X-ray emission is dominated by magnetic processes. Since far-infrared variability has only been detected once by Billot et al. (2012) and they do not comment on which classes are most variable, we have no comparison and can only say we found Class II objects to be more variable than Class 0/I, but note that also due to small sample size, this is a very tentative conclusion.

5.3.3   Time domain analysis

One of our original questions was whether we would find correlations after time domain analysis between the different wavelengths, and if so, whether they are in the same time domain or shifted. A shift would be indicative of an X-ray flare with a heating response in the far-infrared, whereas if they were in the same time domain that would be less likely due to the light travel time. We found a strong positive shifted correlation for IRS 1 of 1-3 days with a significance of 16% due to the small sample size. Also, for all of the variable far-infrared sources, we did not see X-ray variability in the same time domain, which strengthens the hypothesis that this is not just variable emission from the central object.

Chapter 6

Conclusion

We analyzed light curves for eleven young stellar objects in the Coronet Cluster taken simultaneously in far-infrared and X-ray over five epochs. This represents the first simultaneous multi-epoch comparison of far-infrared and X-ray variability in YSOs. In this section we list our primary conclusions.

- We found three sources that exhibited far-infrared variability: S CrA, IRS 2, and IRS 1. This verifies the results by Billot et al. (2012) showing it is possible to observe short timescale variability of YSOs in the far-infrared.

- All X-ray sources exhibit some level of variability. The most variable was IRS 7e, with a flare of up to 36 times the previous epoch's flux. The most variable Class I protostar was IRS 5. Both of these results are in agreement with Forbrich et al. (2007).

- The most variable sources were not the same in both wavelengths. The most variable far-infrared source was the T Tauri star S CrA and the most variable X-ray source was the Class 0 protostar IRS 7e.

- IRS 1 was variable in both wavelengths with an X-ray peak in the first epoch and a far-infrared peak in the second epoch. This could be an X-ray flare followed by a far-infrared heating response, with time domain shifted 1-3 days, as expected by the light travel time out to the far-IR emitting material. There was a strong positive correlation between the X-ray and far-infrared light curves with an offset of one epoch (with the first four X-ray epochs and the last four far-infrared epochs), but due to the small sample size of four, the null hypothesis probability was only 16%

and generally 5% is considered significant, so we cannot make a final conclusion on the correlation from this dataset alone.

- IRS 2 was also variable in both wavelengths and had a possible correlation between the X-ray and far-IR peak with a time domain shift of about 4-14 days, but this could not be verified as the correlation test had a very high null hypothesis probability, mostly due to the small sample size.

- There were no Coronet sources found only in the X-ray but not the far-infrared. However, in only the far-infrared we observed T CrA and SMM 2 and we resolved IRS 5a/b, IRS 5N, and IRS 7w. But we did not find any new far-infrared sources and our far-IR population matched that of Sicilia-Aguilar et al. (2013).

- Using the 4XMM Source Catalogue, we identified five or six possible new X-ray cluster members.

Chapter 7

Future Work

This project was very multi-faceted and there were many ideas we had and ways we could dig deeper that were not within the scope of this thesis. This includes comparing our far-infrared data to near-infrared studies of the Coronet cluster. These would not be within our simultaneous timeframe but would give an interesting look at near- versus far-infrared variability.

Our findings in this study motivate the science question "do we see a heating event here?", which to answer would require additional steps of X-ray radiative transfer. First we would calculate the actual luminosity of the X-ray and far-infrared flares (especially for IRS 1 where there was a possible correlation) to check if it was even possible for the X-ray flares to cause such a far-infrared response. And we could look at the SED of S CrA to see if it was emitting enough X-ray radiation to have caused the variability seen in the Herschel light curve. We would like to investigate how the flare could heat up the circumstellar material and possibly calculate if this size of flare could have caused this amount of disk heating. One way we could do this would be to apply the X-ray flare modeling discussed in Alexander et al. (2004). In this study, they look at two hydrostatic disk models, a simplified 1D model and then a 2D model, to see if there is enough X-ray radiation to drive disk winds. For this, they developed equations for each model that calculate the flux at each radius due to X-rays that originate in the magnetic reconnection events in the magnetosphere. Thus we could use these equations, once we have calculated the total luminosity from the X-ray flares, to see how much flux makes it to the outer disk region where the far-infrared emission comes from. We also would like to calculate more precise timescales of these events which would require modeling of the X-rays arriving at the outer disk and finding how long it takes them to heat the circumstellar material.

We would also like to extract XMM photometry for IRS 7w. We were not able to do this with our methods as IRS 7e and R CrA were both within the radius of the aperture centered on IRS 7w. However, IRS 7w did flare in the third epoch, which would be interesting to have photometry for and possibly compare with the Herschel results.

Overall, this study was the first step in comparing far-infrared and X-ray variability of YSOs, but future modeling and analysis could use this data to find further unique empirical constraints on processes in star formation.

Bibliography

Acke, B. & van den Ancker, M. E. (2004). ISO spectroscopy of disks around Herbig Ae/Be stars. *Astronomy & Astrophysics*, 426, 151–170.

Alexander, R. D., Clarke, C. J., & Pringle, J. E. (2004). The effects of X-ray photoionization and heating on the structure of circumstellar discs. *Monthly Notices of the Royal Astronomical Society*, 354(1), 71–80.

Andre, P. & Montmerle, T. (1994). From t tauri stars to protostars: Circumstellar material and young stellar objects in the rho ophiuchi cloud. *The Astrophysical Journal*, 420, 837–862.

Andre, P., Ward-Thompson, D., & Barsony, M. (1993). Submillimeter continuum observations of rho ophiuchi a: The candidate protostar vla 1623 and prestellar clumps. *The Astrophysical Journal*, 406, 122.

Andre, P., Ward-Thompson, D., & Barsony, M. (2000). From Prestellar Cores to Protostars: the Initial Conditions of Star Formation. In V. Mannings, A. P. Boss, & S. S. Russell (Eds.), *Protostars and Planets IV* (pp. 59).

Balog, Z., Müller, T., Nielbock, M., Altieri, B., Klaas, U., Blommaert, J., Linz, H., Lutz, D., Moór, A., Billot, N., & et al. (2013). The herschel-pacs photometer calibration. *Experimental Astronomy*, 37(2), 129–160.

Bibo, E., Dawanas, D., et al. (1992). The evolutionary stage of the herbig ae/be stars in the r coronae australis star-forming region. *Astronomy and Astrophysics*, 260, 293–302.

Billot, N., Morales-Calderón, M., Stauffer, J., Megeath, S., & Whitney, B. (2012). Herschel far-infrared photometric monitoring of protostars in the orion nebula cluster. *The Astrophysical Journal Letters*, 753(2), L35.

Blaes, O. M. & Balbus, S. A. (1994). Local Shear Instabilities in Weakly Ionized, Weakly Magnetized Disks. *The Astrophysical Journal*, 421, 163.

Brown, A. (1987). Radio emission from pre-main-sequence stars in corona australis. *The Astrophysical Journal*, 322, L31–L34.

Cazzoletti, P., Manara, C. F., Baobab Liu, H., van Dishoeck, E. F., Facchini, S., Alcalà, J. M., Ansdell, M., Testi, L., Williams, J. P., Carrasco-González, C., Dong, R., Forbrich, J., Fukagawa, M., Galván-Madrid, R., Hirano, N., Hogerheijde, M., Hasegawa, Y., Muto, T., Pinilla, P., Takami, M., Tamura, M., Tazzari, M., & Wisniewski, J. P. (2019). Alma survey of class ii protoplanetary disks in corona australis: a young region with low disk masses. *Astronomy & Astrophysics*, 626, A11.

Chen, H., Grenfell, T., Myers, P., & Hughes, J. (1997). Comparison of star formation in five nearby molecular clouds. *The Astrophysical Journal*, 478(1), 295.

Chini, R., Kämpgen, K., Reipurth, B., Albrecht, M., Kreysa, E., Lemke, R., Nielbock, M., Reichertz, L., Sievers, A., & Zylka, R. (2003). Simba observations of the r corona australis molecular cloud. *Astronomy & Astrophysics*, 409(1), 235–244.

Cody, A. M., Stauffer, J., Baglin, A., Micela, G., Rebull, L. M., Flaccomio, E., Morales-Calderón, M., Aigrain, S., Bouvier, J., Hillenbrand, L. A., & et al. (2014). Csi 2264: Simultaneous optical and infrared light curves of young disk-bearing stars in ngc 2264 withcorotandspitzer—evidence for multiple origins of variability. *The Astronomical Journal*, 147(4), 82.

Cugno, G., Quanz, S. P., Launhardt, R., Musso Barcucci, A., Brems, S. S., Cheetham, A., Godoy, N., Kennedy, G. M., Henning, T., Müller, A., & et al. (2019). Ispy – naco imaging survey for planets around young stars. *Astronomy & Astrophysics*, 624, A29.

Ercolano, B., Drake, J. J., Raymond, J. C., & Clarke, C. C. (2008). X-ray–irradiated protoplanetary disk atmospheres. i. predicted emission-line spectrum and photoevaporation. *The Astrophysical Journal*, 688(1), 398–407.

ESA (2013). Herschel closes its eyes on the universe. *ESA Science & Exploration*. URL: www.esa.int/Science_Exploration/Space_Science/Herschel/Herschel_closes_its_eyes_on_the_Universe (Date accessed: 4 February 2022).

ESA (2014). *Herschel Observers' Manual.* Version 5.0.3, Document Number: HERSCHEL-HSC-DOC-0876. URL: http://herschel.esac.esa.int/Docs/Herschel/pdf/observatory.pdf (Date accessed: 4 February 2022).

Flaccomio, E., Micela, G., Sciortino, S., Cody, A. M., Guarcello, M. G., Morales-Calderòn, M., Rebull, L., & Stauffer, J. R. (2018). A multi-wavelength view of magnetic flaring from PMS stars. *Astronomy & Astrophysics*, 620, A55.

Flaherty, K. & Muzerolle, J. (2010). Modeling mid-infrared variability of circumstellar disks with non-axisymmetric structure. *The Astrophysical Journal*, 719(2), 1733.

Flaherty, K., Muzerolle, J., Rieke, G., Gutermuth, R., Balog, Z., Herbst, W., Megeath, S., & Kun, M. (2012). Infrared variability of evolved protoplanetary disks: Evidence for scale height variations in the inner disk. *The Astrophysical Journal*, 748(1), 71.

Flaherty, K., Muzerolle, J., Wolk, S., Rieke, G., Gutermuth, R., Balog, Z., Herbst, W., Megeath, S. T., & Furlan, E. (2014). Connecting x-ray and infrared variability among young stellar objects: ruling out potential sources of disk fluctuations. *The Astrophysical Journal*, 793(1), 2.

Flaherty, K. M., Muzerolle, J., Rieke, G., Gutermuth, R., Balog, Z., Herbst, W., Megeath, S. T., & Kun, M. (2011). The Highly Dynamic Behavior of the Innermost Dust and Gas in the Transition Disk Variable LRLL 31. *The Astrophysical Journal*, 732(2), 83.

Fletcher, L., Dennis, B. R., Hudson, H. S., Krucker, S., Phillips, K., Veronig, A., Battaglia, M., Bone, L., Caspi, A., Chen, Q., et al. (2011). An observational overview of solar flares. *Space science reviews*, 159(1), 19–106.

Forbrich, J. & Preibisch, T. (2007). Coronae in the Coronet: a very deep X-ray look into a stellar nursery. *Astronomy & Astrophysics*, 475(3), 959–972.

Forbrich, J., Preibisch, T., & Menten, K. M. (2006). Radio and x-ray variability of young stellar objects in the coronet cluster. *Astronomy & Astrophysics*, 446(1), 155–170.

Forbrich, J., Preibisch, T., Menten, K. M., Neuhäuser, R., Walter, F. M., Tamura, M., Matsunaga, N., Kusakabe, N., Nakajima, Y., Brandeker, A., Fornasier, S., Posselt, B., Tachihara, K., & Broeg, C. (2007). Simultaneous X-ray, radio, near-infrared, and optical monitoring of young stellar objects in the Coronet cluster. *Astronomy & Astrophysics*, 464(3), 1003–1013.

Galli, P. A. B., Bouy, H., Olivares, J., Miret-Roig, N., Sarro, L. M., Barrado, D., Berihuete, A., & Brandner, W. (2020). Corona-Australis DANCe. I. Revisiting the census of stars with Gaia-DR2 data. *Astronomy & Astrophysics*, 634, A98.

Getman, K. V. & Feigelson, E. D. (2021). X-ray super-flares from pre-main sequence stars: Flare energetics and frequency.

Getman, K. V., Feigelson, E. D., Broos, P. S., Micela, G., & Garmire, G. P. (2008). X-Ray Flares in Orion Young Stars. I. Flare Characteristics. *The Astrophysical Journal*, 688(1), 418–436.

Getman, K. V., Feigelson, E. D., & Garmire, G. P. (2021). X-ray super-flares from pre-main sequence stars: Flare modeling.

Getman, K. V., Feigelson, E. D., Micela, G., Jardine, M. M., Gregory, S. G., & Garmire, G. P. (2008). X-ray flares in orion young stars. II. flares, magnetospheres, and proto-planetary disks. *The Astrophysical Journal*, 688(1), 437–455.

Groppi, C. E., Hunter, T. R., Blundell, R., & Sandell, G. (2007). High spatial resolution observations of two young protostars in the r corona australis region. *The Astrophysical Journal*, 670(1), 489–498.

Grosso, N., Hamaguchi, K., Principe, D. A., & Kastner, J. H. (2020). Evidence for magnetic activity at starbirth: a powerful x-ray flare from the class 0 protostar hops 383. *Astronomy & Astrophysics*, 638, L4.

Grosso, N., Montmerle, T., Feigelson, E., André, P., Casanova, S., & Gregorio-Hetem, J. (1997). An x-ray superflare are from an infrared protostar. *Nature*, 387(6628), 56–58.

Güdel, M. (2015). Ionization and heating by x-rays and cosmic rays. In *EPJ Web of Conferences*, volume 102 (pp. 00015).: EDP Sciences.

Güdel, M., Briggs, K., Arzner, K., Audard, M., Bouvier, J., Dougados, C., Feigelson, E., Franciosini, E., Glauser, A., Grosso, N., & et al. (2007). Accretion and outflow-related x-rays in t tauri stars. *Proceedings of the International Astronomical Union*, 3(S243), 155–162.

Haas, M., Heymann, F., Domke, I., Drass, H., Chini, R., & Hoffmeister, V. (2008). A near-infrared survey of the entire R Coronae Australis cloud. *Astronomy & Astrophysics*, 488(3), 987–996.

Hamaguchi, K., Corcoran, M. F., Petre, R., White, N. E., Stelzer, B., Nedachi, K., Kobayashi, N., & Tokunaga, A. T. (2005). Discovery of Extremely Embedded X-Ray Sources in the R Coronae Australis Star-forming Core. *The Astrophysical Journal*, 623(1), 291–301.

Hartmann, L. (2008). *Accretion Processes in Star Formation*. Cambridge Astrophysics. Cambridge University Press, 2 edition.

Herbig, G. H. (1960). The spectra of be-and ae-type stars associated with nebulosity. *The Astrophysical Journal Supplement Series*, 4, 337.

Herschel (2017). *Data Analysis Guide*. Version 11.1, Document Number: HERSCHEL-HSC-DOC-1199. URL: http://herschel.esac.esa.int/hcss-doc-15.0/print/dag/dag.pdf (Date accessed: 29 January 2022).

Hillenbrand, L. A., Strom, S. E., Vrba, F. J., & Keene, J. (1992). Herbig ae/be stars-intermediate-mass stars surrounded by massive circumstellar accretion disks. *The Astrophysical Journal*, 397, 613–643.

Imanishi, K., Koyama, K., & Tsuboi, Y. (2001). ChandraObservation of the ρ ophiuchi cloud. *The Astrophysical Journal*, 557(2), 747–760.

Joy, A. H. (1945). T tauri variable stars. *The Astrophysical Journal*, 102, 168.

Kaas, A. A., Olofsson, G., Bontemps, S., André, P., Nordh, L., Huldtgren, M., Prusti, T., Persi, P., Delgado, A. J., Motte, F., & et al. (2004). The young stellar population in the serpens cloud core: An isocam survey. *Astronomy & Astrophysics*, 421(2), 623–642.

Kastner, J. H., Huenemoerder, D. P., Schulz, N. S., Canizares, C. R., & Weintraub, D. A. (2002). Evidence for accretion: High-resolution x-ray spectroscopy of the classical t tauri star tw hydrae. *The Astrophysical Journal*, 567(1), 434–440.

Knacke, R., Strom, K., Strom, S., Young, E., & Kunkel, W. (1973). A young stellar group in the vicinity of r coronae austrinae. *The Astrophysical Journal*, 179, 847–854.

Knox Shaw, H. (1916). Note on the variable nebula in corona australis. *Monthly Notices of the Royal Astronomical Society*, 76, 646–647.

Koyama, K., Hamaguchi, K., Ueno, S., Kobayashi, N., & Feigelson, E. D. (1996). Discovery of hard x-rays from a cluster of protostars. *Publications of the Astronomical Society of Japan*, 48(5), L87–L92.

Lada, C. J. (1987). Star formation: From ob associations to protostars. *Symposium - International Astronomical Union*, 115, 1–18.

Lesniak, M. & Desch, S. (2011). Temperature structure of protoplanetary disks undergoing layered accretion. *The Astrophysical Journal*, 740(2), 118.

Martínez-Jiménez, M., Moyano-Cambero, C. E., Trigo-Rodríguez, J. M., Alonso-Azcárate, J., & Llorca, J. (2017). Asteroid mining: mineral resources in undifferentiated bodies from the chemical composition of carbonaceous chondrites. In *Assessment and Mitigation of Asteroid Impact Hazards* (pp. 73–101). Springer.

McCabe, C., Ghez, A. M., Prato, L., Duchêne, G., Fisher, R. S., & Telesco, C. (2006). Investigating Disk Evolution: A High Spatial Resolution Mid-Infrared Survey of T Tauri Stars. *The Astrophysical Journal*, 636(2), 932–951.

Meyer, M. R. & Wilking, B. A. (2009). Infrared spectra of young stars embedded in the r coronae australis cloud. *Publications of the Astronomical Society of the Pacific*, 121(878), 350.

Mowlavi, N., Rimoldini, L., Evans, D. W., Riello, M., De Angeli, F., Palaversa, L., Audard, M., Eyer, L., Garcia-Lario, P., Gavras, P., Holl, B., Jevardat de Fombelle, G., Lecoeur-Taïbi, I., & Nienartowicz, K. (2021). Large-amplitude variables in gaia data release 2 - multi-band variability characterization. *Astronomy & Astrophysics*, 648, A44.

Neuhäuser, R. & Forbrich, J. (2008). The corona australis star forming region. *arXiv preprint arXiv:0808.3374*.

Neuhäuser, R. & Preibisch, T. (1997). Rosat detection of class i protostars in the cra coronet. *Astronomy & Astrophysics*, 322, L37–L40.

Nisini, B., Antoniucci, S., Giannini, T., & Lorenzetti, D. (2005). Probing the embedded YSOs of the R CrA region through VLT-ISAAC spectroscopy. *Astronomy & Astrophysics*, 429, 543–557.

Nutter, D. J., Ward-Thompson, D., & Andre, P. (2005). The pre-stellar and protostellar population of R Coronae Australis. *Monthly Notices of the Royal Astronomical Society*, 357(3), 975–982.

Peterson, D. E., o Garatti, A. C., Bourke, T. L., Forbrich, J., Gutermuth, R. A., Jørgensen, J. K., Allen, L. E., Patten, B. M., Dunham, M. M., Harvey, P. M., et al. (2011). The spitzer survey of interstellar clouds in the gould belt. iii. a multi-wavelength view of corona australis. *The Astrophysical Journal Supplement Series*, 194(2), 43.

Poglitsch, A., Waelkens, C., Geis, N., Feuchtgruber, H., Vandenbussche, B., Rodriguez, L., Krause, O., Renotte, E., Van Hoof, C., Saraceno, P., et al. (2010). The photodetector array camera and spectrometer (pacs) on the herschel space observatory. *Astronomy & Astrophysics*, 518, L2.

Prato, L., Greene, T. P., & Simon, M. (2003). Astrophysics of Young Star Binaries. *The Astrophysical Journal*, 584(2), 853–874.

Preibisch, T., Kim, Y.-C., Favata, F., Feigelson, E. D., Flaccomio, E., Getman, K., Micela, G., Sciortino, S., Stassun, K., Stelzer, B., & Zinnecker, H. (2005). The origin of t tauri x-ray emission: New insights from the chandra orion ultradeep project. *The Astrophysical Journal Supplement Series*, 160(2), 401–422.

Read, A. M., Rosen, S. R., Saxton, R. D., & Ramirez, J. (2011). A new comprehensive 2D model of the point spread functions of the XMM-Newton EPIC telescopes: spurious source suppression and improved positional accuracy. *Astronomy & Astrophysics*, 534, A34.

Reynolds, J. H. (1916). The variable nebula in Corona Australia (N. G. C. 6729). *Monthly Notices of the Royal Astronomical Society*, 76, 645.

Shu, F., Adams, F., & Lizano, S. (1987). Star formation in molecular clouds: Observation and theory. *Annual Review of Astronomy and Astrophysics*, 25, 23–81.

Sicilia-Aguilar, A., Henning, T., Juhász, A., Bouwman, J., Garmire, G., & Garmire, A. (2008). Very low mass objects in the coronet cluster: The realm of the transition disks. *The Astrophysical Journal*, 687(2), 1145–1167.

Sicilia-Aguilar, A., Henning, T., Kainulainen, J., & Roccatagliata, V. (2011). Protostars and stars in the coronet cluster: Age, evolution, and cluster structure. *The Astrophysical Journal*, 736(2), 137.

Sicilia-Aguilar, A., Henning, T., Linz, H., André, P., Stutz, A., Eiroa, C., & White, G. J. (2013). Protostars, multiplicity, and disk evolution in the corona australis region: aherschelgould belt study. *Astronomy & Astrophysics*, 551, A34.

Sissa, E., Gratton, R., Alcalà, J. M., Desidera, S., Messina, S., Mesa, D., D´Orazi, V., & Rigliaco, E. (2019). The origin of r cra variability - a complex triple system hosting a disk. *Astronomy & Astrophysics*, 630, A132.

Skinner, S. L., Güdel, M., Audard, M., & Smith, K. (2004). New perspectives on the x-ray emission of hd 104237 and other nearby herbig ae/be stars from xmm-newton and chandra. *The Astrophysical Journal*, 614(1), 221.

Stauffer, J., Cody, A. M., Baglin, A., Alencar, S., Rebull, L., Hillenbrand, L. A., Venuti, L., Turner, N. J., Carpenter, J., Plavchan, P., & et al. (2014). Csi 2264: Characterizing accretion-burst dominated light curves for young stars in ngc 2264. *The Astronomical Journal*, 147(4), 83.

Stetson, P. B. (1987). Daophot: A computer program for crowded-field stellar photometry. *Publications of the Astronomical Society of the Pacific*, 99(613), 191.

Strom, S. E., Grasdalen, G. L., & Strom, K. M. (1974). Infrared and optical observations of herbig-haro objects. *The Astrophysical Journal*, 191, 111–142.

Swift, J. J. & Welch, W. J. (2008). A case study of low-mass star formation. *The Astrophysical Journal Supplement Series*, 174(1), 202–222.

Taylor, K. N. R. & Storey, J. W. V. (1984). The Coronet, an obscured cluster adjacent to R Corona Austrina. *Monthly Notices of the Royal Astronomical Society*, 209(1), 5P–10P.

Thome, M. J. (1994). VizieR Online Data Catalog: Cordoba Durchmusterung (Thome 1892-1932). *VizieR Online Data Catalog*, (pp. I/114).

Vievering, J. T., Glesener, L., Grefenstette, B. W., & Smith, D. M. (2019). New star observations with nustar: Flares from young stellar objects in the ρ ophiuchi cloud complex in hard x-rays. *The Astrophysical Journal*, 882(1), 72.

Ward-Thompson, D., Warren-Smith, R., Scarrott, S., & Wolstencroft, R. (1985). Evidence for discs and jets associated with r and t cr a. *Monthly Notices of the Royal Astronomical Society*, 215(4), 537–544.

Webb, N. A., Coriat, M., Traulsen, I., Ballet, J., Motch, C., Carrera, F. J., Koliopanos, F., Authier, J., de la Calle, I., Ceballos, M. T., & et al. (2020). The xmm-newton serendipitous survey. *Astronomy & Astrophysics*, 641, A136.

Wilking, B. A., McCaughrean, M. J., Burton, M. G., Giblin, T., Rayner, J. T., & Zinnecker, H. (1997). Deep infrared imaging of the r coronae australis cloud core. *The Astronomical Journal*, 114, 2029.

Wolk, S. J., Rice, T. S., & Aspin, C. (2013). Near-infrared Variability among Young Stellar Objects in the Star Formation Region Cygnus OB7. *The Astrophysical Journal*, 773(2), 145.